Fibre Optic Shape Sensing and Load Monitoring of Adaptive Aerospace Structures

Nazeer, N.

DOI
10.4233/uuid:f77b0e21-338d-4edf-81d6-8a2bd400d71a

Publication date
2022

Document Version
Final published version

Citation (APA)
Nazeer, N. (2022). *Fibre Optic Shape Sensing and Load Monitoring of Adaptive Aerospace Structures*. [Dissertation (TU Delft), Delft University of Technology]. https://doi.org/10.4233/uuid:f77b0e21-338d-4edf-81d6-8a2bd400d71a

He flew faster than the phoenix in his flight
when he dressed his body in the feathers of a vulture.

- M'umin ibn Said, on the first human flight by Abbas ibn Firnas; 9th century.

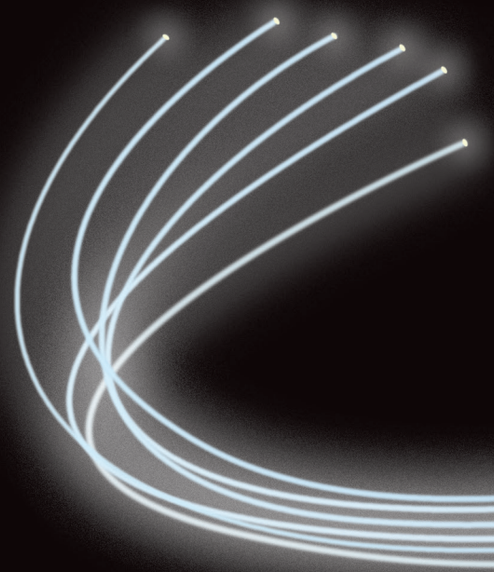

Fibre Optic Shape Sensing and Load Monitoring of Adaptive Aerospace Structures Nakash Nazeer

Fibre Optic Shape Sensing and Load Monitoring of Adaptive Aerospace Structures

Nakash Nazeer

INVITATION

You are cordially invited to attend the public defence of my PhD dissertation

Fibre Optic Shape Sensing and Load Monitoring of Adaptive Aerospace Structures

On Thursday,
the 30th of June 2022
at 10:00 hrs

At the Aula
Congrescentrum of
the Delft University of
Technology,
Mekelweg 5,
2628 CC, Delft,
The Netherlands

Nakash Nazeer

Propositions

accompanying the dissertation

Fibre Optic Shape Sensing and Load Monitoring of Adaptive Aerospace Structures

by

Nakash Nazeer

1. The closest reference to a complex morphing structure is an experimental based model. (thesis)
2. Sensor systems for morphing structures can only be considered smart after calibration in realistic conditions. (thesis)
3. Gaining knowledge from an experiment involves gathering as much data as required and not as much data as possible. (thesis)
4. The vision to achieve bird-like intelligence and flight performance is to limit one's thinking in the design of higher performing smart aircraft.
5. A quality that the PhD teaches you is being self-reliant which is exactly what your next job is not looking for.
6. The PhD experience involves learning that the statement 'it can't get any worse than this!' is always false.
7. It would be more efficient in terms of time and knowledge if the graduate school credit requirement was more flexible.
8. Gender equality should not be about having equal representation but rather about having equal choices and equal opportunities.
9. Only when poverty is eradicated would people collectively work towards a green planet.
10. COVID has made people realise that covering one's face is not a security threat.

These propositions are regarded as opposable and defendable, and have been approved as such by the promotors Prof. dr. ir. R. Benedictus and Dr. R. M. Groves.

Stellingen

behorende bij het proefschrift

Fibre Optic Shape Sensing and Load Monitoring of Adaptive Aerospace Structures

door

Nakash Nazeer

1. De dichtstbijzijnde referentie van een complexe morphing-structuur is een experimenteel gebaseerd model. (proefschrift)
2. Sensorsystemen voor morphing-structuren kunnen pas als slim worden beschouwd na kalibratie onder realistische omstandigheden. (proefschrift)
3. Kennis opdoen uit een experiment betekent zoveel gegevens verzamelen als nodig is en niet zoveel gegevens als mogelijk is. (proefschrift)
4. De visie om vogelachtige intelligentie en vliegprestaties te bereiken, beperkt het denken bij het ontwerpen van beter presterende slimme vliegtuigen.
5. Een kwaliteit die het doctoraat je leert, is zelfredzaam te zijn - en dat is precies waar je volgende werkgever niet naar op zoek is.
6. De PhD-ervaring houdt in dat men leert dat de uitspraak 'erger dan dit kan het niet worden!' altijd onjuist is.
7. Het zou, qua tijd en kennis, efficiënter zijn om een meer flexibele aanpak te hebben rond het behalen van de graduate school credits.
8. Gendergelijkheid moet niet gaan over het hebben van gelijke vertegenwoordiging, maar over het hebben van gelijke keuzes en gelijke kansen.
9. Alleen als de armoede is uitgebannen, zullen mensen collectief werken aan een groene planeet.
10. COVID heeft de mensen doen inzien dat het bedekken van het gezicht geen bedreiging vormt voor de veiligheid.

Deze stellingen worden opponeerbaar en verdedigbaar geacht en zijn als zodanig goedgekeurd door de promotoren Prof. dr. ir. R. Benedictus en Dr. R. M. Groves.

Fibre Optic Shape Sensing and Load Monitoring of Adaptive Aerospace Structures

Fibre Optic Shape Sensing and Load Monitoring of Adaptive Aerospace Structures

Dissertation

for the purpose of obtaining the degree of doctor
at Delft University of Technology,
by the authority of the Rector Magnificus Prof. dr. ir. T.H.J.J. van der Hagen,
chair of the Board of Doctorates,
to be defended publicly on
Thursday the 30^{th} of June 2022 at 10:00 hrs

by

Nakash NAZEER

Master of Science in Aerospace Engineering,
Nanyang Technological University, Singapore,
born in Madras, India.

This dissertation has been approved by the promotors.

Composition of the doctoral committee:

Rector Magnificus,	Delft University of Technology, chairperson
Prof. dr. ir. R. Benedictus,	Delft University of Technology, promotor
Dr. R. M. Groves,	Delft University of Technology, promotor

Independent members:

Prof. dr. W. N. MacPherson	Heriot-Watt University
Prof. dr. K. A. Williams	Eindhoven University of Technology
Prof. dr. ir. H. L. Offerhaus	University of Twente
Prof. dr. F. Scarano	Delft University of Technology
Prof. dr. F. C. T. van der Helm	Delft University of Technology
Prof. C. A. Dransfeld	Delft University of Technology, reserve member

Keywords: Fibre Bragg grating; FBG pair; Strain measurement; Optical interferometry; Spectral sensing; Multimodal sensing; Structural Health Monitoring; Morphing wing; Experimental mechanics.

Printed by: Ipskamp printing

Front & Back: Wing of a buff-breasted sandpiper with the impression of optical fibres running through and out of the wing.
Concept & initial design by: Nakash Nazeer
Final design by: Douwe Oppewal

ISBN (E-book) 978-94-6384-325-6
ISBN (Paperback) 978-94-6384-326-3

An electronic version of this dissertation is available at
http://repository.tudelft.nl/.

To Ma and Pa.

Contents

Summary xi

Samenvatting xiii

List of Abbreviations xv

List of Symbols xvii

List of Tables xix

List of Figures xxi

1 Introduction 1
- 1.1 The invention that shrunk the world . . . 2
- 1.2 The beginning . . . 2
- 1.3 Smart structures . . . 3
- 1.4 Morphing aircraft wings . . . 4
- 1.5 SmartX . . . 7
- 1.6 Motivation . . . 8
- 1.7 Thesis Outline . . . 9
- References . . . 10

2 Literature Review 13
- 2.1 Structural Health Monitoring . . . 14
- 2.2 Load Monitoring . . . 15
- 2.3 Shape Sensing . . . 18
- 2.4 Morphing monitoring . . . 21
- 2.5 Sensor selection . . . 22
- 2.6 Fibre Optic Sensors . . . 25
- 2.7 Grating based sensors . . . 26
  - 2.7.1 FBG sensing . . . 27
  - 2.7.2 FBG-Pair sensing . . . 28
- 2.8 Scattering based sensors . . . 29
- 2.9 Fabry-Pérot sensors . . . 30
- 2.10 Fibre optic interrogators . . . 31
- 2.11 Summary . . . 34
- References . . . 34

3 Research Workflow **47**
3.1 Exploring gaps . . . 48
3.2 Research questions . . . 48
3.3 Methodology . . . 50
3.4 Research process . . . 52
References . . . 53

4 Monitoring of a Cantilever Beam **57**
4.1 Introduction . . . 58
4.2 Cantilever Beam - 1D sensing . . . 58
4.2.1 Setup . . . 59
4.3 Measurements . . . 61
4.3.1 Calibration . . . 61
4.3.2 Unknown deflection at an unknown position . . . 63
4.4 Results . . . 64
4.5 Discussion . . . 65
4.6 Concluding remarks . . . 67
References . . . 68

5 Monitoring of a Cantilever Plate **71**
5.1 Introduction . . . 72
5.2 Cantilever Plate - 2D sensing . . . 73
5.2.1 Setup . . . 74
5.2.2 Sensor design . . . 76
5.3 Measurements . . . 78
5.3.1 Calibration . . . 78
5.3.2 Deflection at arbitrary locations . . . 80
5.3.3 Algorithm . . . 81
5.4 Results . . . 83
5.4.1 Finer grid . . . 83
5.4.2 Coarser grid . . . 90
5.5 Discussion . . . 91
5.6 Concluding remarks . . . 92
References . . . 93

6 Monitoring of a Morphing Wing Mock-up **97**
6.1 Introduction . . . 98
6.2 Morphing-wing mockup . . . 98
6.2.1 Setup . . . 100
6.2.2 Sensor design . . . 103
6.3 Measurements . . . 104
6.3.1 Morphing cases . . . 105
6.3.2 Calibration . . . 105
6.3.3 Arbitrary morphing . . . 106
6.3.4 Algorithm . . . 107

6.4 Results . . . 108
6.4.1 Arbitrary morphing . . . 112
6.5 Discussion . . . 112
6.6 Concluding remarks . . . 114
References . . . 115

7 Monitoring of the SmartX Wing Demonstrator 119
7.1 Introduction . . . 120
7.2 Collaboration and Contribution . . . 120
7.3 SmartX enabling technologies . . . 121
7.3.1 Slow morphing concept . . . 121
7.3.2 Fibre optic shape sensing . . . 123
7.4 Morphing control logic . . . 124
7.4.1 Manoeuvre Load Alleviation . . . 124
7.5 SmartX hardware demonstrator . . . 125
7.5.1 Setup . . . 125
7.5.2 Actuator Setup . . . 127
7.5.3 Sensor layout design . . . 129
7.6 Measurements . . . 131
7.6.1 Calibration . . . 131
7.6.2 Camber morphing - Wind tunnel tests . . . 131
7.6.3 Manoeuvre Load Alleviation . . . 132
7.7 Results . . . 132
7.8 Discussion . . . 136
7.9 Concluding remarks . . . 138
References . . . 139

8 Conclusions 143
8.1 Scope of the thesis . . . 144
8.2 Research process . . . 144
8.3 Key points . . . 145
8.4 Future work and ideas . . . 146

List of Publications 149

Acknowledgements 151

About the author 153

Summary

The aerospace industry is an ever-evolving field that has seen many technological advances over the past decades. The desire for aircraft to be not only efficient and reliable but also cheaper and safer has brought about many proposals across the industry. One of these advances is towards morphing aircraft wings to make wings lighter, more flexible, aerodynamically efficient and structurally stable. One of the key elements of a morphing wing is sensors that monitor the loads and shape of the wing throughout the flight. Within the framework of the SmartX project, the goal and contribution of this study is on the design and development of novel sensing methods for Structural Health Monitoring. This has been performed with a specific focus on shape sensing and load monitoring.

This thesis is focussed towards the design and development of a Structural Health Monitoring tool for adaptive aerospace structures and at the same time to reduce the dependency on a high number of sensors. Fibre Optic Sensors were chosen as the preferred sensing technology for this work. Compared to other sensors, fibre optic based sensors are advantageous because of their properties including high sensitivity, lightweight, capability of having multiple sensing points in a single fibre, flexibility and ability to operate in harsh environments.

Within the already available fibre optic sensor techniques an identification was made for demonstrating the potential of a higher performing SHM tool involving the combination of FBG spectral sensing and FBG-Pair interferometric sensing. A proposal is made to have a reliable, robust and cost effective sensing methodology for real time monitoring of morphing structures with a simultaneous focus on the SmartX morphing wing demonstrator. It is evident from the review that most of the focus of the work involving monitoring of morphing wings or wing-like structures is towards measuring deflections and mapping the deformation whilst the others are focussed on development of new sensing methods. The morphing data is not included as information to the controller about the morphing position, which could affect not only its current mission but its remaining service life. The morphing data can be utilised as an input to the control for active feedback regarding the morphing sequence and to ensure that the structure is not operating outside its design specifications. Additionally, information on the actuator effectiveness during morphing is not investigated.

The study begins with the demonstration of 1 dimensional sensing by estimating the position and magnitude of arbitrary loads on a beam. This is followed by the investigation of 2 dimensional sensing on a large cantilever plate. A self-contained mock-up morphing wing section was then analysed to understand the morphing mechanism and to give recommendations on the sensing fibre placement and sensor location. Finally, the potential for shape monitoring of morphing structures was

demonstrated on a 1.8 m composite morphing wing demonstrator. This was done in a wind tunnel along with studying the actuator effectiveness when subjected to different load alleviation tests.

Lastly, the method developed and demonstrated in this thesis is not limited to aerospace (and morphing) structures and can be extended to other engineering structures. Load carrying structures that undergo deformations/deflections can be monitored provided they are properly calibrated. These include, but are not limited to, rotor blades, masts, beam structures and bridges.

Samenvatting

De luchtvaart- en ruimtevaartindustrie is een sector die voortdurend in ontwikkeling is en die de afgelopen decennia veel technologische vooruitgang heeft gekend. De wens dat vliegtuigen niet alleen efficiënt en betrouwbaar, maar ook goedkoper en veiliger moeten zijn, heeft in de hele sector tot veel voorstellen geleid. Een van deze ontwikkelingen betreft het morphing van vliegtuigvleugels om de vleugels lichter, flexibeler, aërodynamischer en zijn constructie stabieler te maken. Eén van de belangrijkste elementen van een morphing-vleugel zijn de sensoren die de belasting en de vorm van de vleugel tijdens de vlucht monitoren. In het kader van het SmartX project ligt het doel en de bijdrage van deze studie op het ontwerp en de ontwikkeling van nieuwe sensormethodes voor Structural Health Monitoring. Dit is uitgevoerd met een specifieke focus op vormsensoren en belastingmonitoring.

Dit proefschrift is gericht op het ontwerp en de ontwikkeling van een instrument voor Structural Health Monitoring voor adaptieve luchtvaart- en ruimtevaartconstructies. Tegelijkertijd wordt onderzocht hoe de afhankelijkheid van een groot aantal sensoren kan worden verminderd. Optische vezelsensoren zijn gekozen als de gewenste sensortechnologie voor dit werk. Vergeleken met andere sensoren zijn de sensoren op basis van optische vezels gunstig vanwege hun eigenschappen, zoals hoge gevoeligheid, lichte gewicht, de mogelijkheid om meerdere meetpunten in één vezel te hebben, flexibiliteit en de mogelijkheid om in ruwe omgevingen te werken.

Binnen de reeds beschikbare optische vezeltechnieken werd een identificatie gemaakt om de mogelijkheid aan te tonen van een beter presterend SHM-instrument, waarbij een combinatie van FBG-spectrale detectie en FBG-Pair interferometrische detectie wordt gebruikt. Er wordt een voorstel gedaan voor een betrouwbare, robuuste en rendabele detectiemethode voor het in real-time monitoren van morphingstructuren met een gelijktijdige focus op de SmartX morphing demonstratievleugel. Uit het overzicht blijkt duidelijk dat het merendeel van de studies betreffende het monitoren van morphing-vleugels of vleugelachtige constructies gericht is op het meten van verplaatsing en het in kaart brengen van de vervorming, terwijl de anderen gericht zijn op de ontwikkeling van nieuwe monitoringsmethoden. De morphing-gegevens, met informatie over de morphing-positie, worden niet gebruikt voor de besturing. Dit zou niet alleen van invloed kunnen zijn op de huidige missie, maar ook op de resterende levensduur van het vliegtuig. De morphing gegevens kunnen worden gebruikt als input in de besturing voor actieve feedback over de morphing-volgorde en om ervoor te zorgen dat de constructie niet buiten haar ontwerpspecificaties opereert. Daarnaast is de informatie over de doeltreffendheid van de actuator tijdens de morphing niet onderzocht.

De studie begint met de demonstratie van eendimensionale monitoring door het

bepalen van de positie en de grootte van willekeurige belastingen op de balk. Daarna volgt het onderzoek van tweedimensionale monitoring op een grote cantilever plaat. Een onafhankelijk werkend model van een morphing vleugelonderdeel werd hierna geanalyseerd om het morphing mechanisme te begrijpen en om aanbevelingen te doen voor de plaatsing van de optische vezels en de locatie van de sensoren. Tenslotte werd de potentie voor vormcontrole van morphing-structuren gedemonstreerd op een 1,8 m composiete morphing demonstratievleugel. Dit werd gedaan in de windtunnel, net als het bestuderen van de effectiviteit van de actuator wanneer deze werd onderworpen aan verschillende belastingverlichtende testen.

Tot slot is de in dit proefschrift ontwikkelde en gedemonstreerde methode niet beperkt tot luchtvaart- en ruimtevaart (en morphing-) constructies en kan zij worden uitgebreid voor andere bouwkundige constructies. Dragende constructies die vervormingen/verplaatsingen ondergaan kunnen worden gemonitord, mits ze goed gekalibreerd zijn. Deze omvatten, maar zijn niet beperkt tot, rotorbladen, masten, balkconstructies en bruggen.

List of Abbreviations

ADC	Analog to Digital Converter(s)
ASCM	Aerospace Structures and Computational Mechanics
ASM	Aerospace Structures and Materials
CAD	Computer-Aided Design
CFRP	Carbon Fibre Reinforced Polymer
CL	Complexity Level(s)
CP	Calibration Point(s)
DAQ	Data AcQuisition
EFPI	Extrinsic Fabry-Pérot interferometer
EMI	Electromagnetic Interference
FBG	Fibre Bragg Grating
FBGP	Fibre Bragg Grating Pair
FC/APC	Ferrule Connector/Angled Physical Contact
FEM	Finite Element Method
FOS	Fibre Optic Sensing/Sensor(s)
FP	Fabry-Pérot
FSR	Free Spectral Range
FWHM	Full Width Half Maximum
INDI	Incremental Nonlinear Dynamic Inversion
INDI-QP-V	INDI Quadratic Programming Virtual
LPG	Long Period Gratings
MLA	Manoeuvre Load Alleviation
NACA	National Advisory Committee for Aeronautics
NASA	National Aeronautics and Space Administration
NDT	Nondestructive Testing
NI	National Instruments
NovAM	Novel Aerospace Materials
OJF	Open Jet Facility
OS	Optical Sensor
PRQ	Principle Research Question
PZT	Lead Zirconate Titanate
RI	Refractive Index
RQ	Research Question(s)

SHM	Structural Health Monitoring
SI&C	Structural Integrity and Composites
SM	Single Mode
TP	Test Point(s)
TRIC	Translation Induced Camber
UAV	Unmanned Aerial Vehicle(s)
WDM	Wavelength Division Multiplexing

List of Symbols

$n_{cladding}$	Refractive Index of the optical fibre cladding
$n_{core/eff}$	Refractive Index of the optical fibre core
λ	Wavelength
λ_B	Bragg wavelength
Λ	Periodic spacing of the grating
$\Delta\lambda_B$	Bragg wavelength shift
ρ_a	Photoelastic coefficient
ΔT	Change in ambient temperature
α_n	Thermal expansion coefficient
ξ	Thermo-optic coefficient
$R_{1/2}$	Reflectors of an FBG-Pair
L_c	Cavity length of an FBG-Pair
ΔL	Displacement
Φ	Phase difference
ΔT	Change in ambient temperature
L_t	Change in length due to ΔT
R	Reflectance of lossless reflectors
L/l	Length
b	Breadth
w	Width
t	Thickness
x_{root}	Root of the specimen
x_{tip}	Tip of the specimen
$S1$	FBG sensor 1
$S2$	FBG sensor 2
$S3$	FBG sensor 3
$S4$	FBG sensor 4
L_{sensor}	Effective sensor length
ε	Strain
δ	Deflection
c_t	Chord (top)
c_b	Chord (bottom)

s_t	Span (top)
s_b	Span (bottom)
F_y	Wing root shear force
M_x	Wing root bending moment
c_t	Chord (wing)
c_m	Chord (module)
s_w	Span (wing)
s_m	Span (module)

m	metre
mm	millimetre
cm	centimetre
km	kilometre
nm	nanometre
pm	picometre
μm	micrometre
s	seconds
dB	decibel
N	newton
Hz	hertz
rad	radians
deg	degrees

List of Tables

2.1 Relative property assessment of optical fibres and PZT sensors for embedding in adaptive composite systems [88]. 25

3.1 Relationship and alignment of the chapters with the Complexity Levels (CL) and Research Questions (RQ). 53

4.1 Material and geometric properties of the cantilever beam. 58
4.2 Properties of the grating sensors $S1$ and $S2$. 60
4.3 Comparison between the analytical modelling and experimental measurements for ΔL due to δ applied at the tip of the beam. 62
4.4 Comparison between the analytical modelling and experimental measurements for ΔL due to δ applied at the midpoint of the beam. . . . 62
4.5 Comparison between the analytical modelling and experimental measurements for ε due to δ applied at the tip of the beam. 62
4.6 Comparison between the analytical modelling and experimental measurements for ε due to δ applied at the midpoint of the beam. 63
4.7 Local strain (ε) and displacement (ΔL) measured between the grating sensors for deflections applied at the tip of the beam. 63
4.8 Local strain (ε) and displacement (ΔL) measured between the grating sensors for deflections applied at the mid of the beam. 64
4.9 Simultaneous estimation of unknown deflection (δ mm) at an unknown position (x mm) by the convergence of δ values from ΔL and ε. 65
4.10 Iteration sample of an 'extreme test' at 40 mm deflection focussed on repeatability. 67

5.1 Material and geometric properties of the cantilever beam. 74
5.2 Properties of the grating sensors S1, S2, S3 and S4 (DK Photonics). . 78
5.3 Typical magnitudes of measured displacement for ΔL_{1-2}, ΔL_{3-4}, ε_1 and ε_4. The plate was deflected at the centre by 20 mm. 83
5.4 Actual location of the test points A, B, C and D. 84

6.1 Material and geometric properties of the wing. 100
6.2 Properties of the fibre Bragg grating sensor pairs $S1/S1^*$, $S2/S2^*$, $S3/S3^*$ and $S4/S4^*$ (FORC-Photonics). Unlike other sensor pairs, $S3/S3^*$ had different wavelengths and are mentioned separately. . . 103

6.3 Allowable movement ranges specified and set by the calibration procedure to adhere to the structural design limits. This pertains to the actuator (x-axis) and the deflection of the wing tip (z-axis). 106
6.4 Actual deflections of the wing during bending due to arbitrary morphing A to D. 106
6.5 Actual deflections of the wing during twisting due to arbitrary morphing E to H. 106
6.6 Model estimated deflections of the wing during bending due to arbitrary morphing A to D. 112
6.7 Model estimated right deflections of the wing during twisting due to arbitrary morphing E to H. 112
6.8 Model estimated left deflections of the wing during twisting due to arbitrary morphing E to H. 112

7.1 Material and geometric properties of the wing. 125
7.2 Properties of the grating sensors S1, S2, S3 and S4 (DK Photonics). . 130

List of Figures

1.1 Illustration of Abbas ibn Firnas' attempt at flight in 875 AD [1]. . . . 2
1.2 First successful flight of the Wright Flyer by the Wright brothers in 1903 [8]. . . . 3
1.3 A wandering Albatross morphing its wings independently to optimise its flight [13]. *Photo by Paul Tixier*. . . . 4
1.4 Wing of an Airbus A320 aircraft showing the flap fairings [20]. a) Flaps retracted during cruise; b) Flaps extended during landing. . . . 6
1.5 Morphing compliant control surfaces by FlexSys Inc [22]. a) Unmorphed state and b) Morphed state through controlled deformations. . 6
1.6 Cyclic workflow of a smart wing system. . . . 7

2.1 Categorisation of loading types under structural and aerodynamic loading followed in this study. Influence of damage is not considered here. . . . 17
2.2 Components of a typical optical fibre. . . . 25
2.3 Categorisation of a few fibre optic sensors technologies. Grating based and interferometric sensing will be the focus in this thesis. . . 26
2.4 The different configurations of fibre and grating combinations used. From top to bottom: single-core, multi-core and multi-fibre configurations. . . . 27
2.5 Uniform gratings written on the fibre core. Λ denotes the grating period. . . . 28
2.6 Typical structure of a sensing pair. R_1 and R_2 represent the reflectors and L_c is the length of the cavity formed between them. . . . 29
2.7 Spectrum of backscattering waves showing stokes and anti-stokes components [113]. . . . 30
2.8 Basic configuration of a typical Fabry-Pérot Sensor . . . 31
2.9 Schematic representation of a typical Michelson interferometer working principle. . . . 32
2.10 Schematic of the Optics11 ZonaSens system along with the sensing zones in the fibre [120]. . . . 33
2.11 The ZonaSens interrogator box along with the reference (yellow) and sensor (white) fibre. . . . 34

3.1 Example spectra of the FBG, indicating the shift in Bragg reflection peak due to the fiber undergoing tension . . . 51

3.2 Example spectra of the FBG pair, indicating the sensing fiber undergoing gradual tension and compression 52
3.3 The building blocks in terms of complexity (CL) followed within the framework of this study. 54

4.1 Geometry and coordinate system of the cantilever beam setup. $S1$ and $S2$ are FBGs close to the root and tip of the beam, respectively. The fibre containing the FBGs was placed along the central axis as shown in the bottom figure in red. 59
4.2 The experimental setup showing the a) Beam vertically fixed to a b) Clamp on one end to form a cantilever. The c) Linear stage provided deflections on the beam whilst the d) National Instruments interrogator and e) Optics11 interrogator measured the readings from the grating sensors $S1$ and $S2$. 61
4.3 Location of the x (mm) values along the length of the beam used by the interpolation steps in Table 4.9. 65
4.4 Extreme deflection tests on the cantilever beam with the bonded optical fibre to check for repeatability and robustness. a) Undeflected and b) Deflected beam 67

5.1 Geometry and coordinate system of the cantilever plate setup. . . . 73
5.2 The experimental setup showing the a) Plate vertically fixed/clamped to a b) Support beam on one end. The c) Linear stage is attached to a d) Slider stage. The e) National Instruments interrogator, f) Optics11 interrogator and g) Optical switch are also shown. 74
5.3 The linear actuator and loading setup showing the vertical and horizontal slider stage mechanism. 75
5.4 Schematic of the experimental setup including the sensing and reference fibre. Zoomed in: Structure of the sensing fibre containing the $S1/S2$ and $S4/S3$ grating sensor pairs. 76
5.5 Layout of the fibre (in red) and the grating sensors. $S1$-$S2$ and $S3$-$S4$ are parallel and equidistant to the central axis of the plate and are along the clamped-free direction. 77
5.6 The highlighted pattern showing the area of interest and the 45 calibration points of the finer grid. The grid pattern is formed of 125 x 125 mm squares. The position of the sensors are also shown. 79
5.7 The highlighted pattern showing the area of interest and the 9 calibration points of the coarser grid. The grid pattern is formed of 250 x 500 mm rectangles. The position of the sensors are also shown. . 79
5.8 Location of the arbitrary test points A, B, C and D on the plate. . . . 80
5.9 Estimated location of the applied load for arbitrary test point A using the finer grid. The actual location is marked by the asterisk. The estimation is shown for a) 5mm, b) 10 mm, c) 15 mm, d) 20 mm and e) 25 mm deflections. 86

5.10 Estimated location of the applied load for arbitrary test point B using the finer grid. The actual location is marked by the asterisk. The estimation is shown for a) 5mm, b) 10 mm, c) 15 mm, d) 20 mm and e) 25 mm deflections. 87
5.11 Estimated location of the applied load for arbitrary test point C using the finer grid. The actual location is marked by the asterisk. The estimation is shown for a) 5mm, b) 10 mm, c) 15 mm, d) 20 mm and e) 25 mm deflections. 88
5.12 Estimated location of the applied load for arbitrary test point D using the finer grid. The actual location is marked by the asterisk. The estimation is shown for a) 5mm, b) 10 mm, c) 15 mm, d) 20 mm and e) 25 mm deflections. 89
5.13 Estimated location of the applied load for arbitrary test points a) A, b) B, c) C and d) D, using the coarser grid. The actual location is marked by the asterisk. The estimation is shown for 20 mm deflection. 90

6.1 Geometry and coordinate system of the test wing section. 99
6.2 The experimental setup showing the test wing's (a) fixed top surface, (b) sliding bottom surface, (c) actuator (up close in Figure 6.4), (d) sensing fibres (e) vertical scales, (f) optical switch, (g) National Instruments interrogator, (h) Optics11 interrogator and the (i) data acquisition system. 101
6.3 Side view of the wing attached to the support beams. The top section is fixed whilst the bottom section is allowed to slide. 102
6.4 The actuation mechanism showing the actuator attached to a fixed base plate and a moveable spring loaded stage plate. The controller is in the foreground. 102
6.5 Top-view of the wing with the optical fibre running along the x-axis in the bulk of the top (and bottom) section(s). The grating sensors $S1$, $S2$, $S3$ and $S4$ are on the top section. The sensors on the bottom section are a superimposition of the top sensor positions marked with asterisks ($*$); (eg., $S1$ is directly above $S1^*$ and so on). 104
6.6 The position of the wing during a) bend-up b) bend-down c) right-twist and d) left-twist morphing cases. 105
6.7 Strain trend in the top section of the wing through sensors a) $S1$ and $S4$ and b) $S2$ and $S3$, undergoing bend-down with respect to deflection due to morphing. Separate figures are used due to the large variation in scales. 109
6.8 Strain trend in the top section of the wing through sensors a) $S1$ and $S4$ and b) $S2$ and $S3$, undergoing bend-up with respect to deflection due to morphing. Separate figures are used due to the large variation in scales. 109
6.9 Strain trend in the top section of the wing undergoing twist with respect to deflection due to morphing. 110

6.10 Strain trend in the bottom section of the wing undergoing bend-down with respect to deflection due to morphing. 110
6.11 Strain trend in the bottom section of the wing undergoing bend-up with respect to deflection due to morphing. 111
6.12 Strain trend in the bottom section of the wing undergoing twist with respect to deflection due to morphing. 111

7.1 SmartX slow morphing concept: the trailing edge can seamlessly move up and down [2]. 122
7.2 TRIC skin ply drop pattern (one layer has a thickness of 0.12 mm) [2].123
7.3 Layout of the spanwise and chordwise optical fibres (in red) on the SmartX wing. Connections to the 14 fibres are through the fibre connector hub. 123
7.4 The experimental setup for shape sensing at the OJF (Open Jet Facility) low speed wind tunnel, showing the (a) wing, (b) optical fibres (yellow), (c) National Instruments interrogator, (d) Optics11 interrogator, (e) Thorlabs optical switch, and the (f) Data acquisition (DAQ) system. 126
7.5 Block diagram depicting the sequential workflow of the experiment. . 127
7.6 Overview of the wing showing the (a) fibre on module #1 and (b) internal view. The (c) actuator setup morphs the (d) seamless morphing modules that are connected through (e) flexible intermodular elastomeric skins [4]. 128
7.7 Zoomed-in images of module #1 of the test wing showing the module's upper surface (fixed) along with the optical fibre connector hub at its bottom. 128
7.8 Zoomed-in images of module #1 of the test wing showing the module's lower surface (sliding). 129
7.9 The U-shaped fibre layout (in red) on the upper (inner) surface of the morphing module. The location of FBG sensors ($S1$ to $S4$) along the fibre are as marked. 130
7.10 Estimated position with respect to module #1 deflections for the F_y = 20 and M_x = 0 case. The morphing sequence begins at ~15 s. The positions of actuators 1 and 2 are separated and shown in figures a and b, respectively. 133
7.11 Estimated position with respect to module #1 deflections for the F_y = 25 and M_x = 0 case. The morphing sequence begins at ~15 s. The positions of actuators 1 and 2 are separated and shown in figures a and b, respectively. 133
7.12 Estimated position with respect to module #1 deflections for the F_y = 30 and M_x = 0 case. The morphing sequence begins at ~15 s. The positions of actuators 1 and 2 are separated and shown in figures a and b, respectively. 134

7.13 Estimated position with respect to module #6 deflections for the F_y = 20 and M_x = 0 case. The morphing sequence begins at ~15 s. The positions of actuators 1 and 2 are separated and shown in figures a and b, respectively. 134
7.14 Estimated position with respect to module #6 deflections for the F_y = 25 and M_x = 0 case. The morphing sequence begins at ~15 s. The positions of actuators 1 and 2 are separated and shown in figures a and b, respectively. 135
7.15 Estimated position with respect to module #6 deflections for the F_y = 30 and M_x = 0 case. The morphing sequence begins at ~15 s. The positions of actuators 1 and 2 are separated and shown in figures a and b, respectively. 135
7.16 The mismatch in estimation between the servo command and the fibre optic sensor (FOS) measurement in degrees. 136
7.17 Experimental result for backlash-induced wing root shear force hysteresis loop [12]. 137

8.1 Idea for an unobstructive optical fibre pressure sensor. 147

1

Introduction

He flew faster than the phoenix in his flight
when he dressed his body in the feathers of a vulture.

M'umin ibn Said, on the first human flight by Abbas ibn Firnas; 9th century.

The aerospace industry is an ever-evolving field and has seen many technological advances over the past decades. The desire for aircraft to be not only efficient and reliable but also cheaper and safer has brought about many proposals across the industry. This push has seen new designs, materials and maintenance methods. One of these advances is towards morphing aircraft wings to make wings lighter, more flexible, aerodynamically efficient and structurally stable. One of the key elements of a morphing wing are the sensors that monitor the loads and shape of the wing throughout the flight. The design and development of smart sensing methods is important to support this. The research in this thesis under the project SmartX aims to address this need and work towards the design and development of smart sensing methodologies for shape sensing and load monitoring of morphing aircraft wings.

1

1.1. The invention that shrunk the world

The ability to fly is undoubtedly one of the most prominent inventions of this world. Airplanes have made a huge impact in society and have been used for different reasons including transportation, agriculture and trading. At any given point in time there are thousands of airplanes flying all around the globe. It is worthwhile to pause and appreciate their engineering beauty. Needless to say, they have become a normal part of our day to day lives.

1.2. The beginning

So, how did this all come to be? Since ancient times mankind has dreamt about flying like birds. The most apparent physical difference of humans from birds in terms of the capability to fly is the absence of wings. In order to imitate birds, the intuitive first step was to attach a pair of wings and launch oneself from a height. This was in hopes of getting airborne and to glide back to the ground.

This was attempted as early as in the 9th century by a polymath named Abbas ibn Firnas when he covered himself in a feathered suit and attaching a pair of wings to his arms [1]. He jumped off a cliff and flew 'a considerable distance' before hurting himself landing. It was recorded that he forgot to provide himself with a tail to aid in alighting as birds do. A couple of centuries later, Eilmer of Malmesbury attempted the same feat but also ended up hurting himself on landing by making the same mistake of skipping the tail [2].

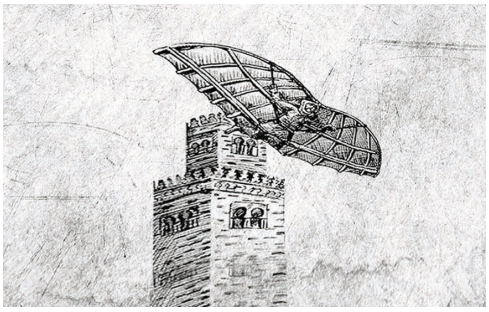

Figure 1.1: Illustration of Abbas ibn Firnas' attempt at flight in 875 AD [1].

Several such human flights were attempted following that before which the first 'heavier than air' flight was recorded. This came in the form of a manned but uncontrolled glider designed by George Cayley in 1853 [3]. In 1890, the first manned powered flight was confirmed by Clément Ader in his monoplane design which was again uncontrolled [4]. Otto Lilienthal on the other hand, in 1891, is claimed to have designed the very first manned and controlled glider [5].

The issue of control was a key element that was lacking in all the previous attempts. Combining all the contributions of the past attempts, the Wright brothers as of 1903 are known to have achieved the first piloted, sustained flight covering 37 m in a heavier-than-air machine at Kitty Hawk, North Carolina [6]. Since then

many changes have taken place in order to optimise human flight. Stephen Dalton writes in his book [7] that the Wright brothers' inspiration for flight undoubtedly came from birds, with their ability to soar up in the skies and to efficiently manoeuvre with little to no adverse effects to their bodies. What caught the Wright brothers' attention was the ability of birds to control their flight using their wings. As Orville Wright puts it, *'Learning the secret of flight from a bird was a good deal like learning the secret of magic from a magician'*.

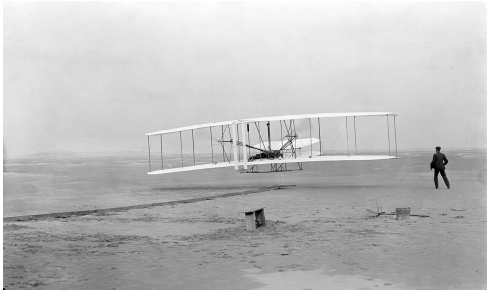

Figure 1.2: First successful flight of the Wright Flyer by the Wright brothers in 1903 [8].

The Wright flyer formed the basis for all future aircraft. Following this, improvements were made in countless iterations that led to the aircraft design that we know today. Regardless of that, there is ongoing research to improve flight to replicate the efficiency and perfection of birds.

The million-dollar question is not, 'What happens when we truly achieve the perfection of birds?', but rather, 'Could we ever reach that perfection?'.

1.3. Smart structures

The dictionary definition of smart structures are those that are capable of reacting to their environment with the help of multifunctional subsystems. These subsystems perform sensing and actuation as well as communication and control [9]. Smart structures are capable of sensing and reacting to external disturbances including temperature, pressure and load. More importantly, they are capable of monitoring their own *health* by either reacting accordingly to any perturbation or performing necessary functions to get back to their equilibrium state. Along these lines birds can be considered as 'smart'.

Today, technology has not yet advanced to the level where we can have aircraft wings that imitate those of birds in terms of movement and structural stability. The closest we have come to such an achievement is a fixed wing-root with a sweeping tip or a morphing wing control-surface or substructure [10].

To achieve this, aircraft should first be lightweight and also have a degree of flexibility. Their operational efficiency is dramatically increased by reducing the overall weight which has a direct effect on the fuel efficiency. For example, a

Boeing 787 that uses lightweight materials in its construction has been shown to have an increase in efficiency of up to 12% [11]. Airbus has also reported that the demand for new aircraft will progressively shift from fleet growth to replacement of older and less fuel efficient aircraft [12].

But, the issue of weight solves only part of the problem. What is also necessary to progress towards a morphing *bird-like* wing is to have active real-time control and optimisation for which a network of smart sensors are required. This is necessary to measure aerodynamic and structural data throughout the flight regime. This sensor-system is synonymous to the birds' nervous system that consists of permanently fitted unobtrusive sensors to form a network.

Figure 1.3 depicts a wandering Albatross as a prime example of flawless flight. Albatrosses morph their wings independently to optimise their glide. They adapt their geometry based on the surroundings and use a flight technique called dynamic soaring to keep themselves airborne whilst utilising the air around them to their advantage.

Figure 1.3: A wandering Albatross morphing its wings independently to optimise its flight [13]. *Photo by Paul Tixier*.

1.4. Morphing aircraft wings

The concept of morphing can be traced all the way back to the Wright Flyer (twist wing morphing, 1903) [14]. Following this there have been a lot of reports of aircraft implementing different morphing technologies. These include, but are not limited to, the Ptedrodactyl IV (sweep wing morphing, 1931), the MAK-10 (span wing morphing, 1931), the IS-1 (variable dihedral wing morphing, 1932), the LIG-7 (chord wing morphing, 1937), the MAK-123 (span wing morphing, 1947), the X 5 (sweep wing morphing, 1951), the XF10F (sweep wing morphing, 1952), the F 111 (sweep wing morphing, 1964), the XB 70 (span bending wing morphing, 1964), the SU 17 IG (sweep wing morphing, 1966), the MIG 23 (sweep wing morphing, 1967), the SU 24 (sweep wing morphing, 1967), the TU 22 M (sweep wing morphing, 1969), the F 14 (sweep wing morphing, 1970), the FS 29 (span wing morphing, 1972), the B 1 (sweep wing morphing, 1974), the Tornado (sweep wing morphing,

1974), the AD 1 (obliquing wing morphing, 1979), the Tu 160 (sweep wing morphing, 1981), the AFTI/F 11 (Mission Adaptive Wing morphing, 1985), the FLYRT (span wing morphing, 1993), the MOTHRA (camber wing morphing, 1994), the AAL (pitch wing morphing, 2001), the F/A 18 (Active Aeroelastic Wing morphing, 2002), the Virginia Tech team (span wing morphing, 2003; camber wing morphing, 2007 and 2010), the University of Florida research group (twist wing morphing, 2004; dihedral/gull wing morphing, 2005; sweep wing morphing, 2006; folding wing morphing, 2007), the MFX 1 and MFX 2 (sweep and span wing morphing, 2006 and 2007, respectively) and the Delft University of Technology research group (sweep wing morphing, 2008) [14]. Needless to say, a lot of work has been documented on morphing structures. These are again based on, but are not limited to, different applications, material or shape morphing mechanisms and geometry changes [14–18].

Moving on to the present day aircraft, at each stage within a flight envelope (take-off, cruise and landing) the geometrical design requirements of the wing changes. This is due to the fact that the structure needs to deal with different aerodynamic and inertial forces. For example, during landing the aircraft needs to maintain lift at lower airspeed. This is done by increasing the camber of the wing [19]. On the other hand, whilst cruising, a smaller camber is preferred for reduced drag [19]. The periods of take-off and landing are critical for the safety of the aircraft as it encounters its lowest flight speeds. In order for the aircraft to fly controllably at those speeds it has to stay above a certain speed limit called the stalling speed. Flaps are typically used to assist in increasing this stall speed [19] and prevent the aircraft from abruptly loosing lift and falling down. These flaps are basically hinged surfaces at either the leading or trailing edge of the wing and help in changing the camber of the wing. By doing so they increase (or decrease) the lift force on the aircraft.

This design approach has led to rather stiff wings along with additional mechanisms to accommodate control surfaces. Figure 1.4 shows a typical modern wing design with conical structures called flap fairings that house secondary mechanical components for the flap control assembly. The downside is that these are responsible for increased weight and drag. Optimisation of the wing to serve for each and every flight phase has been a challenge. That being said, apart from just using flap fairings, wing designs need to be improved in order to get rid of the heavy and complex mechanisms of conventional wing and control surface assemblies. At the same time they should also contribute to reduced drag and a capability to withstand external loads. Hence, research has been slowly progressing towards having an adaptive (morphing) wing and/or wing sections.

This is where morphing wings come into the picture. A morphing wing concept requires 'actuators attached to internal mechanisms, covered with flexible/sliding aerodynamic surfaces, together with load-transfer attachments between the skin and the skeleton' [14]. A morphing wing is capable of changing its aerodynamic geometry according to different mission requirements and to environmental effects. This is done to attain the maximum possible optimisation of the flight in terms of

(a) (b)

Figure 1.4: Wing of an Airbus A320 aircraft showing the flap fairings [20]. a) Flaps retracted during cruise; b) Flaps extended during landing.

reduced structural loads and drag, improved energy efficiency and ultimately reduced fuel costs. Traditional wings cannot change their shape without causing aerodynamic gaps (see Figure 1.4b). Morphing wings are gapless, do not have separate structures hinged together and potentially have less moving parts. The aerodynamic flow potential at every stage of the flight's envelope can be explored by having a morphing wing technology that adjusts to the changing flow and load requirements. This would allow higher aerodynamic performance as well as improved structural design. In short, having a morphing wing reduces the trade-offs required to ensure the efficient and safe operation of the airplane in multiple flight conditions [21].

An example of such a wing is the Flexfoil shape morphing wing shown in Figure 1.5. The Flexfoil wing has control surfaces whose geometry can be varied on demand. These control surfaces are seamlessly connected throughout the wing without the presence of flap fairing or gaps as in the Boeing 737's wing in Figure 1.4.

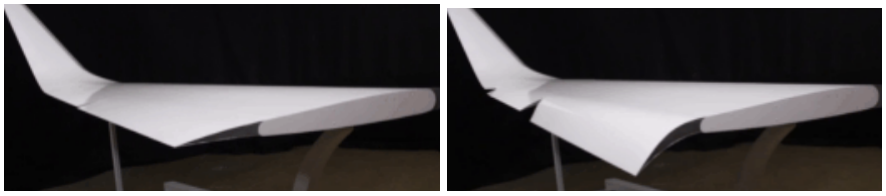

(a) (b)

Figure 1.5: Morphing compliant control surfaces by FlexSys Inc [22]. a) Unmorphed state and b) Morphed state through controlled deformations.

What would make these type of morphing wings 'smart' would be their ability to function analogously to a biological body. They should operate in a closed loop and should be capable of deciding in real time the best configuration by monitoring parameters related to the load, shape and health of the structure. This would be achievable with the participation of four essential elements, viz., the sensors, the

control strategies, the actuators and the power conditioning electronics [23].
Figure 1.6 depicts the typical cyclic principle of a smart-wing system.

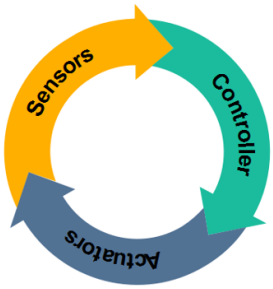

Figure 1.6: Cyclic workflow of a smart wing system.

In order to realise a perfect smart wing it would require:

- Smart sensing: The smart system should be capable of recording the changes caused as result of environmental and structural changes. These measurements would be further processed to accordingly either adapt or counter these changes.

- Smart controls: The sensors provide aerodynamic, structural and health related information to the controls. This control system takes appropriate decisions about what is the best outcome for the performance and structural health of the wing and passes this information to the actuators. Following that, the aforementioned sensors make sure the correct changes are taking place and validate them by reporting back to the controls. This process repeats forming a closed-loop control system.

- Smart actuation: This is an integral part of morphing structures. The actuators are responsible for carrying out intended deformations of (parts of) the wing to keep its performance optimised according to the mission requirements. The wing changes its geometry to adapt to the environment.

Sensors acquire important information and input the data to the controller. The control unit manages the incoming data and decides appropriate steps. Instructions are then sent to the actuators for those steps to take place. The sensors make sure the intended changes have taken place by sending feedback to the controller.

1.5. SmartX

Project SmartX was set up to make the Aerospace Structures and Materials (ASM) department of the Faculty of Aerospace Engineering at TU Delft world leaders in smart-wing-structures research and development. The research in this study is

part of the larger SmartX project involved in the design and development of an autonomous smart wing [24]. The end goal is to have a technology demonstrator that includes the three key elements of smart sensing, smart actuation and smart control strategies. The SmartX wing (named SmartX-Alpha) would be a one of a kind hardware demonstrator that would be tested in the wind tunnel.

With reference to the key elements required for a smart wing as discussed in section 1.4, Project SmartX will bring together the research activities within the Aerospace Structures and Materials (ASM) department. This will be done by combining the expertise in its individual research groups of Structural Integrity and Composites (SI&C), Novel Aerospace Materials (NovAM) and Aerospace Structures and Computational Mechanics (ASCM).

The researchers involved in the project and their brief objectives are as follows:

- **Nakash Nazeer** / SI&C: To design and develop smart sensing methodologies for shape sensing and load monitoring of the wing.
  Supervisor: Roger M. Groves.

- Tigran Mkhoyan / ASCM: To develop control and optimisation algorithms to optimise the autonomous wing for performance, flight dynamics and loads.
  Supervisor: Roeland De Breuker.

- Vincent Stuber / NovAM: To develop and integrate pressure sensors and fast actuators for the wing.
  Supervisor: Sybrand van der Zwaag.

1.6. Motivation

Morphing control surfaces undergo continuous deformations as a result of aerodynamic as well as structural loads. When we talk of an autonomous flying wing we also require its continuous monitoring to make sure it is operating within the specified design limits.

The optimum shape of the wing is realised by measuring the deformations of the morphing surface and communicating this information with the control system. Following this, appropriate actuation is carried out until the desired deformation and shape is achieved. This is to be done continuously with the help of an effective shape sensing method. Monitoring of the wing is vital for operational as well as for safety purposes. Therefore, Structural Health Monitoring is of prime importance for an autonomous smart wing.

Within the framework of the SmartX project, the goal and contribution of this study is on the design and development of novel sensing methods for Structural Health Monitoring. This has been done with a specific focus on shape sensing and load monitoring. The methodology and workflow will further be elaborated in Chapter 3.

1.7. Thesis Outline

This thesis consists of a total of 8 chapters. The details of each of the chapters are summarised below.

Chapter 1: The first chapter serves as an introduction to the thesis and the history of flight. The current trend to move towards smart structures is discussed with a focus on morphing aircraft wings. The bigger SmartX project is introduced elaborating on the goals of the project, the members involved and their individual contributions. Finally, the contribution and motivation of this study is put forward.

Chapter 2: This chapter covers the literature review necessary to understand the direction of the thesis. The chapter starts with a review of morphing aircraft and aircraft wings. An introduction to Structural Health Monitoring is made along with highlighting its requirements. This is followed by a review of shape sensing and load monitoring methods whilst explaining their importance for morphing wings. The currently available sensors for shape sensing and load monitoring are discussed and the selection of Fibre Optic Sensing technology for this study is justified. The fundamentals of Fibre Bragg Grating and Fibre Bragg Grating Pair sensing are presented which will serve as the basis of the sensing methodology proposed and presented in this study.

Chapter 3: This chapter summarises the literature review and points to the areas where more work is required. The chapter talks about how combining different methods can overcome problems with regard to smart sensing for morphing aircraft wings. A potential approach is identified for higher performing shape sensing and load monitoring that is robust and comparatively inexpensive. This sensing methodology selection, termed as the 'hybrid sensing approach', is justified and elaborated upon. The second part of this chapter details the research questions that the following chapters address. The research questions for Chapters 4 to 7 will be developed and defined in Section 3.2. The sub-research questions are aligned with the technical chapters of the thesis to tackle the gradual build-up in complexity.

Chapter 4: This chapter is the first of the four technical chapters of the thesis. The chapter deals with the identification of a higher performing fibre optic sensing methodology that is simple, less computational intensive to analyse the data and would require the least number of gratings for sensing. The aim of the sensing system is to be able to estimate the load and monitor the shape of the structure. A preliminary study on a cantilever beam was carried out to check the feasibility of the proposed sensing method with the aim of 1 dimensional sensing by estimating the position and magnitude of an arbitrary load. The results of this experiment are presented and discussed. This forms the basis for the upcoming chapters. The chapter ends by concluding the findings and talks about how these findings open up the idea for higher complexity involving 2 dimensions.

Chapter 5: This second technical chapter is a development on the previous chapter as it moves from a cantilever beam to a cantilever plate. The chapter deals with the application of the proposed sensing method for 2 dimensional sensing that involves both position and magnitude sensing. The feasibility of the approach investigated in the previous chapter is tested for a cantilever plate that includes an extra parameter, viz., twist. This chapter also studies the possibility of estimating the structural irregularities in the plate. The setup was modified to accommodate a large cantilever plate where 2 dimensional sensing is considered again for position and magnitude of an arbitrary load. The results of the study are presented and discussed. The chapter is concluded by discussing about the possibility of increasing the complexity and making a link to the next chapter involving a mockup of a morphing aircraft wing.

Chapter 6: This third technical chapter focusses directly on the monitoring of morphing structures. Laboratory experiments on an aluminium mockup morphing wing were carried out with an additional aim of studying the best placement of the optical fibres. The mockup wing's morphing design has some similarities with the SmartX morphing wing which would also help to form a basis for the study in the next chapter. The results of the study are presented and discussed. The chapter is concluded by making a bridge to the more complex SmartX demonstrator wing.

Chapter 7: This final technical chapter is a study on the SmartX composite morphing wing hardware demonstrator named as the 'SmartX-Alpha'. The knowledge gained from the previous chapter findings are incorporated in this wing for monitoring purposes. As opposed to the mockup wing the SmartX-Alpha was tested in the wind tunnel to be closer to the real-world application. The results of the study are presented and discussed. The chapter concludes by talking about the limitations of the experimental campaign and summarising the findings.

Chapter 8: This chapter concludes the thesis by giving a summary of the study and the end contribution of this work. The challenges faced along the way for carrying out the experiments are expressed and the recommendations for follow up and future work are listed. Additional ideas that could be adopted for Fibre Optic sensing on morphing wings are also presented.

References

[1] C. J. Botham. *Abbas ibn Firnas' Attempt At Flight*. [Online; accessed 4-August-2021]. url: https://www.onverticality.com/blog/abbas-ibn-firnas-attempt-at-flight.

[2] L. T. White Jr. "Eilmer of Malmesbury, an Eleventh Century Aviator: A Case Study of Technological Innovation, Its Context and Tradition". In: *Technology and Culture* 2.2 (1961), pp. 97–111. url: https://www.jstor.org/stable/3101411.

[3] D. W. Wragg. *Flight before flying*. Oxford: Osprey Publishing, 1974. isbn: 0850451655.

[4] T. D. Crouch. *Clément Ader*. Encyclopedia Britannica, 2021.

[5] J. D. Anderson Jr. *A History of Aerodynamics: And Its Impact on Flying Machines*. New York: Cambridge University Press, 1997. isbn: 9780521669559.

[6] "Airship Flight is a Success". In: *The San Francisco Call* (1903), p. 1. url: https://chroniclingamerica.loc.gov/lccn/sn85066387/1903-12-18/ed-1/seq-1/.

[7] S. Dalton. *The Miracle of Flight*. New York: Firefly Books, 1991.

[8] Wikimedia Commons. *File:Wrightflyer.jpg — Wikimedia Commons, the free media repository*. [Online; accessed 4-August-2021]. 2020. url: https://commons.wikimedia.org/w/index.php?title=File:Wrightflyer.jpg&oldid=499379693.

[9] Smart structures. *McGraw-Hill Dictionary of Scientific & Technical Terms, 6E*. [Online; accessed 5-April-2018]. url: https://encyclopedia2.thefreedictionary.com/smart+structures.

[10] D. Li, S. Zhao, A. Da Ronch, J. Xiang, J. Drofelnik, Y. Li, L. Zhang, Y. Wu, M. Kintscher, H. P. Monner, A. Rudenko, S. Guo, W. Yin, J. Kirn, S. Storm, and R. D. Breuker. "A review of modelling and analysis of morphing wings". In: *Progress in Aerospace Sciences* 100 (2018), pp. 46–62. issn: 0376-0421. doi: https://doi.org/10.1016/j.paerosci.2018.06.002.

[11] M. Marino and R. Sabatini. "Advanced Lightweight Aircraft Design Configurations for Green Operations". In: *Proceedings of the PRCC Conference Melborne - Australia* (2014). doi: 10.13140/2.1.4231.8405.

[12] AIRBUS. *Global market forecast 2021 – 2040*. AIRBUS, 2021.

[13] S. Ponton. *The wandering Albatrosses of the Crozet islands*. [Online; accessed 4-August-2021]. url: https://animalecologyinfocus.com/2018/06/26/the-wandering-albatross-of-the-crozet-islands/.

[14] S. Barbarino, O. Bilgen, R. M. Ajaj, M. I. Friswell, and D. J. Inman. "A Review of Morphing Aircraft". In: *Journal of Intelligent Material Systems and Structures* 22.9 (2011), pp. 823–877. doi: 10.1177/1045389X11414084.

[15] M. Sinapius, H. P. Monner, M. Kintscher, and J. Riemenschneider. "DLR's Morphing Wing Activities within the European Network". In: *Procedia IUTAM* 10 (2014). Mechanics for the World: Proceedings of the 23rd International Congress of Theoretical and Applied Mechanics, ICTAM2012, pp. 416–426. issn: 2210-9838. doi: 10.1016/j.piutam.2014.01.036.

[16] S. Barbarino, E. I. S. Flores, R. M. Ajaj, I. Dayyani, and M. I. Friswell. "A review on shape memory alloys with applications to morphing aircraft". In: *Smart Materials and Structures* 23.6 (2014), p. 063001. doi: 10.1088/0964-1726/23/6/063001.

[17] J. Sun, Q. Guan, Y. Liu, and J. Leng. "Morphing aircraft based on smart materials and structures: A state-of-the-art review". In: *Journal of Intelligent material systems and structures* 27.17 (2016), pp. 2289–2312. doi: 10.1177/1045389X16629569.

[18] D. Li, S. Zhao, A. Da Ronch, J. Xiang, J. Drofelnik, Y. Li, L. Zhang, Y. Wu, M. Kintscher, H. P. Monner, A. Rudenko, S. Guo, W. Yin, J. Kirn, S. Storm, and R. D. Breuker. "A review of modelling and analysis of morphing wings". In: *Progress in Aerospace Sciences* 100 (2018), pp. 46–62. issn: 0376-0421. doi: 10.1016/j.paerosci.2018.06.002.

[19] J. D. Anderson Jr. *Introduction to flight*. Boston: MacGraw-Hill Higher Education, 2005. isbn: 0072825693.

[20] **N. Nazeer**. *Airbus A320 en route Basel Euro Airport EAP - easyJet Switzerland*. [Photo on 14-Dec-2021].

[21] E. Stanewsky. "Adaptive wing and flow control technology". In: *Progress in Aerospace Sciences* 37.7 (2001), pp. 583–667. doi: https://doi.org/10.1016/S0376-0421(01)00017-3.

[22] FlexSys Inc. *FlexFoil*. [Online; accessed 20-April-2018]. url: https://www.flxsys.com/.

[23] H. Nguyen, W. Zatar, and H. Mutsuyoshi. "2 - Hybrid polymer composites for structural applications". In: *Hybrid Polymer Composite Materials*. Ed. by V. K. Thakur, M. K. Thakur, and A. Pappu. Woodhead Publishing, 2017, pp. 35–51. isbn: 978-0-08-100785-3. doi: https://doi.org/10.1016/B978-0-08-100785-3.00002-4.

[24] R. D. Breuker, T. Mkhoyan, **N. Nazeer**, V. Stuber, R. M. Groves, S. van der Zwaag, and J. Sodja. "Overview of the SmartX wing technology integrator". In: *Journal of Aircraft* (2022). Manuscript submitted for publication.

2

Literature Review

We do not need magic to change the world,
we carry all the power we need inside ourselves already.

J. K. Rowling

The advancement of technology in the past decade has brought about new structural designs in the aerospace industry. To ensure the safety and long-term reliability of these structures, cost-effective and reliable monitoring solutions are vital and are continually being sought. For this purpose, Structural Health Monitoring (SHM) is an important tool for establishing safety, reliability, desirable service life estimation and finally widening the knowledge regarding the structure being monitored. Over the years, a variety of sensors have been proposed and demonstrated for this purpose based on different applications. For the monitoring of aircraft structures the potential for the use of optical fibres has been well-documented. Shape sensing using Fibre Bragg gratings (FBG) in particular is not a mature technology for SHM when it comes to modern aircraft designs like morphing wings.

2

2.1. Structural Health Monitoring

The definition of Structural Health Monitoring in the words of Christian Boller is *'the integration of sensing and possibly also actuation devices to allow the loading and damaging conditions of a structure to be recorded, analyzed, localized, and predicted in a way that nondestructive testing (NDT) becomes an integral part of the structure and a material'* [1].

The term Structural Health Monitoring has been around for decades. SHM has been largely used to keep track of the integrity of various engineering structures. These structures can range from, but are not limited to, the field of aerospace [2, 3], wind turbines [4, 5], pipelines [6, 7] and civil engineering [8, 9].

In an ideal case, engineering structures would be designed and built for a long target-service-life. Although it would be preferred for structures to remain within their design specifications, they tend to naturally degrade over usage and time [10]. Any deviations from those limits may increase the cost of ownership and have an effect on safety [11]. Structural Health Monitoring aims to keep check and make sure the structure does not drift away from the said specifications. Structural Health Monitoring is hence of importance and could eventually also aid in extending the lifetime of the structure. This considerably decreases the costs for regular inspections/checks that would not have been necessary. That being said, a prudent SHM plan should be in place so that the cost of an SHM system does not outgrow the savings from the maintenance costs [12]. On a bigger scale, SHM can increase the reliability of the structure, avoiding longer downtime periods and allowing for the optimal usage of the structure.

The presence of an unknown number of small defects are certain in all materials [13]. Defects at a micro or nano level are intrinsic in nature, grow in size and become of interest for SHM detection. Contrary to a possible misconception, Structural Health Monitoring is not solely about the detection of faults or damage in a structure. The concept of SHM was first classified by Rytter is 1993 into four pre-defined levels, viz., detection, localisation, assessment and consequence [14]. Later in 2004, Worden and Dulieu-Barton proposed an addition of a level called classification [13] as a step after localisation. Their point was to show the importance of understanding the physics of the damage for effective identification at the last two levels. Therefore, information regarding the type of damage is also necessary.

The categorisation of SHM has currently been established and can be summarised into the following levels [1, 15]:

- Detection/Monitoring (Level I): This is the first step to establish whether the structure is operating within its specified design limits. The loads acting on the structure that cause it to shift from a defined design boundary are acknowledged. A challenge for the measuring device or sensors would also be to identify and isolate variations occurring due to changes in the environment instead of the structure.

- Localisation (Level II): The next step deals with the determination of the location of the loads and damage detected in level I. This is also helpful in

determining which areas of the structure are operating outside the design specification.

- Classification (Level III): This step is simply the identification of the type of load and damage monitored in the previous steps.

- Assessment/Quantification (Level IV): This step assesses the extent of the damage to the structure. A reference model is required in this step to evaluate the deviation from the allowable design specification.

- Consequence/Prognosis (Level V): This step deals with the evolution of the damage and the prediction of its residual lifetime. Information from past damage is also required to aid in the prediction.

Levels I, II and III deal with the actual properties of the current state of the structure. They are related directly to structural dynamics testing and modelling issues. On the other hand, levels IV and V deal with the long-term effect on the structures performance due to the loads and damage. They are associated with the fields of fracture and damage mechanics and fatigue life analysis [16].

My focus in this thesis is on levels I and II of SHM.

2.2. Load Monitoring

With reference to morphing aircraft wings, having information of the wing and wing section deflections as well as of the in-flight loads is key for the structural design process. This is also vital for morphing control as the information gathered could be used for load (including manoeuvre and gust load) alleviation purposes during flight [17]. As morphing wing and wing sections have the capability to optimise flight by changing their shapes appropriately they also benefit fuel efficiency by increasing the aerodynamic efficiency of the wing and in turn the aircraft overall [18].

Knowledge of the loads acting on an aircraft or aircraft section during its service life is a crucial parameter not only for damage prediction and estimation of the remaining service life [19], but also for morphing control. Damage present in the structure can be identified as their presence would cause a change in load distribution. Monitoring this change in load distribution would provide additional information on the health of the structure [20]. Calibration and reference data are required in order to distinguish between strain which are due to a change in shape and those due to material or structural degradation.

For the purpose of this thesis and with regard to monitoring of aircraft wings a distinction between load monitoring and damage monitoring is made.

The definition of *damage* is when a structure is no longer operating within its prescribed ideal condition and continues to operate in a sub-optimal fashion [13]. This

means that the stiffness of the structure has gone past a predefined operational boundary. This leads to permanent damage that ultimately lead to faults in the system. A *fault* is defined as when the structure is altered to the point that there is a reduction in quality and it is no longer capable of operating in a satisfactory manner [13]. In short, damage lead to faults.

Load(s), in general, is a term that includes structural, aerodynamic, gravity and manoeuvre loads. Based on the type of loading, there is a significant variation in their severity and frequency. A reference unloaded state can be specified at equilibrium (already taking into account gravity) and any deviation from this equilibrium is caused by loads acting on the structure.

Hence, a few points need to be established regarding load monitoring within the framework of this study.

- A structure can have a load acting upon it and still function at optimal fashion.
- The load tolerance level can be pre-defined by the structural design limits.
- Loads that go beyond the pre-defined structural limit may eventually progress to causing damage.
- Load is a temporary shift from the defined equilibrium whilst damage is a permanent state.

For an aircraft in flight, the structural and aerodynamic loads can be classified as primary and secondary loading, respectively. These in-flight time-varying loads could be significant enough to be detrimental to the integrity of the structure. Figure 2.1 shows the classification that will be followed in this study. The primary loading type consists of aerodynamic loads on the wing during flight that include manoeuvre and gust loads as well as structural loads caused by gravity [21]. The secondary loading type consists of varying loads brought forth due to the actuation of the control surfaces.

Operational load monitoring should lead to a successful deployment optimisation. This is because keeping checks on the structure during its operation will help in maintaining it within its designed limits. Having information about the loads acting on a section is a basic requirement to understanding the performance of the structure. In recent years many researchers have investigated the potential of monitoring these loads, examples of which will be mentioned below. Different methods have been implemented to capture this information and the preferred method has been the measurement of the strain as a direct result of these loads. Two of the most widely used sensor types are strain gauges and optical fibre sensors (also alternatively referred to as electrical strain gauges and optical strain gauges, respectively) whose references are mentioned in the following sections. The justification for the selected sensor technology in this thesis is given in Section 2.5.

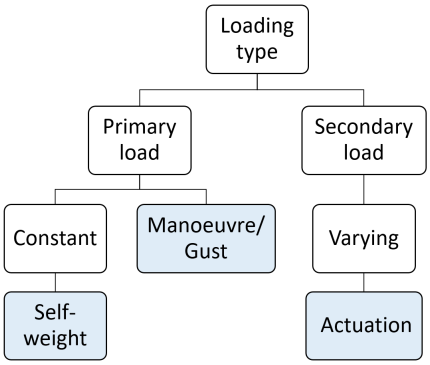

Figure 2.1: Categorisation of loading types under structural and aerodynamic loading followed in this study. Influence of damage is not considered here.

To monitor the loads on a wing spar, Liang et al. used a group of FBGs at multiple points [22]. By doing so, a relation between the load and the strain from each of the FBGs was established. The FBGs were aligned along different axes and each FBG independently measured the strain in their respective axes. A single FGB was not sufficient to monitor multiple axes but rather a group of them were required to capture all loading modes. Kwon et al. performed an in-flight wing loading estimation [23]. This was done by monitoring the strain, and in turn the structural loads, using multiple FBGs at specific and multiple points on the wing. An array of 6 FBG sensors was used for this purpose for each wing structure. In order to relate the wing loads with the strain distribution, calibration of the loads on each of the wings was performed. Kim et al. conducted static tests on a small full scale aircraft wing using different loading scenarios [24]. For this application they used a low sampling rate interrogator with 10 FBG sensors along the main spar. They continued the study to develop an SHM system for monitoring the loads on the wing. A series of ground and flight tests were carried out along with load calibration tests using a total 30 FBG sensors [25, 26].

Load measurements through strain response can also be done using resistance strain gauge rosette patterns [27]. When the principle strain directions are not known, rectangular or delta rosettes are incorporated. This rosette pattern has also been applied to optical strain gauges. When the principle strain directions are known it is preferred that the optical strain gauges are oriented along the strain axes for maximum strain response [28]. Li et al. monitored the loads on a wing spar subjected to bending loads using optical strain gauge rosettes [21]. They used a group of 15 FBGs in a delta pattern and showed their similarity with the results from the resistance strain gauges. Ertveldt et al. studied the response of a cantilever (wing) with FBGs bonded to it and subjected to aerodynamic loading in a wind tunnel [29]. Different angle of attacks were considered and the sensors measured the vertical deflection alone. The wings of Unmanned Ariel Vehicles (UAV) have also been monitored using FBGs [30]. The in-flight strain data was recorded using

a total 54 FBG sensors for tracking the structural response of the wings and the tail. Apart from aircraft wings as highlighted above, FBGs have also been used to monitor the loads on different sections of the aircraft including the tail [31] and the fuselage [32].

Mechanical strain gauges (or electrical resistance strain gauges) on the other hand have been a standard for strain measurements for decades [33]. Aircraft structures have been fitted with a number of these strain gauges for operational load monitoring [20].

The basic operating principle of an electrical strain gauge is the strain transfer from the measured object to an electrical conductor which is bonded to its surface [34]. The change in the shape and size of the conductor alters its length and the cross-sectional area which eventually affects its resistance. Whenever the conductor is stretched or compressed (within its elastic limits), it gets narrower and longer or shorter and broader, respectively. This causes a change in its resistance through which the changes in the strain can be found [34].

Electrical strain gauges typically use two to four wires for each measurement point. They also typically require an amplifier to convert the low amplitude output into a higher level of electrical signal. Moreover, unlike optical fibres, they are comparatively larger, not immune to harsh environments, sensitive to electrical noise and may require recalibration to be used effectively [35]. Having an extended region as strain sensors is also harder to achieve with electrical sensors.

Jebáček et al. measured the strain distribution of a wing along with a calibration of the loads using a total of 36 electrical strain gauges [36]. The static wing bending test results were compared to the in-flight measurements to calculate the fatigue life. Reymer and Leksi also used the strain distribution method to monitor the load spectrum with a focus on the wing bending moments [37]. They used electrical strain gauges at 86 different points with the final aim of estimating fatigue due to loading. Tang et al. developed a loading platform to monitor loads on an aircraft landing gear during different stages from taxi to landing [38]. Multiple strain gauges were attached at different locations to capture bending, shear and torque. Kurnyta et al. studied the operational loads on the wing by determining the in-flight loads during different phases of the flight using strain gauges and accelerometers [39, 40]. These sensors were bonded to pre-defined spots that they refer to as hot-spots (like the wings main spar) for load determination. This study resulted in better a utilisation of the aircraft.

2.3. Shape Sensing

Shape sensing can be defined as the process of using data from discrete strain measurements to reconstruct the displacement field of a structure. With regard to morphing wings, shape sensing is a fundamental requirement alongside load monitoring (see section 2.2). Shape sensing also aids in regulating and monitoring the in-flight loads [17] as well as in the optimisation and the increase in aerodynamic efficiency in flight [18].

Shape sensors were first reported using optical fibre technologies back in the

'90s. Djordjevich and Boskovic [41] demonstrated a single-axis sensor with the fibre transmissivity sensitive to its deflection curvature, from which strain can be inferred. Using this principle they were able to measure the curvature of a beam. They proposed that measurements of curvature can be carried out anywhere at the surface or in the bulk as the measurement principle is not dependant on the local strain. Additionally, changes in the material properties do not change the curvature of the structure as (regardless of damage) the curvature of the fibre is the curvature of the structure. A similar single-axis sensor was later developed using FBGs as strain gauges in a multicore fibre [42]. A fibre containing multiple cores was used in which each grating acted as independent strain gauges. The difference in Bragg wavelength between the gratings gave the local curvature. Building on this, two-axis sensors were demonstrated by differential strain measurement using interferometry (far-field interferogram [43], FBGs [44]) between cores of a multicore fibre [45]. Each fibre acts as independent strain gauge. The measurement of the local curvature was estimated by comparing the strains between all the fibres. Multiple distributed FBGs and chirped FBGs have also been reported for bend, curvature and 3D shape measurements [46]. Instrument tracking and reconstruction also finds applications in the medical industry. Multicore fibres have been used to track the shape of surgical needles using FBGs as optical strain sensors [47]. These different (fibre and grating) configurations are explained further in Section 2.7.

Combined measurement of the bending strain and vibration of a cantilever beam has also been demonstrated using FBG sensors [48]. Apart from determining the shape, distributed FBG sensors have the ability to measure dynamic displacements and measure vibrations in the structure [49, 50]. The data acquired from vibration analysis could be useful for smart structures for active vibration control and to decrease loads on the structure. The advantage of such fibres is that they have good isothermal behaviour as all the sensors are within one single fibre. The disadvantage, however, is that they require proper installation to have a reliable long term life. If the sensor fibres are not glued to the structure properly, creep in the glue may hinder the sensor's long term stability [44]. Shape sensing also comes in the form of deformation monitoring across the structure to estimate its shape. Earlier works have discussed shape reconstruction but mostly on simple structures in the lab environment [51, 52]. Moreover, they focus on optimising sensor location and mostly involve a large number of sensors.

Over the years, different optical fibre based curvature sensors and sensing methods have been investigated but their application mostly remains limited and within the lab environment. Very few reports have been made for deflection or displacement sensing for full scale morphing wing demonstrators. Moreover, the primary aim of the sensors are curvature or bend sensing whilst none give information on the location of the load being applied.

PZT (Lead Zirconate Titanate) is a piezoelectric ceramic material used as transducers. They are also of interest in Structural Health Monitoring as they offer the flexibility of being an actuator as well as a sensor. Like resistance strain gauges, they require wired connections to and from all sensors and this does not help in the effort to reduce the weight and complexity of the system when a large number of

sensors are considered [53, 54]. This is a major reason why PZTs and resistance strain gauges are not the preferred technology for our application. This is further elaborated in section 2.5.

Techniques like fringe projection [55] have also been reported for real-time 3D shape measurement. Patterns are projected on the target object and a camera captures these patterns and combines the data to map the shape of the object. Another shape sensing method is by projecting light on to the structure where image data is processed using colour coded sensors and by using artificial vision to obtain the shape of the object [56]. Yu et.al have presented a review of different fringe projection techniques for 3D shape measurement [57]. Anand et al. reconstructed the deformation surface of a convex object using the intensity measurement of volume speckle field and phase retrieval [58]. Charge Coupled Device (CCD) cameras were also utilised with an edge detection method by using a large number of pixels to form an image. Although this method was found to have high accuracy it had measurement limitations with respect to small vertical displacements [59]. Babovsky et al. used multiple cameras and demonstrated shape measurement by using digital holographic stereo photogrammetry with speckle patterns [60]. In most of the techniques, factors like illumination, installation, low scanning speed and reliability are a concern when attaching a camera based system to an aircraft body. In addition to that, it is quite difficult for the camera to take undistorted full swept photos of the wing to accurately measure the shape and/or the loads acting on it.

Moreover, non-visual sensing methods are generally preferred as they do not require the processing of large amounts of data. They are also cheaper and have faster acquisition rates for dynamic real-time monitoring. The most common method used nowadays for shape sensing is based on mapping displacements based on strain data from fibre optic sensors [61, 62]. The objective is to have sensors that can be fitted on (or in) an aircraft wing and to fly with them. The National Aeronautics and Space Administration (NASA) famously reported the shape sensing of an aircraft wing under bending loads. The system contained a series of FBGs bonded at specific points along the span of the wing. Multiple strain measurements were taken on ground and during flight and were used to reconstruct the shape of the wing [63, 64].

For aerodynamic loads, the current state of the art is using pressure sensitive paints which is a visual sensing approach. For reasons mentioned earlier they are not a viable option for our application. Moreover loads are typically measured based on multiple strain data and algorithms. The most commonly used algorithms are modal transformation theory, Ko's displacement theory and iFEM [65]. The optical technologies used for pressure load monitoring are based on Extrinsic Fabry-Pérot interferometers [66]. They consist of an optical cavity which is a region between the end of the fibre and the sensing membrane. The sensing membrane is basically a flexible diaphragm that allows single point measurements. Interferometry is used to measure the distance changes between the end of the fibre and the sensing membrane [35].

2.4. Morphing monitoring

In conventional aircraft wing designs, additional flap-type mechanisms are required in order to maximise flight efficiency during different flight regimes. As shown and explained in Section 1.4 these introduce gaps that are responsible for decreasing the aerodynamic efficiency as well as increasing aerodynamic noise. This leads to additional drag and reduced fuel efficiency. Morphing wings and control surfaces have the potential to overcome these issues.

The concept of morphing has been there since the Wright flyer was introduced as it was able to twist and morph its wings. As aircraft became larger and heavier in addition to carrying higher loads on the wings, the concept of morphing wings decreased. To accommodate higher wing loads and larger aircraft designs the wings were designed to be stiffer resulting in their inability to morph. The separation of functionalities in aircraft wings was introduced, where the wing load-carrying structure was separated from the rigid wing movables (control surfaces), which enabled the wing's high-lift and rolling capabilities [67]. However, since the 80's, there has been a growing interest again in morphing aircraft and morphing wings. A lot of work has been done that covers morphing aircraft including smart structures, materials and systems [18, 68–74]. Moreover, very rarely do these concepts focus particularly on monitoring of the morphing structure with tests in the wind tunnel or in flight.

As visual and non-contact methods are not preferred for in-flight applications, an alternative is to measure other properties of the morphing structure such as acceleration and/or strain. This is best done by means of attachable sensors.

Akl et al. used electrical resistance strain gauges to measure the morphing of structures [75]. A specially configured distributed network of wires were used where each wire sensor acted as a distributed strain gauge sensor that mapped the strain distribution over the entire surface of the wing. Similarly, a distributed network of optical sensors was also used to monitor the strain and in turn the morphing deformations of the wings [76]. Reich and Sanders used fibre optic strain gauges to investigate the structural deformation due to morphing by using a displacement–strain transformation matrix [77]. They used a combination of experimental and analytical modelling to develop a generic monitoring system. Butler et al. presented an approach to estimate the deformation of a morphing airfoil using glass fibres coated with radially aligned carbon nanotubes (CNT) [78]. Electrodes in an accompanying micropore allowed for a piezoresistive response of the CNTs when the fibres were deflected. Li et al. validated a method for monitoring the Flexible Variable Camber Wings (FVCW) based on the capturing strain data using FBGs as well as electrical strain gauges [79]. Laser range-finders were used for reference measurements and to verify the method. Sun et al. demonstrated a stretchable skin for monitoring of morphing wings [80]. An optical fibre was embedded in a flexible skin in an S-shaped pattern. As opposed to other works, FBGs were used in a multi-core fibre that consisted of a total of 7 cores. They noticed that the wavelength shift of the FBGs increased with the bending curvature of the skin whereas it decreased with the embedded depth of the fibre. Visual measurements were used

to verify the findings. Similar work was carried out by the group with the same aim with the help of 3 [81] and 48 [82] FBGs. Evenblij et al. demonstrated the potential of a sensing strip consisting of FBGs that was attached to a wing but expressed limitations in the design and morphing [83]. Smoker et al. studied the shape of morphing plate by monitoring the bending and twisting deflections using distributed wire sensors [84]. They used a ten segment sensor arrangement in order to extract the deflection information. He et al. used FBGs embedded in polyimide film skin to measure the deformation of the morphing wing [85]. They found that when the ratio of the upper to lower embedded depth was larger, the sensitively of the FBG sensor was higher. The morphing deformations were compared to visual measurements. Scheerer et al. used distributed and multiplexed fibre optic sensors for the development of a hybrid deflection and damage monitoring system [86]. Strain was measured at different positions on a CFRP structure to extract the morphing information. Tomić et al. presented a fibre optic interferometric technique aimed at measuring the deflection of morphing wings [87]. They measured the change of the phase angle of the light propagating in the fibre optic coil sensors to determine the deflections and the bending angle.

It is evident from the review that most of the focus of the work involving monitoring of morphing wings or wing-like structures is towards measuring deflections and mapping the deformation whilst the others are focussed on development of new sensing methods. The morphing data is not included as information to the controller about the morphing position which could affect not only its current mission but its remaining service life. The morphing data can be utilised as an input to the control for active feedback regarding the morphing sequence and to ensure that the structure is not operating outside its design specifications. Additionally, information on the actuator effectiveness during morphing is not investigated.

2.5. Sensor selection

For the purpose of this study involving load monitoring and shape sensing, I can acknowledge that the measurement of strain on the target surface is a requirement. From the review I can also establish that the most widely used and preferred methods for this are using optical or electrical strain gauges.

Schwartz has listed important parameters required for evaluating the performance of a sensor [88] and they are as follows:

- Sensitivity; this pertains to how sensitive the sensor is in reacting to external perturbations. It is also the ability of the sensor to detect weak signals.
- Measurement length; the length or area covered by the sensor across which a measurement is made.
- Bandwidth; the width of the operating frequency range of the sensor.
- Response time; the speed at which the sensor can respond to a change in the

variable.

- Temperature; the operating temperature range across which the sensor can reliably function.
- Repeatability; the closeness of the recorded data between multiple measurement trials under the same measurement conditions.
- Precision; the closeness of measurements recorded in multiple trials regardless of the accuracy.
- Weight of the sensor, and finally
- Cost of the sensor

Although electrical strain gauges have a rich history as a reliable source of strain measurement, they fall behind when compared to optical fibres. Electrical strain gauges require long installation times, have a lot of wiring to deal with (and can lead to electrical noise pickup too) and are prone to damage in harsh environments. Zhu et al. did a comparison of traditional resistance strain gauges with FBG sensors [89]. They noted that the time domain plots were smoother for FBG sensors which allowed a clear readable signal for efficient interpretation.

Fibre optic sensors on the other hand offer many advantages including flexibility, immunity to electrical noise, electrical and optical multiplexing and large spectral bandwidth [35]. They are negligible in weight and can have multiple sensors within the same fibre. Their ability to operate in harsh environments has opened up application possibilities. The sensors are intrinsically safe as they use light as a medium of interrogation and do not carry electricity. To prove their inconspicuous nature, earlier researchers compared the failure of composites with sensor-fibres embedded and non-embedded in the structure. It was proved that the performance of sensor-fibre embedded composites were the same as that of non-embedded composites in terms of failure stress [90]. Another study showed that optical fibres did not affect the stress concentrations within the structure which proved to be a good option for bonded as well as permanently embedded sensors [91]. Their performance was indicated by their capability of measuring reliable strain measurements. They have gained popularity over mechanical strain gauges as well as PZTs in the past years and have proven to be promising for SHM applications.

An additional advantage of fibre optic sensors is that they are capable of measuring internal strains unlike resistance strain gauges. With proper calibration and baseline measurements, their ability to monitor static as well as dynamic strain fields is a major advantage over other sensing methods [92]. Being able to measure internal strain is important in order to study internal load and fracture dynamics. Data from the deviations in local strains (and change in temperature) could give information about possible damage initiation due to prolonged or excessive loads [93]. An interesting conclusion was put forward that the highest internal temperatures were measured where the strains were the lowest, which was attributed to frictional

rubbing of surfaces around the cracks. This was because the highest temperatures were locally reached where strain was relaxed.

With fibre optic sensors, variations in structural or atmospheric properties like pressure, temperature and strain can be encoded into corresponding changes in frequency or wavelength, amplitude or phase of the transmitted light. Using appropriate demodulation systems or interrogators these changes can hence be monitored.

Leng and Asundi showed the feasibility of using both EFPIs and FBGs as sensors for detecting structural changes [94]. They conducted tests on composites and aluminium with and without damage (delamination and cracks, respectively) to show the sensors' capabilities. Parallel tests were also carried out with sensors in the bonded as well as embedded state and good correspondence between the two was noticed. They also reported that positioning of the sensor fibre was critical as it showed smaller strain levels when embedded closer to the neutral axis during bending.

The orientation of the optical fibres is crucial as the direction of maximum strain is always parallel to the axis of bending. This is for example also true for the Lamb wave propagation direction within the structure as FBGs are capable of detecting ultrasound. In other words, very weak signals would be picked up if the strain propagation is perpendicular to the optical fibre axis [92]. A way around this is to form a rosette pattern with the fibres in order to be able to localize the source of such waves [92, 95]. Researchers have also investigated the possibilities of hybrid arrangements, for example, an active SHM system where PZTs act as actuators whilst FBGs act as the sensors [96, 97]. This system was shown to be able to detect discontinuities within complex structures.

PZT sensors fall into the same category as strain gauges. Embedding them is not as desirable as fibre optic sensors as they have the tendency to debond or fracture under large strains [98]. However, optical fibres tend to break specifically at ingress points. This can easily be tackled by using adapters at the cross section of the composites to which other fibre connectors can be attached. That being said, a few points need to be kept in mind whilst embedding the optical fibres. For example, a) they should not degrade the mechanical properties of the material, b) the fibre should be well bonded for the accurate transfer of stress to the structure and c) the coating should be selected appropriately as it is partly responsible for the bonding as well as for protection against the harsh environment. With the additional help of optical devices [35] like splitters, couplers, optical switches and circulators an all-fibre system can be achieved.

Another noteworthy point of optical fibres is their low sensitivity to electromagnetic field/interference (EMI) which gives them an upper hand over PZTs (and strain gauges). A comparison of the main properties of fibre optic sensors and PZT sensors for embedding in adaptive composite systems are given in Table 2.1.

Following this review, optical sensors were chosen as the prospective sensors for this project and its applications. The subsequent sections focus on the different fibre optic sensing technologies available and their working principles.

Table 2.1: Relative property assessment of optical fibres and PZT sensors for embedding in adaptive composite systems [88].

Property	Optical Fibres	PZTs
Sensitivity	Moderate	Moderate
Gauge length	Moderate (better)	High
Bandwidth	High	Moderate
Resolution	High	Moderate
Temperature range	High	High

2.6. Fibre Optic Sensors

Over the past decades, fibre optic technology has revolutionised the telecommunication industry [99, 100]. It has also shown significant promise in the fields of industrial and environmental sensing [35, 101]. Optical fibres find applications in different fields including aerospace, railways, offshore and in the medical industry due to their properties like being lightweight, small in size and the ability to operate in harsh environments [35]. Fibre optic technology uses light as the carrier of information through a guided cable.

Fibre optic sensors (FOS) work by modulating one or more properties of a propagating light wave including intensity, phase, polarisation and frequency of the light in response to the environmental parameter being measured. A typical optical fibre consists of three parts, the core, the cladding and an outer buffer coating, as shown in Figure 2.2. Based on the diameter of the core they are further divided into single-mode and multi-mode fibres. If the modal volume number (also referred to as the 'V number') is lower than 2.405 [35], the light is spatially constrained to propagate in only a single mode along the waveguide axis. This happens when the dimensions of the core are comparable to the wavelength of the propagating light. On the other hand, when the modal volume number is greater than 2.405, additional higher order modes propagate.

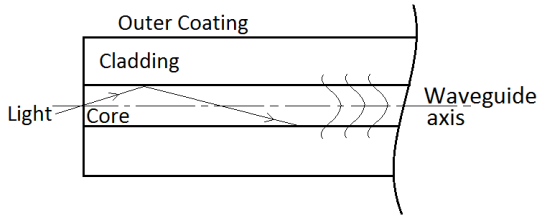

Figure 2.2: Components of a typical optical fibre.

To a first approximation optical fibres work under the principle of total internal reflection where the light is guided back into the core by the cladding. These fibres are thin strands of glass (or plastic) that act as a waveguide which allows certain modes to propagate. The cladding steers most of the stray light back into the

core ensuring the transmission of light through the core with minimal loss. This is achieved with a higher refractive index (RI) in the core relative to the cladding, i.e. $n_{cladding} < n_{core}$, causing total internal refection of the light. However, part of the light extends into the cladding region called the evanescent field. Sensors can make use of this evanescent field for sensing applications. For example, acoustic sensors have been formed by the evanescent coupling between adjacent optical fibres [35] and also evanescent-field sensors based on FBGs [102, 103]. The buffer coating serves as a protection for the fibre from external conditions and physical damage.

Fibre optic sensors can be broadly categorised into grating based, distributed and interferometric sensors. Figure 2.3 shows the categorisation of a few of the fibre optic sensor technologies used [104]. Grating based and interferometric sensing technologies are highlighted as they will be used later in this thesis. Fibre optic sensors can further classified as intrinsic and extrinsic (hybrid) sensors. The former uses the fibre itself as the sensing element whereas the latter uses the fibre only as a mechanism to transmit light to and from a sensing element.

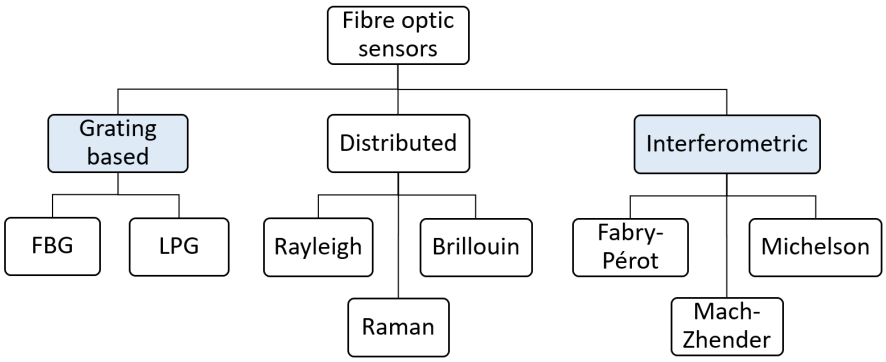

Figure 2.3: Categorisation of a few fibre optic sensors technologies. Grating based and interferometric sensing will be the focus in this thesis.

2.7. Grating based sensors

Grating based sensors contain a periodic perturbation of the refractive index of the core. Gratings can be of different patterns/types including uniform, chirped, tilted and superstructure gratings [105]. Based on the length of the period, they are classified into long (long-period gratings) and short (fibre Bragg gratings) period gratings. Long-period gratings (LPG) typically have a grating period that ranges from 100 µm to 1 mm [106]. They couple light from the guided core mode to forward propagating cladding modes. Fibre Bragg gratings on the other hand have a sub-micron period and couple light from the forward-propagating mode to the

counter propagating mode [102]. FBG sensors currently represent one of the most rapidly growing areas of research in the field of fibre based sensing [107].

In terms of grating configurations, they can be combined with different fibre arrangements as shown in Figure 2.4. The most widely used configuration is the single-core fibre with either single of quasi-distributed gratings. The next one is the multi-core configuration which is predominantly used for multi-axis measurements. Another configuration that is also found is a single fibre with multi-cores.

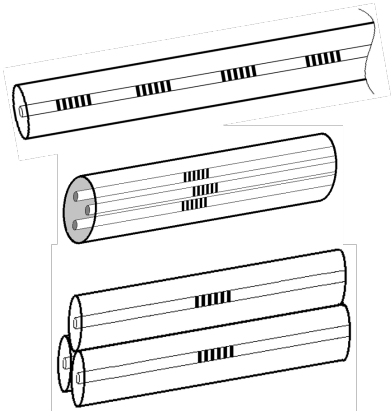

Figure 2.4: The different configurations of fibre and grating combinations used. From top to bottom: single-core, multi-core and multi-fibre configurations.

2.7.1. FBG sensing

FBGs work on the principle of Bragg reflection. The uniform gratings, as shown in Figure 2.5, that form the sensing region, are capable of modulating the amplitude and phase of incoming light with respect to external disturbances. The permanent changes in the refractive index of the core are a result of the photosensitivity in these fibres. In order to easily achieve these changes, photosensitive fibres are normally used [108]. A laser is used to write (etch) the required grating pattern with specific wavelengths on the core of the fibre through a phase mask [102]. Several methods have been implemented to fabricate grated fibres [102]. These gratings can vary in pattern based on application and choice.

The grating region acts as a bandpass filter in transmission and a bandstop filter in reflection. On undergoing perturbations, a narrow band of the incident optical field is reflected with a central wavelength which is the on-resonance condition. This is due to successive coherent scattering from the index variations. This wavelength is referred to as the *Bragg wavelength* [109] and is given by:

$$\lambda_B = 2n_{eff}\Lambda, \tag{2.1}$$

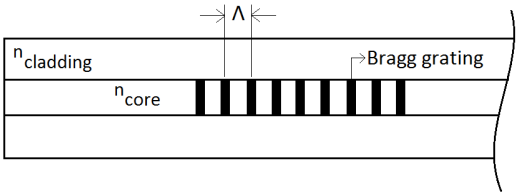

Figure 2.5: Uniform gratings written on the fibre core. Λ denotes the grating period.

where λ_B is the Bragg wavelength, n_{eff} is the refractive index of the core and Λ is the periodic spacing of each grating (also refer to figure 2.5).

External perturbations (including mechanical and thermal changes) on the optical fibre influence the Bragg wavelength (λ_B) given that it is a function of the refractive index of the core and the spacing between the gratings. The result is referred to as a shift in the Bragg wavelength and is denoted as $\Delta\lambda_B$. This shift is represented as strain and is calculated as [110]:

$$\Delta\varepsilon = \frac{\Delta\lambda_B}{\lambda_B(1-\rho_a)} - \Delta T(\alpha_n + \frac{\xi}{(1-\rho_a)}), \tag{2.2}$$

where $\Delta\varepsilon$ is the calculated strain, ρ_a is the photoelastic coefficient, α_n is the thermal expansion coefficient, ξ is the thermo-optic coefficient and ΔT is the change in ambient temperature.

In order to accurately measure and decipher the central wavelength and its position, there is a need to have a reference Bragg wavelength measurement. The reflection spectra is recorded using spectrometers found in FBG interrogators and the central Bragg wavelength is determined by calculation. Finally, the magnitude of wavelength shift to converted in terms of μ strain.

2.7.2. FBG-Pair sensing

As the name suggests, two FBGs are required for this type of sensing. The structure of a typical FBG-Pair is as shown in figure 2.6. The basic requirement is the presence of two reflectors (R_1 and R_2) that would form a cavity or region in the primary fibre (sensing fibre) that operate on different wavelengths. This could be considered similar to an in-line fibre etalon [111] except that an additional hollow core region is not required to be spliced to the sensing fibre. In this setting and for the purpose of this study, the reflectors are the FBGs themselves which is where the term 'FBG-Pair' sensing comes from.

The sensing methodology is based on the principle of comparing phase differences between interference patterns [112]. A reference fibre is required for this comparison that contains a mirror fixed at its end and is compared to the light reflected by the two reflectors. The region between the reflectors (the cavity) is sensitive to external mechanical and/or thermal perturbations. The phase difference is calculated based on the difference in the interference patterns between the

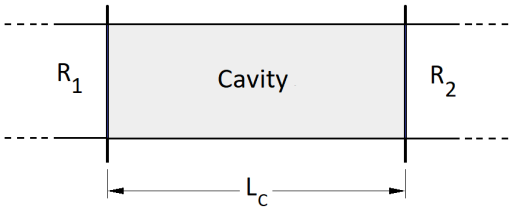

Figure 2.6: Typical structure of a sensing pair. R_1 and R_2 represent the reflectors and L_c is the length of the cavity formed between them.

reflected lights from the reference fibre and the sensing fibre. As this phase difference is a caused due to change in L_c, measuring this length would give the change in optical path-length between the two reflectors, and is given by:

$$\Delta L = \frac{1}{n}[(\frac{\Delta\Phi\lambda}{2\pi}) - L_c\Delta n] \tag{2.3}$$

where ΔL is the displacement, n is the refractive index, Φ is the phase difference and λ is the wavelength at which the grating reflects light.

The total strain therefore due to this perturbation is calculated in terms as strain and is given by:

$$\varepsilon = \frac{\Delta l - L_t\Delta T}{L_c}, \tag{2.4}$$

where ΔT is the change in ambient temperature and L_t is the change in length due to ΔT.

2.8. Scattering based sensors

Scattering based sensors make use of the intrinsic scattering property of the fibre core material. These constitute Rayleigh, Brillouin and Raman components [113] as depicted in the spectrum in Figure 2.7. Backscattering waves have been used to sense parameters like strain and temperature [114, 115]. Rayleigh scattering has the largest amplitude within the spectrum that occurs due to the presence of density and composition variations introduced during the manufacturing process. This scattering occurs due to variations in the index of refraction of the fibre core. When a narrow pulse of light is sent through the fibre, variations in the backscatter can determine the approximate spatial location of these variations. Brillouin waves are frequency shifted due to interactions with acoustic waves (phonons) which are related to applied strain or temperature. The location of scattering is determined by interrogating the time of arrival of the scattered light. This gives information on strain or temperature along the length of the fibre. Similarly, the intensity ratio of two components of Raman scattering (Stokes and anti-Stokes) is a function of temperature and hence gives information of the temperature along the fibre.

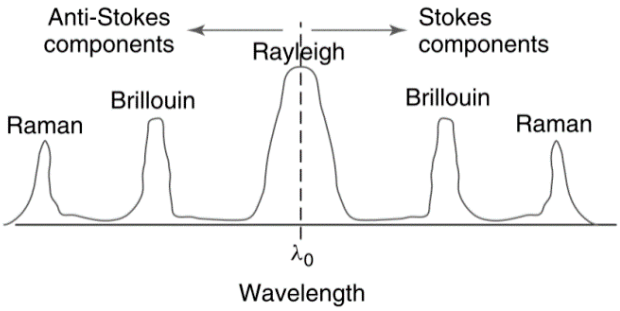

Figure 2.7: Spectrum of backscattering waves showing stokes and anti-stokes components [113].

2.9. Fabry-Pérot sensors

Fabry-Pérot (FP) sensors typically consist of an optically transparent medium with parallel reflectors (mirrors) on either sides. The transmittance is sensitive to the changes in wavelength and/or the spacing between the reflectors. The Free Spectral Range (FSR) of an FP cavity defines the frequency spacing of its transmission peaks and is related to the bandwidth (FWHM - Full Width Half Maximum) by the finesse. For a given finesse, the wavelength resolution can be improved by increasing the mirror distance, but at the cost of reducing the free spectral range. Depending on the reflectance of lossless reflectors, the performance of the sensor is characterized by this finesse and is given by [35]:

$$F = \frac{4R}{(1-R)^2}, \tag{2.5}$$

where F is the finesse and R is the reflectance of the lossless reflectors.

FP sensors can further be divided into intrinsic and extrinsic sensors. Intrinsic sensors consist of a single optical fibre in which two mirrors are fusion spliced either beside each other or one at the free end of the fibre. The change is path length through the region between the mirrors is calculated. As the fusion splicing can deteriorate the cross section of the fibre their application is limited. In contrast to in-line fibre etalons, FBGs generally have a higher mechanical strength [116]. Extrinsic FP sensors, also referred to as cavity sensors, have two optical fibres within a glass tube. One fibre is the lead-in/out and the other is a reflector. The gap between them is a reflecting cavity that is used to measure strain based on the change in cavity length. Changes in the distance of this gap produces a modulation of the output signal. A basic configuration of a typical Fabry-Pérot Sensor is shown in Figure 2.8.

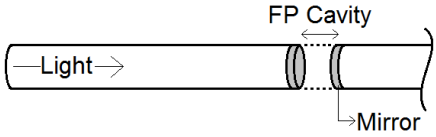

Figure 2.8: Basic configuration of a typical Fabry-Pérot Sensor

2.10. Fibre optic interrogators

Optical interrogators are optoelectric instruments that read sensor data in static or dynamic monitoring applications. Based on the type of interrogator system, various parameters such as strain, displacement and temperature can be measured simultaneously or at different sampling rates. Measurements are done based on the interrogator's design, for example, the interrogator may either measure the time of arrival of the reflected light or the wavelength associated with the light. This information is then converted into measurements in engineering units.

Interferometry based interrogators are known to have high sensitivities [98]. Mach-Zehnder, Michelson, Fabry-Pérot and Sagnac are examples of interferometric designs. The Mach-Zehnder interferometer [117] consists of two fibres whose lengths can be balanced or unbalanced. The first is a sensing fibre which is embedded in the host structure and the second a reference fibre usually in free space or within the instrument housing. Similarly, the Michelson interferometer [117] consists of two fibres but both of them are embedded in the host structure. This makes its use more practical. The ends of these fibres are mirrored and the optical path length of the travelled wave is calculated. When a disturbance is picked up by the sensing fibre there is a change in the optical path length which leads to interference between the light from the two fibres. The downside of these sensors are phase preservation at fibre host interface and their vulnerability to noise. The Sagnac interferometer [117] consists of counter-propagating beams in a ring formed through either multiple mirrors or an optical fibre. When the interferometer is rotated, it brings about a relative phase shift of the counter-propagating beams. Therefore, the fringe pattern is sensitive to any phase difference of the beam and therefore shift based on the angular velocity of the interferometer setup. This is referred to as Sagnac effect.

Different interrogators use different light sources and detectors. The light sources used are generally through spontaneous or stimulated emission [35]. Certain light sources are based on superradiance which is a combination of the two. The power returned from the sensors are monitored using optical detectors. The optical detectors for these sensors are mostly semiconductor or avalanche photodiodes [35]. For certain applications, a photodetector array combined with a diffraction grating is used.

The most common interrogator design for FBG interrogation is based on spectral sensing using a tunable/adjustable Fabry-Pérot bandpass filter, scanning broadband light source and a photodetector [118]. Using this, the amplitude and reflection of

the spectrum is recorded. An example of such a system is the National Instruments (NI) PXI Optical Sensor (OS) module. The PXIe-4844 is an Optical Sensor with a 4 Channel dual-slot data acquisition module for fibre Bragg grating (FBG) optical sensors. The PXIe-4844 features an optical core which combines a high-power, low-noise swept wavelength laser with fibre Fabry-Pérot tunable filter technology [119]. For a multi-channel system like the PXIe-4844 the output of the source is split into different fibres which is in turn connected to an array of couplers or circulators that interact with the fibre that contain the FBGs. Since the Wavelength Division Multiplexing (WDM) scheme is adopted here, a filter is typically used to separate the different wavelengths. The reflected signal from the FBGs is demodulated and converted to an electrical signal which is further processed in the digital domain by using Analog to Digital Converters (ADC).

The working of a sensor pair interferometry interrogator showing the light source and detector along with the light path is explained as follows.

The ZonaSens interrogator by Optics11 is described as it was used as part of this study. This is an example of a Michelson type interferometer. All Michelson type interferometers follow the working principle as depicted in Figure 2.9. A laser beam (coherent light source) passes through a beam-splitter which splits it into two identical beams. One beam is transmitted through the beam-splitter whilst the other gets reflected, as shown in the schematic. Each beam travels down an arm of the interferometer at the end of which are mirrors that reflect them back to the beam-splitter. The incoming beams merge together and the optical phase is measured by amplitude at the detector.

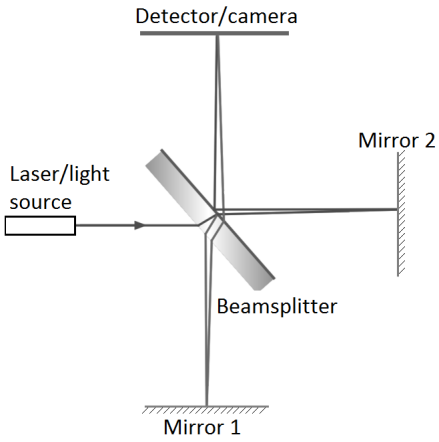

Figure 2.9: Schematic representation of a typical Michelson interferometer working principle.

ZonaSens is a high-tech fibre sensing technology that enables high quality monitoring and measurements of acoustic vibrations. Unlike other FBG interrogators in the market where the gratings are the sensors, ZonaSens uses interferometry

to define discreet measurement zones between gratings in the fibre. Within these zones the system observes minute changes in the length of the fibre zones. These zones become the sensing elements of the system which can be applied in many ways to solve measurement challenges.

A schematic representation of the main Optics11 system components is shown in Figure 2.10 [120]. Different zones can be user-defined based on choice and application. The two gratings of a particular zone work on different wavelengths. Four central wavelengths, 1530 nm, 1540 nm, 1550 nm and 1560 nm have been pre-set by the manufacturer which can be changed if required based on the wavelength of the available sensors. A zone can be a combination of any two of the desired wavelengths.

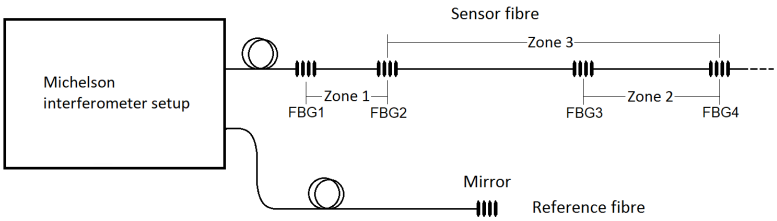

Figure 2.10: Schematic of the Optics11 ZonaSens system along with the sensing zones in the fibre [120].

The yellow (reference) and white (sensor) fibres shown in Figure 2.11, connected to the Optics11 interrogator as the interferometer arms.

The length of a zone between any two FBGs can be from 5 cms to 40 km in length in the ZonaSens interrogator. As the interrogator uses interferometry, it can go up to 750 kHz of sampling giving access to acoustic emission signals. The system is capable of detecting pico-metre changes in the optical path length and has noise levels as low as tens of femtostrains/rt(Hz) [121].

This technology finds applications in Structural Health Monitoring to detect and locate changes on a structure like crack detection in composites, train wheel damage detection, pipeline leakage detection, underwater sonar positioning, to map specific areas for ground exploration purposes, seismic sensing or process monitoring in remote areas [122].

A limitation of the Optics11 ZonaSens interrogator is that only two predefined zones can be interrogated at a single time. In addition to that, shifting the interrogation from a zone to a new one is not instantaneous and may take a few seconds. This currently limits the user to using 2 zones for dynamic real-time sensing applications.

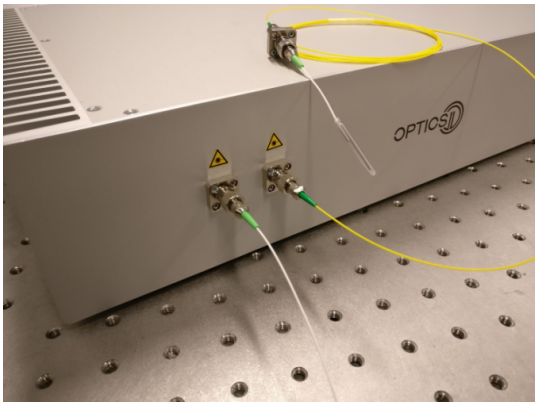

Figure 2.11: The ZonaSens interrogator box along with the reference (yellow) and sensor (white) fibre.

2.11. Summary

This chapter contained the literature review which provides background information to the reader about the direction and focus of this thesis. Within the framework of SHM, the chapter focussed on SHM Levels I and II which pertain to detection and localisation of loads acting on the structure as the focus of this study is on load monitoring and shape sensing of morphing aircraft structure. The most widely used sensors for this purpose were discussed together with their advantages and disadvantages. The usefulness of fibre optic sensors is apparent from the literature which finds applications in various fields for the purpose of SHM. This chapter also discussed the concept, requirement and importance of Structural Health Monitoring with a focus on aircraft and its morphing sections. The selection of fibre optic sensors was justified owing to being fast, reliable, immune to harsh environments and ease of installation. The fundamentals of fibre Bragg grating and fibre Bragg grating pair sensing were presented. These will be utilised in the sensing methodology proposed in this thesis. Based on the literature review, the following chapter talks about areas where more work is required. Furthermore, a novel sensing methodology is proposed and presented as a result of the gaps and limitations of the current available sensing methods.

References

[1] C. Boller. *Structural Health Monitoring-An Introduction and Definitions*. John Wiley and Sons, 2009. isbn: 9780470058220. doi: 10.1002/9780470061626.shm204.

[2] V. Giurgiutiu. *Structural Health Monitoring of Aerospace Composites*. Academic Press, 2015.

[3] R. M. Groves. "Inspection and Monitoring of Composite Aircraft Structures". In: *Reference Module in Materials Science and Materials Engineering* (Dec. 2017). doi: 10.1016/B978-0-12-803581-8.10340-6.

[4] F. Ochieng, C. Hancock, G. Roberts, and J. Le Kernec. "A review of ground-based radar as a noncontact sensor for structural health monitoring of in-field wind turbines blades". In: *Wind Energy* 21.12 (2018), pp. 1435–1449. doi: 10.1002/we.2252.

[5] P. Schubel, R. Crossley, E. Boateng, and J. Hutchinson. "Review of structural health and cure monitoring techniques for large wind turbine blades". In: *Renewable Energy* 51 (2013), pp. 113–123. doi: 10.1016/j.renene.2012.08.072.

[6] S. Mahzan and M. Elghanudi. "Feasibility study of structural health monitoring towards pipeline corrosion monitoring: A review". In: *ARPN Journal of Engineering and Applied Sciences* 11.14 (2016), pp. 8673–8678.

[7] F. Felli, A. Paolozzi, C. Vendittozzi, C. Paris, H. Asanuma, G. De Canio, M. Mongelli, and A. Colucci. "Structural health monitoring of pipelines for environment pollution mitigation". In: *ASME 2015 Conference on Smart Materials, Adaptive Structures and Intelligent Systems, SMASIS 2015* 2 (2015). doi: 10.1115/SMASIS2015-8922.

[8] H.-N. Li, L. Ren, Z.-G. Jia, T.-H. Yi, and D.-S. Li. "State-of-the-art in structural health monitoring of large and complex civil infrastructures". In: *Journal of Civil Structural Health Monitoring* 6.1 (2016), pp. 3–16.

[9] A. Martone, M. Zarrelli, M. Giordano, and J. López-Higuera. *Structural health monitoring in buildings, bridges and civil engineering*. 2013, pp. 21–45. doi: 10.1142/9789814412971_0002.

[10] Z. Su and L. Ye. *Identification of Damage Using Lamb Waves: From Fundamentals to Applications*. Springer, London, 2009. isbn: 978-1-84882-784-4. doi: 10.1007/978-1-84882-784-4.

[11] R. Steenbergen and A. Vrouwenvelder. "Safety philosophy for existing structures and partial factors for traffic loads on bridges". In: *HERON* 55.2 (2010), pp. 123–139. doi: resolver.tudelft.nl/uuid:9addac3c-6fb9-4702-b4fb-415907c741c2.

[12] D. Balageas, C. Fritzen, and A. Güemes. *Structural Health Monitoring*. Wiley-ISTE, 2006. isbn: 978-1-905209-01-9.

[13] K. Worden and J. Dulieu-Barton. "An Overview of Intelligent Fault Detection in Systems and Structures". In: *Structural Health Monitoring-an International Journal - STRUCT HEALTH MONIT* 3 (Mar. 2004), pp. 85–98. doi: 10.1177/1475921704041866.

[14] A. Rytter. "Vibrational Based Inspection of Civil Engineering Structures". Ph.D.-Thesis defended publicly at the University of Aalborg, April 20, 206 pp. PhD thesis. Denmark, 1993.

[15] C. Boller. *Structural Health Monitoring – Its Association and Use*. Ed. by W. Ostachowicz and J. A. Güemes. Springer Vienna, 2013, pp. 1–79.

[16] S. Doebling, C. Farrar, M. Prime, and D. Shevitz. "Damage Identification and Health Monitoring of Structural and Mechanical Systems From Changes in their Vibration Characteristics: A Literature Review". In: *Technical Report No. LA-13070-MS* 30 (1996). doi: 10.2172/249299.

[17] T. de Souza Siqueira Versiani, F. J. Silvestre, A. B. Guimarães Neto, D. A. Rade, R. G. Annes da Silva, M. V. Donadon, R. M. Bertolin, and G. C. Silva. "Gust load alleviation in a flexible smart idealized wing". In: *Aerospace Science and Technology* 86 (2019), pp. 762–774. issn: 1270-9638. doi: https://doi.org/10.1016/j.ast.2019.01.058.

[18] S. Barbarino, O. Bilgen, R. M. Ajaj, M. I. Friswell, and D. J. Inman. "A Review of Morphing Aircraft". In: *Journal of Intelligent Material Systems and Structures* 22.9 (2011), pp. 823–877. doi: 10.1177/1045389X11414084.

[19] T. Nakamura, H. Igawa, and A. Kanda. "Inverse identification of continuously distributed loads using strain data". In: *Aerospace Science and Technology* 23.1 (2012), pp. 75–84. doi: 10.1016/j.ast.2011.06.012.

[20] A. Airoldi, G. Sala, R. Evenblij, C. Koimtzoglou, T. Loutas, G. M. Carossa, P. Mastromauro, and T. Kanakis. "Load Monitoring by Means of Optical Fibres and Strain Gages". In: *Smart Intelligent Aircraft Structures (SARISTU)*. Ed. by P. C. Wölcken and M. Papadopoulos. Springer International Publishing, 2016, pp. 433–469. isbn: 978-3-319-22413-8.

[21] H. Li, L. Zhu, G. Sun, M. Dong, and J. Qiao. "Deflection monitoring of thin-walled wing spar subjected to bending load using multi-element FBG sensors". In: *Optik* 164 (2018), pp. 691–700. issn: 0030-4026. doi: https://doi.org/10.1016/j.ijleo.2018.03.067.

[22] X. Liang, W. Zhang, W. Dai, J. Bo, J. Yao, and Y. Wang. "Real time load monitoring technology of wing structure based on Fiber Bragg grating". In: *9th European Workshop on Structural Health Monitoring, EWSHM 2018* (2018).

[23] H. Kwon, Y. Park, J.-H. Kim, and C.-G. Kim. "Embedded fiber Bragg grating sensor–based wing load monitoring system for composite aircraft". In: *Structural Health Monitoring* 18 (2019), p. 147592171984377. doi: 10.1177/1475921719843772.

[24] Jin-Hyuk, Y. G. Lee, Y. Park, and C.-G. Kim. "Temperature-compensated strain measurement of full-scale small aircraft wing structure using low-cost FBG interrogator". In: *Sensors and Smart Structures Technologies for Civil, Mechanical, and Aerospace Systems 2013*. Ed. by J. P. Lynch, C.-B. Yun, and K.-W. Wang. Vol. 8692. International Society for Optics and Photonics. SPIE, (2013), pp. 751–757. doi: 10.1117/12.2011720.

[25] J.-H. Kim, P. Shrestha, Y. Park, and C.-G. Kim. "Application of fiber Bragg grating sensors in light aircraft: ground and flight test". In: *23rd International Conference on Optical Fibre Sensors*. Ed. by J. M. López-Higuera, J. D. C. Jones, M. López-Amo, and J. L. Santos. Vol. 9157. International Society for Optics and Photonics. SPIE, (2014), pp. 1265–1268. doi: 10.1117/12.2053641.

[26] J.-H. Kim, Y. Park, Y.-Y. Kim, P. Shrestha, and C.-G. Kim. "Aircraft health and usage monitoring system for in-flight strain measurement of a wing structure". In: *Smart Materials and Structures* 24.10 (2015), p. 105003. doi: 10.1088/0964-1726/24/10/105003.

[27] C. A. Sciammarella and F. M. Sciammarella. "Strain Gage Rosettes: Selection, Application and Data Reduction". In: *Experimental Mechanics of Solids* (2012), pp. 111–121. doi: 10.1002/9781119994091.ch5.

[28] E. S. Kocaman, C. J. Keulen, E. Akay, M. Yildiz, H. S. Turkmen, and A. Suleman. "An experimental study on the effect of length and orientation of embedded FBG sensors on the signal properties under fatigue loading". In: *Science and Engineering of Composite Materials* 23.6 (2016), pp. 711–719. doi: 10.1515/secm-2014-0029.

[29] J. Ertveldt, J. Stoev, M. Verbandt, J. Swevers, S. Vanlanduit, and R. Pintelon. "Study of the nonlinear aeroelastic response of a cantilever wing from wind tunnel tests on the Active Aeroelastic Test Bench". In: *International Conference on Noise and Vibration Engineering*. ISMA 2016. (2016).

[30] I. Kressel, J. Balter, I. Sovran, O. Shapira, N. Shemesh, B. Glam, and M. Tur. "High Speed, In-Flight Structural Health Monitoring System For Medium Altitude Long Endurance Unmanned Air Vehicle". In: *7th European Workshop on Structural Health Monitoring*. IFFSTTAR, Inria. (2014). doi: 10.13140/RG.2.1.1846.1287.

[31] I. Kressel, B. Dorfman, Y. Botsev, A. Handelman, J. Balter, A. C. R. Pillai, M. H. Prasad, N. Gupta, A. M. Joseph, R. Sundaram, and M. Tur. "Flight validation of an embedded structural health monitoring system for an unmanned aerial vehicle". In: *Smart Materials and Structures* 24.7 (2015), p. 075022. doi: 10.1088/0964-1726/24/7/075022.

[32] D. Wada, H. Igawa, M. Tamayama, T. Kasai, H. Arizono, H. Murayama, and K. Shiotsubo. "Flight demonstration of aircraft fuselage and bulkhead monitoring using optical fiber distributed sensing system". In: *Smart Materials and Structures* 27 (2018). doi: 10.1088/1361-665X/aaa588.

[33] L. Molent and B. Aktepe. "Review of fatigue monitoring of agile military aircraft". In: *Fatigue & Fracture of Engineering Materials & Structures* 23 (9 2001), pp. 767–785. doi: 10.1046/j.1460-2695.2000.00330.x.

[34] S. Keil. "Fundamentals of strain gage technology". In: *Technology and Practical Use of Strain Gages With Particular Consideration of Stress Analysis Using Strain Gages*. John Wiley & Sons Ltd, 2017. Chap. 2, pp. 17–108. isbn: 9783433606667. doi: 10.1002/9783433606667.ch2.

[35] E. Udd and W. B. S. Jr. *Fiber Optic Sensors: An Introduction for Engineers and Scientists*. Hoboken, N.J.: John Wiley & Sons; 2nd ed., 2011. isbn: 978-0-470-12684-4.

[36] I. Jebáček and M. Horak. "Possibilities and methods of in-flight loading measurement". In: *Aviation* 16 (June 2012), pp. 47–50. doi: 10.3846/16487788.2012.701860.

[37] P. Reymer and A. Leski. "Flight Loads Acquisition for PZL-130 Orlik TCII Full Scale Fatigue Test". In: *Fatigue of Aircraft Structures* 2011 (Aug. 2011). doi: 10.2478/v10164-010-0041-7.

[38] A. Tang, Z. Zhou, and J. Cao. "A technique of landing gear loads calibration with strain gages". In: *Proceedings of the 27th international congress of the aeronautical sciences (ICAS), Nice* (2010).

[39] A. Kurnyta, W. Zieliński, P. Reymer, M. Dziendzikowski, and K. Dragan. "In flight load determination in critical structure elements based on operational load monitoring system". In: *9th European Workshop on Structural Health Monitoring*. EWSHM Manchester, UK. (2018).

[40] A. Kurnyta, W. Zieliński, P. Reymer, K. Dragan, and M. Dziendzikowski. "Numerical and Experimental UAV Structure Investigation by Pre-Flight Load Test". In: *Sensors* 20 (2020), p. 3014. doi: 10.3390/s20113014.

[41] A. Djordjevich and M. Boskovic. "Curvature gauge". In: *Sensors and Actuators: A. Physical* 51.2-3 (1995), pp. 193–198. doi: 10.1016/0924-4247(95)01222-2.

[42] M. J. Gander. "Bend measurement using Bragg gratings in multicore fibre". In: *Fourteenth International Conference on Optical Fiber Sensors*. Ed. by A. G. Mignani and H. C. Lefèvre. Vol. 4185. International Society for Optics and Photonics. SPIE, (2000), pp. 535–538. doi: 10.1117/12.2302270.

[43] M. Gander, D. Macrae, E. Galliot, R. McBride, J. Jones, P. Blanchard, J. Burnett, A. Greenaway, and M. Inci. "Two-axis bend measurement using multicore optical fibre". In: *Optics Communications* 182.1 (2000), pp. 115–121. issn: 0030-4018. doi: https://doi.org/10.1016/S0030-4018(00)00817-8.

[44] G. M. H. Flockhart, W. N. MacPherson, J. S. Barton, J. D. C. Jones, L. Zhang, and I. Bennion. "Two-axis bend measurement with Bragg gratings in multicore optical fiber". In: *Optics Letters* 28.6 (2003), pp. 387–389. doi: 10.1364/OL.28.000387.

[45] P. M. Blanchard, J. G. Burnett, G. R. G. Erry, A. H. Greenaway, P. Harrison, B. Mangan, J. C. Knight, P. S. J. Russell, M. J. Gander, R. McBride, and J. D. C. Jones. "Two-dimensional bend sensing with a single, multi-core optical fibre". In: *Smart Materials and Structures* 9.2 (2000), pp. 132–140. doi: 10.1088/0964-1726/9/2/302.

[46] A. Rauf, J. Zhao, and B. Jiang. "High-sensitivity bend angle measurements using optical fiber gratings". In: *Applied Optics* 52.21 (2013), pp. 5072–5078. doi: 10.1364/AO.52.005072.

[47] F. Parent, S. Loranger, K. K. Mandal, V. L. Iezzi, J. Lapointe, J.-S. Boisvert, M. D. Baiad, S. Kadoury, and R. Kashyap. "Enhancement of accuracy in shape sensing of surgical needles using optical frequency domain reflectometry in optical fibers". In: *Biomed. Opt. Express* 8.4 (2017), pp. 2210–2221. doi: 10.1364/BOE.8.002210.

[48] Y. Mizutani and R. M. Groves. "Multi-Functional Measurement Using a Single FBG Sensor". In: *Experimental Mechanics* 51 (Nov. 2011), pp. 1489–1498. doi: 10.1007/s11340-011-9467-2.

[49] M. Davis, A. Kersey, J. Sirkis, and E. Friebele. "Shape and vibration mode sensing using a fiber optic Bragg grating array". In: *Smart Materials and Structures* 5 (Jan. 1999), p. 759. doi: 10.1088/0964-1726/5/6/005.

[50] K.-C. Chuang, H.-T. Liao, and C.-C. Ma. "Dynamic Sensing Performance of a Point-Wise Fiber Bragg Grating Displacement Measurement System Integrated in an Active Structural Control System". In: *Sensors (Basel, Switzerland)* 11 (Dec. 2011), pp. 11605–28. doi: 10.3390/s111211605.

[51] R. T. Jones, D. G. Bellemore, T. A. Berkoff, J. S. Sirkis, M. A. Davis, M. A. Putnam, E. J. Friebele, and A. D. Kersey. "Determination of cantilever plate shapes using wavelength division multiplexed fiber Bragg grating sensors and a least-squares strain-fitting algorithm". In: *Smart Materials and Structures* 7.2 (1998), pp. 178–188. doi: 10.1088/0964-1726/7/2/005.

[52] P. Heaney, T. Ivanco, and O. Bilgen. "Distributed Sensing of a Cantilever Beam and Plate using a Fiber Optic Sensing System". In: *Aerodynamic-Structural Dynamics Interaction I*. Atlanta, GA. AIAA 2018-3482, (2018). doi: 10.2514/6.2018-3482.

[53] Q. Lei, Y. Shenfang, W. Qiang, S. Yajie, and Y. Weiwei. "Design and Experiment of PZT Network-based Structural Health Monitoring Scanning System". In: *Chinese Journal of Aeronautics* 22.5 (2009), pp. 505–512. issn: 1000-9361. doi: https://doi.org/10.1016/S1000-9361(08)60133-8.

[54] D. Ai, H. Luo, C. Wang, and H.-p. Zhu. "Monitoring of the load-induced RC beam structural tension/compression stress and damage using piezoelectric transducers". In: *Engineering Structures* 154 (2018), pp. 38–51. doi: 10.1016/j.engstruct.2017.10.046.

[55] X. Wang and Q. Zhang. "Three-dimensional shape and deformation measurement of flapping-wing micro air vehicle". In: *Guangxue Xuebao/Acta Optica Sinica* 33 (2013). doi: 10.3788/AOS201333.s212003.

[56] M. Deetjen, A. Biewener, and D. Lentink. "High-speed surface reconstruction of a flying bird using structured light". In: *Journal of Experimental Biology* 220.11 (2017), pp. 1956–1961. doi: 10.1242/jeb.149708.

[57] M. R. Yu, Y. J. Zhang, and D. Zhang. "Review of 3D Shape Measurement Using Fringe Projection Techniques". In: *Frontiers of Manufacturing Science and Measuring Technology II*. Vol. 503. Advanced Materials Research. Trans Tech Publications Ltd, (2012), pp. 1437–1440. doi: 10.4028/www.scientific.net/AMR.503-504.1437.

[58] A. Anand, V. K. Chhaniwal, P. Almoro, G. Pedrini, and W. Osten. "Shape and deformation measurements of 3D objects using volume speckle field and phase retrieval". In: *Optics Letters* 34.10 (May 2009), pp. 1522–1524. doi: 10.1364/OL.34.001522.

[59] T. H. T. Chan, D. B. Ashebo, H. Tam, Y. Yu, T. Chan, P. Lee, and E. P. Gracia. "Vertical Displacement Measurements for Bridges Using Optical Fiber Sensors and CCD Cameras — A Preliminary Study". In: *Structural Health Monitoring* 8.3 (May 2009), pp. 243–249. doi: 10.1177/1475921708102108.

[60] H. Babovsky, M. Grosse, J. Buehl, A. Kiessling, and R. Kowarschik. "Stereophotogrammetric 3D shape measurement by holographic methods using structured speckle illumination combined with interferometry". In: *Optics Letters* 36.23 (Dec. 2011), pp. 4512–4514. doi: 10.1364/OL.36.004512.

[61] P. Li, Y. Liu, and L. Jinsong. "A new deformation monitoring method for a flexible variable camber wing based on fiber Bragg grating sensors". In: *Journal of Intelligent Material Systems and Structures* 25 (Aug. 2013), pp. 1644–1653. doi: 10.1177/1045389X13510220.

[62] H. Kim, J.-H. Han, and H. Bang. "Real-time deformed shape estimation of a wind turbine blade using distributed fiber Bragg grating sensors". In: *Wind Energy* 17 (2013). doi: 10.1002/we.1644.

[63] W. Ko, W. L. Richards, and V. Fleischer. "Applications of KO Displacement Theory to the Deformed Shape Predictions of the Doubly-Tapered Ikhana Wing". In: *NASA/ TP-2009-214652* (2009).

[64] C. V. Jutte, W. L. Ko, C. A. Stephens, J. A. Bakalyar, and W. L. Richards. "Deformed Shape Calculation of a Full-Scale Wing Using Fiber Optic Strain Data from a Ground Loads Test". In: *NASA/TP-2011-215975* (2011).

[65] M. Gherlone, P. Cerracchio, and M. Mattone. "Shape sensing methods: Review and experimental comparison on a wing-shaped plate". In: *Progress in Aerospace Sciences* 99 (2018), pp. 14–26. issn: 0376-0421. doi: https://doi.org/10.1016/j.paerosci.2018.04.001. url: https://www.sciencedirect.com/science/article/pii/S037604211730221X.

[66] N. Lawson, R. Correia, S. W. James, M. Partridge, S. Staines, J. Gautrey, K. Garry, J. Holt, and R. P. Tatam. "Development and application of optical fibre strain and pressure sensors for in-flight measurements". In: *Measurement Science and Technology* 27 (2016). doi: 10.1088/0957-0233/27/10/104001.

[67] A. Concilio, I. Dimino, L. Lecce, and R. Pecora. *Morphing wing technologies: Large commercial aircraft and civil helicopters*. Butterworth-Heinemann, 2018. isbn: 978-0-08-100964-2.

[68] I. Chopra. "Review of state of art of smart structures and integrated systems". In: *AIAA journal* 40.11 (2002), pp. 2145–2187. doi: 10.2514/2.1561.

[69] H. Pfeiffer and M. Wevers. "The European Project "Aircraft Integrated Structural Health Assessment II"". In: *Innovation for Sustainable Aviation in a Global Environment: Proceedings of the Sixth European Aeronautics Days, Madrid* (2012). doi: 10.3233/978-1-61499-063-5-307.

[70] T. A. Weisshaar. "Morphing aircraft systems: historical perspectives and future challenges". In: *Journal of Aircraft* 50.2 (2013), pp. 337–353. doi: 10.2514/1.C031456.

[71] P. C. Wölcken and M. Papadopoulos. *Smart intelligent aircraft structures (SARISTU): proceedings of the final project conference*. Springer, 2015. isbn: 9783319224138.

[72] J. Sun, Q. Guan, Y. Liu, and J. Leng. "Morphing aircraft based on smart materials and structures: A state-of-the-art review". In: *Journal of Intelligent material systems and structures* 27.17 (2016), pp. 2289–2312. doi: 10.1177/1045389X16629569.

[73] D. Li, S. Zhao, A. Da Ronch, J. Xiang, J. Drofelnik, Y. Li, L. Zhang, Y. Wu, M. Kintscher, H. P. Monner, A. Rudenko, S. Guo, W. Yin, J. Kirn, S. Storm, and R. D. Breuker. "A review of modelling and analysis of morphing wings". In: *Progress in Aerospace Sciences* 100 (2018), pp. 46–62. issn: 0376-0421. doi: https://doi.org/10.1016/j.paerosci.2018.06.002.

[74] Y. Yaman. "Morphing Wings and Control Surfaces: A New Approach in Aircraft Design". In: *4th Conference on Mechanisms, Transmissions and Applications, MeTrApp*. Vol. 52. June (2018), pp. 3–10. isbn: 978-3-319-60701-6. doi: 10.1007/978-3-319-60702-3_1.

[75] W. Akl, S. Poh, and A. Baz. "Wireless and distributed sensing of the shape of morphing structures". In: *Sensors and Actuators A: Physical* 140.1 (2007), pp. 94–102. issn: 0924-4247. doi: https://doi.org/10.1016/j.sna.2007.06.026.

[76] H. Xu, J. Zeng, D. Liang, X. Wang, and H. Liu. "Numerical simulation and experimental study of strain field for morphing wings based on distributed fiber bragg grating sensor network". In: *Hangkong Xuebao/Acta Aeronautica et Astronautica Sinica* 32.10 (2011), pp. 1842–1850.

[77] G. W. Reich and B. P. Sanders. "Structural shape sensing for morphing aircraft". In: *Smart Structures and Materials 2003: Smart Structures and Integrated Systems*. Ed. by A. M. Baz. Vol. 5056. International Society for Optics and Photonics. SPIE, (2003), pp. 134–141. doi: 10.1117/12.483468.

[78] N. S. Butler, W. Su, K. S. T. Magar, and G. W. Reich. "Estimation of morphing airfoil shape and aerodynamic load using artificial hair sensors". In: *Sensors and Smart Structures Technologies for Civil, Mechanical, and Aerospace Systems 2016*. Ed. by J. P. Lynch. Vol. 9803. International Society for Optics and Photonics. SPIE, (2016), pp. 659–674. doi: 10.1117/12.2219520.

[79] P. Li, Y. Liu, and J. Leng. "A new deformation monitoring method for a flexible variable camber wing based on fiber Bragg grating sensors". In: *Journal of Intelligent Material Systems and Structures* 25.13 (2014), pp. 1644–1653. doi: 10.1177/1045389X13510220.

[80] G. Sun, Y. Hu, Y. He, Y. Song, M. Dong, and L. Zhu. "Stretchable sensing skin with S-shape multicore optical fiber implantation for morphing flight vehicles". In: *Optik* 199 (2019). doi: 10.1016/j.ijleo.2019.163088.

[81] Y. He, L. Zhu, G. Sun, F. Meng, and Y. Song. "Fiber Brag grating monitoring of a morphing wing based on a polyvinyl chloride reinforced silicone substrate". In: *Optical Fiber Technology* 50 (2019), pp. 145–153. doi: 10.1016/j.yofte.2019.03.019.

[82] G. Sun, Y. Wu, H. Li, and L. Zhu. "3D shape sensing of flexible morphing wing using fiber Bragg grating sensing method". In: *Optik* 156 (2018), pp. 83–92. doi: 10.1016/j.ijleo.2017.10.159.

[83] R. Evenblij, F. Kong, C. Koimtzoglou, M. Ciminello, I. Dimino, and A. Concilio. "Shape Sensing for Morphing Structures Using Fiber Bragg Grating Technology". In: *Smart Intelligent Aircraft Structures (SARISTU)*. Jan. 2016, pp. 471–491. isbn: 978-3-319-22412-1. doi: 10.1007/978-3-319-22413-8_21.

[84] J. Smoker and A. Baz. "Monitoring the bending and twist of morphing structures". In: *Sensors and Smart Structures Technologies for Civil, Mechanical, and Aerospace Systems 2008*. Ed. by M. Tomizuka. Vol. 6932. International Society for Optics and Photonics. SPIE, (2008), pp. 567–577. doi: 10.1117/12.776433. url: https://doi.org/10.1117/12.776433.

[85] Y. He, M. Dong, G. Sun, F. Meng, Y. Song, and L. Zhu. "Shape monitoring of morphing wing using micro optical sensors with different embedded depth". In: *Optical Fiber Technology* 48 (2019), pp. 179–185. doi: 10.1016/j.yofte.2018.12.025.

[86] M. Scheerer, Z. Djinovic, and M. Schueller. "Fiber optic system for deflection and damage detection in morphing wing structures". In: vol. 8692. Apr. (2013), 86922Q. doi: 10.1117/12.2009256.

[87] M. C. Tomić, Z. V. Djinović, M. Scheerer, and S. J. Petricevic. "Measurement of morphing wing deflection by a cross-coherence fiber optic interferometric technique". In: *Smart Materials and Structures* 27.1 (2018), p. 015017. doi: 10.1088/1361-665x/aa9afe.

[88] M. Schwartz. *Encyclopedia of Smart Materials, 2 Volume Set*. New York: John Wiley & Sons, Inc., 2002. isbn: 0-471-17780-6.

[89] Q. Zhu, C. Xu, and G. Yang. "Experimental research on damage detecting in composite materials with FBG sensors under low frequency cycling". In: *International Journal of Fatigue* 101.P1 (2017), pp. 61–66. doi: 10.1016/j.ijfatigue.2017.03.034.

[90] S. Waite and G. Sage. "The failure of optical fibres embedded in composite materials". In: *Composites* 19.4 (1988), pp. 288–294. issn: 0010-4361. doi: 10.1016/0010-4361(88)90005-5.

[91] L. Sim and G. Zhou. "Designing, manufacturing, and testing of embedded EFPI strain sensor for damage detection of smart composite beams". In: *Proceedings of SPIE - The International Society for Optical Engineering* 5852 (2005). doi: 10.1117/12.621417.

[92] D. C. Betz, G. Thursby, B. Culshaw, and W. J. Staszewski. "Structural Damage Location with Fiber Bragg Grating Rosettes and Lamb Waves". In: *Structural Health Monitoring* 6.4 (2007), pp. 299–308. doi: 10.1177/1475921707081974.

[93] E. S. Kocaman, E. Akay, C. Yilmaz, H. Turkmen, B. Misirlioglu, A. Suleman, and M. Yildiz. "Monitoring the Damage State of Fiber Reinforced Composites Using an FBG Network for Failure Prediction". In: *Materials* 10 (2017), p. 32. doi: 10.3390/ma10010032.

[94] J. Leng and A. Asundi. "Non-destructive evaluation of smart materials by using extrinsic Fabry–Perot interferometric and fiber Bragg grating sensors". In: *NDT & E International* 35 (2002), pp. 273–276. doi: 10.1016/S0963-8695(01)00060-3.

[95] K. Majewska, S. Opoka, P. Kudela, and W. Ostachowicz. "Novel FBG rosette for determining impact location in thin plate-like structure". In: *Journal of Physics: Conference Series* 628 (2015). doi: 10.1088/1742-6596/628/1/012118.

[96] B. Rocha, C. Silva, and A. Suleman. "Development of a PZT Phased Array and FBG Network for Structural Health Monitoring Based in Guided Lamb Waves". In: *CEAS Aeronautical Journal* 4 (2013). doi: 10.1007/s13272-013-0066-z.

[97] F. Lambinet and Z. Sharif Khodaei. "Damage Detection in Composite Skin Stiffener with Hybrid PZT-FO SHM System". In: *Key Engineering Materials* 754 (2017), pp. 367–370. doi: 10.4028/www.scientific.net/KEM.754.367.

[98] Y. Okabe and Q. Wu. "Using optical fibers for ultrasonic damage detection in aerospace structures". In: *Structural Health Monitoring (SHM) in Aerospace Structures*. Ed. by F.-G. Yuan. Woodhead Publishing, Mar. 2016. Chap. 4, pp. 95–118. isbn: 9780081001486. doi: 10.1016/B978-0-08-100148-6.00004-4.

[99] F. Idachaba, D. Ike, and O. Evwieroghene. In: *Future Trends in Fiber Optics Communication*. Vol. 1. Proceedings of the World Congress on Engineering. WCE, July (2014), pp. 438–442. isbn: 978-988-19252-7-5.

[100] M.-J. Li. "Optical Fiber Evolution Over the Past 5 Decades". In: *Frontiers in Optics / Laser Science*. Optical Society of America, Jan. (2020), FM4D.1. doi: 10.1364/FIO.2020.FM4D.1.

[101] R. Bogue. "Fibre optic sensors: A review of today's applications". In: *Sensor Review* 31 (Sept. 2011), pp. 304–309. doi: 10.1108/02602281111169703.

[102] R. Kashyap. "Fabrication of Bragg Gratings". In: *Fiber Bragg Gratings (Second Edition)*. Ed. by R. Kashyap. Academic Press, Dec. 2010. Chap. 3, pp. 53–118. isbn: 9780123725790. doi: 10.1016/B978-0-12-372579-0.00003-X.

[103] L. Fazzi and R. M. Groves. "Demodulation of a tilted fibre Bragg grating transmission signal using α-shape modified Delaunay triangulation". In: *Measurement* 166 (2020), p. 108197. doi: 10.1016/j.measurement.2020.108197.

[104] H. Guo, G. Xiao, N. Mrad, and J. Yao. "Fiber Optic Sensors for Structural Health Monitoring of Air Platforms". In: *Sensors (Basel, Switzerland)* 11 (2011), pp. 3687–705. doi: 10.3390/s110403687.

[105] T. Erdogan. "Fiber Grating Spectra". In: *Lightwave Technology, Journal of* 15 (1997), pp. 1277–1294. doi: 10.1109/50.618322.

[106] S. W. James and R. P. Tatam. "Optical fibre long-period grating sensors: characteristics and application". In: *Measurement Science and Technology* 14.5 (2003), R49–R61. doi: 10.1088/0957-0233/14/5/201.

[107] C. E. Campanella, A. Cuccovillo, C. Campanella, A. Yurt, and V. Passaro. "Fibre Bragg Grating Based Strain Sensors: Review of Technology and Applications". In: *Sensors* 18 (2018), p. 3115. doi: 10.3390/s18093115.

[108] K. Hill and G. Meltz. "Fiber Bragg grating technology fundamentals and overview". In: *Journal of Lightwave Technology* 15.8 (1997), pp. 1263–1276. doi: 10.1109/50.618320.

[109] A. Kersey, M. Davis, H. Patrick, M. Leblanc, K. Koo, C. Askins, M. Putnam, and E. Friebele. "Fiber Grating Sensors". In: *Lightwave Technology, Journal of* 15 (1997), pp. 1442–1463. doi: 10.1109/50.618377.

[110] A. D. Kersey. "A Review of Recent Developments in Fiber Optic Sensor Technology". In: *Optical Fiber Technology* 2.3 (1996), pp. 291–317. issn: 1068-5200. doi: https://doi.org/10.1006/ofte.1996.0036.

[111] J. S. Sirkis, D. D. Brennan, M. A. Putman, T. A. Berkoff, A. D. Kersey, and E. J. Friebele. "In-line fiber étalon for strain measurement". In: *Optics Letters* 18.22 (1993), pp. 1973–1975. doi: 10.1364/OL.18.001973.

[112] G. Gruca and N. Rijnveld. "Optical Fiber-Based Sensor System". In: *Patent: WO 2017/026896 A1* (Feb. 2017). url: https://patents.google.com/patent/WO2017026896A1/en?oq=WO2017%2f026896A1.

[113] K. Peters. "Intensity-, Interferometric-, and Scattering-Based Optical-Fiber Sensors". In: *Encyclopedia of Structural Health Monitoring*. Ed. by C. Boller, F. Chang, and Y. Fujino. Wiley Online Library, NY, 2009. Chap. 60. isbn: 9780470061626. doi: 10.1002/9780470061626.shm026.

[114] X. Bao, D. Webb, and D. Jackson. "Combined distributed temperature and strain sensor based on Brillouin loss in an optical fiber". In: *Optics Letters* 19 (1994), p. 141. doi: 10.1364/OL.19.000141.

[115] Q. Cui, S. Pamukcu, A. Lin, W. Xiao, D. Herr, J. Toulouse, and M. Pervizpour. "Distributed Temperature Sensing System Based on Rayleigh Scattering BOTDA". In: *Sensors Journal, IEEE* 11 (2011), pp. 399–403. doi: 10.1109/JSEN.2010.2066558.

[116] Y.-J. Rao. "In-fibre Bragg grating sensors". In: *Measurement Science and Technology* 8.4 (1997), pp. 355–375. doi: 10.1088/0957-0233/8/4/002.

[117] B. H. Lee, Y. H. Kim, K. S. Park, J. B. Eom, M. J. Kim, B. S. Rho, and H. Y. Choi. "Interferometric Fiber Optic Sensors". In: *Sensors* 12.3 (2012), pp. 2467–2486. issn: 1424-8220. doi: 10.3390/s120302467.

[118] A. D. Kersey, T. A. Berkoff, and W. W. Morey. "Multiplexed fiber Bragg grating strain-sensor system with a fiber Fabry–Perot wavelength filter". In: *Optics Letters* 18.16 (Aug. 1993), pp. 1370–1372. doi: 10.1364/OL.18.001370.

[119] National Instruments. *PXIe-4844: PXI Universal Input Module*. [Online; accessed 10-April-2018]. url: https://www.ni.com/nl-nl/support/model.pxie-4844.html.

[120] Optics11. *ZonaSens: User manual*. Version 1.2. (2018).

[121] Optics11. *ZonaSens: Factsheet*. ZonaSens Development Kit. (2017).

[122] Optics11. *Industrial Sensing*. [Online; accessed 10-April-2018]. url: https://optics11.com/products/industrialsensing/.

3

Research Workflow

If we would have new knowledge,
we must get a whole world of new questions.

Susanne K. Langer

It is imperative to first establish a strategic workflow for this research work. In this chapter a set of research questions are devised that transpire from the background knowledge and the research gaps raised. Within the already available fibre optic techniques an identification is made for the potential of a higher performing SHM tool. A proposal is then made to have a reliable, robust and cost effective sensing methodology for real time monitoring of morphing structures with a simultaneous focus on the SmartX morphing wing demonstrator. Secondary and sub-research questions are framed to address each aspect of the principle research question. A structured workflow is then adopted in this thesis by dividing it into four levels that take the reader through a stepwise increment in complexity.

3.1. Exploring gaps

On reviewing the recent work and advancements of aircraft Structural Health Monitoring, it is evident from the previous chapter (Chapter 2) that the most sought-after technique is fibre optic sensing. This is the preferred technology for the application of this study whilst conforming to the sensor evaluation requirements [1] as elaborated in Section 2.5. Fibre optic sensors are preferred as they have a higher potential than other sensing techniques for load monitoring and shape sensing on morphing aircraft wings given their advantages which include lightweight, high sensitivity, immunity to EMI and harsh environments and being inconspicuous when installed [2]. Being inconspicuous in nature also comes with handling challenges (for bare optical fibres) but it is fairly easy for those installing them to get accustomed to handling them. Moreover, as morphing structures undergo multi-axis bending and twisting they are strong yet flexible enough to undergo and withstand the deformation loads.

In order to have more readings and data points it is noticed that a large number of sensors are being used along with multiple fibres. Different sensor configurations are also seen that require intricate patterns and multiple sensing points (Figure 2.4). There are also cases of single fibres that are run all over the structure that contain an array of sensors. A justified and optimised sensor layout is preferred rather than having a large number of sensors hoping to gather large amounts of data. Overall, the reliability of the monitoring system is reduced when a large number of sensors are used [3]. At times this could result in an increase in inaccurate data and this would be a reason for users to avoid this sort of monitoring systems. Having a large number of sensors requires more processing capabilities to process the large amount of data that would, apart from being more expensive, eventually take us away from the definition of a simple system.

These observations lead me to question if there is a simpler monitoring system that delivers the required information without involving a large number of sensors but at the same time is not expensive. A follow-up question arises that if the number of sensors have to be reduced, how low can the sensor count eventually be to adequately collect the information required with sufficient accuracy.

To be able to approach these questions, an appropriate methodology must first be established. This sensing methodology should basically require discreet strain measurements on the surface of wing. The aim is to be able to monitor the in-flight loads and to measure the shape of the morphing aircraft surfaces. Monitoring the loads on the wing would provide essential information for optimising the flight to maintain it within its structural design limits [4, 5] and keep a check on the structural integrity of the morphing section throughout its service life [6].

3.2. Research questions

Before diving into the feasibility tests and the experimental campaign, it is essential to establish a principle research question within the framework of this study. The principle research question is split into different sub research questions that are approached and answered individually. This is also done to have a fluid

transition between each of the following chapters and to have a clear workflow as will be explained in the following section.

The means required to realise the goals of the thesis elaborated in Section 1.6 can be summarised in one Principle Research Question (PRQ):

⋆ **How can a robust sensing system be developed for multi-functional real-time monitoring of adaptive aerospace structures that is economical and does not require processing of a large amount of data?**

Further, in order to answer the aforementioned principle research question, a list of secondary research questions (RQ) along with their sub-questions have been formulated to break down the study into smaller topics.

RQ1 How can a multimodal methodology be chosen that combines spectral and interferometric sensing to measure the load and shape of a morphing wing?

From the literature review this refers to the usage of either a large number of sensors or complex configurations. RQ1 deals with the identification of a higher performing fibre optic sensing methodology that is simple, less computational intensive to analyse the data and would require the least number of gratings for sensing. The aim of the sensing system is to be able to estimate the load and monitor the shape of the structure. This will be investigated by combining interferometry and spectral Bragg grating principles. The feasibility of the proposed method will be investigated on a cantilever beam for 1 dimensional sensing to estimate the position and magnitude of a load acting upon it. The estimation of the beam deflection is also done by verification with the analytical models. This RQ will be addressed in Chapter 4.

RQ2 How can the hybrid sensing methodology be used for multi-axis monitoring including the estimation of position and magnitude of an arbitrary load?

Much of the literature review refers to the estimation of loading magnitude but not of information on the position of the load. RQ2 deals with the application of the hybrid sensing approach for 2 dimensional sensing that involves both position and magnitude sensing. The feasibility of the approach demonstrated in RQ1 is tested for a cantilever plate that includes an extra parameter, viz., twist. This RQ deals with the demonstration of the position and magnitude estimation of an arbitrary load on the surface of the cantilever plate. The possibility of checking for structural irregularities in the plate is also studied. This RQ will be addressed in Chapter 5.

RQ3 How can the hybrid sensing methodology be used for deflection monitoring of complex morphing structures that cannot be easily modelled?

From the literature review this refers to a combination of RQ1 and RQ2 for complex morphing wings. RQ3 deals with the application of the hybrid sensing approach for monitoring of morphing wing sections. Analytical models do not need to be developed for the complex morphing mechanism and at the same time numerical

models may not completely capture the structural irregularities except those that are visible. A morphing wing undergoes different bend and twist cases and it is the shape of the morphing wing that is of interest. This RQ will be addressed in Chapter 6.

RQ4 How can the fibre optic sensing methodology be integrated and function in the SmartX morphing wing demonstrator?

From the literature review this refers to the earlier works related to morphing monitoring focussed only on deflection estimation and sensing technologies, and not on utilisation of the morphing data as an input to the controller. RQ4 deals with the application of the hybrid sensing approach on a full scale composite morphing wing demonstrator. It concerns itself with the demonstration of the feasibility of having a single optical fibre system that address the different aspects of SHM by combining the findings from the previous RQs as well as the investigation of the actuator effectiveness during morphing. This RQ will be addressed in Chapter 7.

3.3. Methodology

With respect to the motivation and goal of the work elaborated in Section 1.6, the aim of the research to be carried out is on the design and development of a novel sensing approach for the monitoring of morphing aircraft wings. Fibre optic sensors, and in particular fibre Bragg grating sensors are selected (see Section 2.5) as the preferred sensing technology for this application.

For this work a strategy is required to reduce the number of local measurement points which will in turn reduce the number of grating sensors. The idea is to use the least number of gratings but at the same time to cover a larger surface area. An approach is identified that is a fusion between two sensing technologies that deal with point measurements and a measurement along a specified line. For this, point strain measurements from the gratings and displacement measurements between any two given gratings are utilised considering them as a long but artificial Fabry-Pérot cavity (Section 2.9). Therefore, a proposal is made for a novel way for measuring the loads and the shape, which includes the combination of FBG spectral sensing (Section 2.7.1) and multiple FBG-Pair interferometric sensing (Section 2.7.2), which is hereon referred to as the multimodal or hybrid sensing approach.

The multimodal sensing principle follows a two-step FBG measurement procedure. It involves the combination of FBG spectral sensing and FBG-Pair interferometric sensing. Under the topic of load monitoring and shape sensing, this sensing principle is aimed at demonstrating:

- Loading position; locating the position of an arbitrary localised load at an arbitrary location on the surface of the structure.

- Loading magnitude; estimating the degree or magnitude of an arbitrary load on the surface of the structure, and

- Deflection estimation; estimating the overall deflection of the structure due an arbitrary localised or distributed load.

The local strain from each of the FBGs is calculated through the spectral shift, according to equation 2.2. Figure 3.1 shows an example spectra obtained when the FBG contained in the sensing fibre is loaded. A wavelength shift in the Bragg peak is noticed which can be converted to strain.

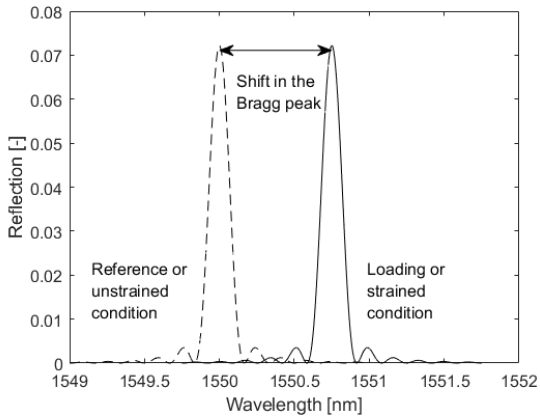

Figure 3.1: Example spectra of the FBG, indicating the shift in Bragg reflection peak due to the fiber undergoing tension

The second step involves the calculation of the optical path length between two given FBGs by measuring the displacement in terms of strain through equation 2.4. Figure 3.2 shows an example spectra obtained when the length between two FBGs is loaded. This example depicts four scenarios. The fibre is initially unstrained, followed by a tension load, a pause and then release of the load, bringing it back to the original unstrained condition.

These graphs and their supporting information are taken from preliminary tests.

As multiple FGBs are incorporated in the multimodal sensing approach, the Wavelength Division Multiplexing (WDM) scheme is used to distinguish and identify the FBGs from one another. After the methodology of the multimodal sensing approach is established, it is necessary to evaluate its performance and to test its feasibility. Detailed algorithms involving position, magnitude and deflection estimation will be discussed in the following chapters.

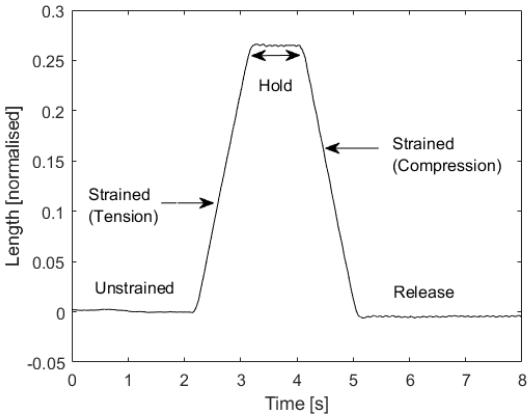

Figure 3.2: Example spectra of the FBG pair, indicating the sensing fiber undergoing gradual tension and compression

3.4. Research process

The goal identified in section 1.6 will be realised by first breaking it down into four complexity levels under the framework of this study. The four complexity levels are as follows:

- Level I: This is the initial level that focusses on the feasibility study of the hybrid fibre optic sensing method as a potential load monitoring and shape sensing tool. This level deals with a simple beam bending case and the estimation of loading position and magnitude in one axis. The minimum number of fibres and sensors will also be discussed.

- Level II: This level goes a step higher by considering the estimation of loading position and magnitude in two axes. For this, a cantilever plate will be used which undergoes both bending and twisting under load. The number and the position of fibres on the plate and the sensors in the fibre are also discussed.

- Level III: This level explores the possibility of monitoring a mock-up of a morphing wing. This wing will be constructed of aluminium for ease of use and undergoes multiple morphing cases. In each case, the potential of the fibre optic sensing system in estimating the deflection and the final shape of the wing will be demonstrated.

- Level IV: The final level deals with implementing and integrating all the findings from the previous levels. This is the highest complexity level that deals with the monitoring of a full scale composite morphing wing in the wind tunnel.

For a structured flow, these complexity levels are aligned with the research questions discussed in Section 3.2. In this way, each technical chapter would each be focussed on answering a sub research question in order. For example, the first technical chapter deals with the Complexity Level (CL) I, which will answer Research Question (RQ) 1, and so forth, as explained in Table 3.1.

Table 3.1: Relationship and alignment of the chapters with the Complexity Levels (CL) and Research Questions (RQ).

Thesis Chapter	Technical Chapter	CL	RQ
4	1	I	1
5	2	II	2
6	3	III	3
7	4	IV	4

The research process is hence guided with steps of increasing complexity to ensure stepwise development and understanding. Instead of jumping directly to morphing wing structures, the study aims to first establish a good foundation of the novel fibre optic sensing methodology and to further build on it. This will help the reader in understanding better the development of a robust SHM tool for different applications. Figure 3.3 shows the building blocks followed within the framework of this study. In hindsight, another benefit of this was that the sensing methodology proposed was able to measure parameters that were not expected and these turned out to be beneficial for the overall monitoring of the morphing wing.

It is worthwhile to note that even though new algorithms were developed in the pursuit of establishing and validating the hybrid sensing method, the feasibility and demonstration of the proposed sensing method for different applications was always kept as a focus. Because of this, a detailed study on computationally optimising the algorithms was not carried out as this was not the focus of the work.

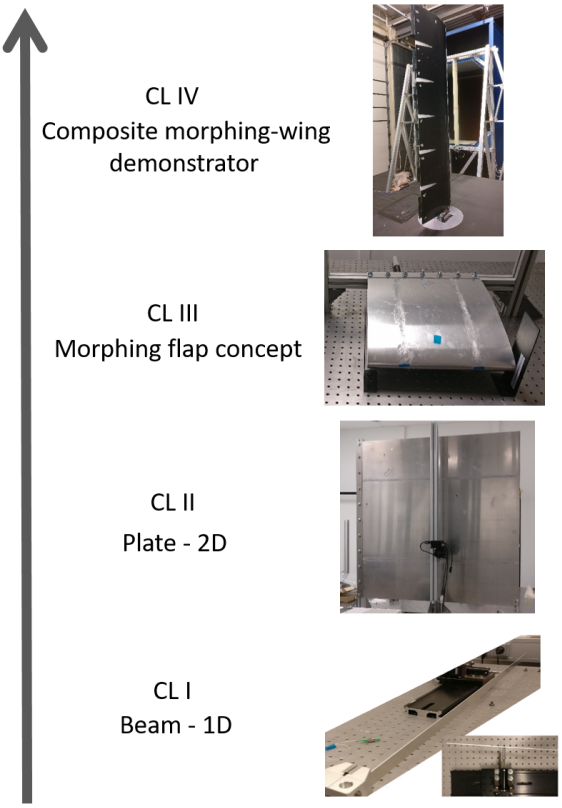

Figure 3.3: The building blocks in terms of complexity (CL) followed within the framework of this study.

References

[1] M. Schwartz. *Encyclopedia of Smart Materials, 2 Volume Set*. New York: John Wiley & Sons, Inc., 2002. isbn: 0-471-17780-6.

[2] E. Udd and W. B. S. Jr. *Fiber Optic Sensors: An Introduction for Engineers and Scientists*. Hoboken, N.J.: John Wiley & Sons; 2nd ed., 2011. isbn: 978-0-470-12684-4.

[3] C. Boller. "Next generation Structural Health Monitoring and its integration into aircraft design". In: *Int. J. Systems Science* 31 (2000), pp. 1333–1349. doi: 10.1080/00207720050197730.

[4] T. Nakamura, H. Igawa, and A. Kanda. "Inverse identification of continuously distributed loads using strain data". In: *Aerospace Science and Technology* 23.1 (2012), pp. 75–84. doi: 10.1016/j.ast.2011.06.012.

[5] T. de Souza Siqueira Versiani, F. J. Silvestre, A. B. Guimarães Neto, D. A. Rade, R. G. Annes da Silva, M. V. Donadon, R. M. Bertolin, and G. C. Silva. "Gust load alleviation in a flexible smart idealized wing". In: *Aerospace Science and Technology* 86 (2019), pp. 762–774. issn: 1270-9638. doi: https://doi.org/10.1016/j.ast.2019.01.058.

[6] A. Airoldi, G. Sala, R. Evenblij, C. Koimtzoglou, T. Loutas, G. M. Carossa, P. Mastromauro, and T. Kanakis. "Load Monitoring by Means of Optical Fibres and Strain Gages". In: *Smart Intelligent Aircraft Structures (SARISTU)*. Ed. by P. C. Wölcken and M. Papadopoulos. Springer International Publishing, 2016, pp. 433–469. isbn: 978-3-319-22413-8.

4

Monitoring of a Cantilever Beam

All rising to a great place is by a winding stair.

Francis Bacon

This chapter covers the initial steps towards validating the feasibility of the proposed multimodal fibre optic sensing method. The study points towards addressing Research Question 1 that falls under Complexity Level I and is focussed on 1 dimensional beam bending. The aim of this work is to be able to simultaneously estimate the deflection magnitude and position of a point arbitrary load on a cantilever beam. By using two fibre Bragg grating sensors bonded on the beam, the shape of the beam before and after deflections are estimated. Analytical modelling is used to validate and compare the experimental measurements. The results show a good approximation to the actual values and the sources of errors are identified and discussed. This chapter lays the foundation to investigate a higher complexity multi-axis case.

Parts of this chapter have been published in SPIE Smart Structures + NDE 10970, 109701Z (2019) [1].

4.1. Introduction

This chapter aims to address RQ1 which is the first step towards the design, development and justification of the novel sensing method. As the final aim is to deal with aircraft wing and wing sections, the route of using cantilevers as the test specimens is taken. This approach has also been seen in past research works for the reason that aircraft wing or wing section could roughly be considered as a cantilever structure [2–4]. This chapter deals with CL I (refer to Section 3.4) to demonstrate the feasibility of the proposed method by using a cantilever beam.

4.2. Cantilever Beam - 1D sensing

The geometry and coordinate system of the setup used for this test is as shown in Figure 4.1 along with the nomenclature used. The test specimen is a beam of length L, width w, and thickness t. The length of the beam is along the x-axis. The root and tip of the beam are denoted by x_root and x_tip, respectively. The deflection happens in the negative y-axis which varies along L depending on the load. $S1$ and $S2$ are FBGs at each end of the beam. The distance between $S1$ and $S2$ is the effective sensor length and is denoted as L_sensor. There is no load in the z-axis; the beam is considered to undergo pure bending. That the beam undergoing pure bending in the negative y-axis indicates that the upper surface undergoes tension whereas the lower surface undergoes compression. The central axis of the beam, corresponding to the neutral axis, undergoes no change in length.

Cantilever beams are also subjected to transverse shear forces. This is considered only when the thickness of the beam is comparable to the width the beam. Shear deformation effects do not play a role as long as the ratio of the width of the beam to its thickness is greater than 10 [5]. The geometric properties of the beam are as shown in Table 4.1.

Table 4.1: Material and geometric properties of the cantilever beam.

Property	Variable	Value
Material		Aluminium
Length	L	1050 mm
Width	w	25 mm
Thickness	t	1.5 mm

When a load acts on the beam, the beam is deflected by a value of δ (mm) in the negative y direction. The strain at any point x along the length of the beam L can be expressed in terms of the deflection using [6]:

$$\varepsilon(x) = \frac{3t\delta x}{2L^3}, \tag{4.1}$$

where x is any point along the length of the beam measured from x_root.

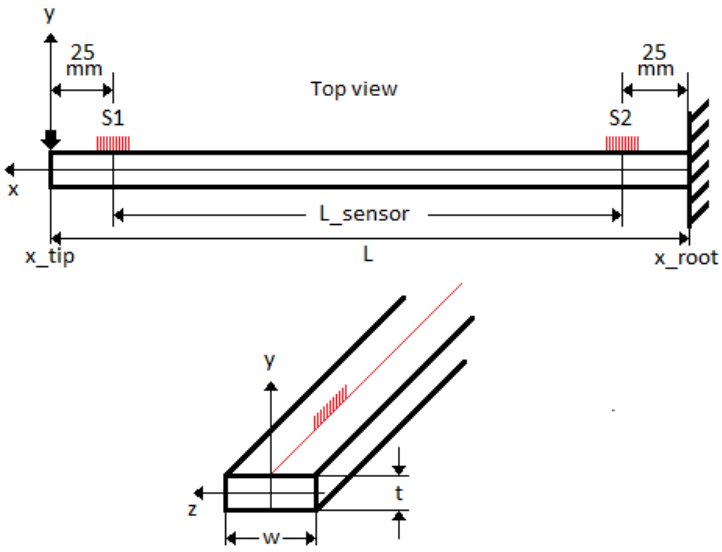

Figure 4.1: Geometry and coordinate system of the cantilever beam setup. $S1$ and $S2$ are FBGs close to the root and tip of the beam, respectively. The fibre containing the FBGs was placed along the central axis as shown in the bottom figure in red.

Furthermore, the displacement ΔL along the beam due to a deflection δ is calculated by integrating equation 4.1 along the length of the beam.

4.2.1. Setup

The beam was firmly clamped on one end with a sharp transition from clamp to beam and left free at the other to form a cantilever. Moreover, the beam was tilted by 90° such that thickness-face of the beam pointed towards the optical table. The beam was hence vertical as opposed to a typical cantilever beam setup. The vertical orientation was chosen for ease of applying deflections. This also helped in reducing vibrations as the beam bending axis was perpendicular to gravity. This configuration can be better understood by viewing Figure 4.2.

A single mode (SM) standard optical fibre was bonded to one of the faces of the beam along its length using a cyanoacrylate adhesive (3M ScotchWeld).

The bonding process was as follows. The area to be bonded was first sanded in multiple direction using sandpaper. The area was then cleaned with alcohol followed by drying the surface with a cloth. The sensing fibre was aligned to a pre-marked route on the surface and held in place with the help of tape. This was also to ensure full contact with the surface. The adhesive was applied at specific intervals along the fibre and was evenly spread using Teflon paper. The tapes were removed and

replaced with the adhesive. Finally, Teflon paper was placed along the bonded fibre till the adhesive dried.

The bond side was chosen such that the fibre would undergo tension when a positive deflection was applied. Two gratings, denoted as Sensor 1 ($S1$) and Sensor 2 ($S2$), were inscribed in the fibre. Their positions on the fibre were chosen such that $S1$ and $S2$ were 25 mm each from the ends x_tip and x_root, respectively.

The properties of the gratings were chosen in accordance with the specification and capability of the interrogators. The details of the properties of the grating sensors $S1$ and $S2$ are listed in Table 4.2 and are provided by the manufacturer (DK Photonics). Both the gratings were 3 mm in length and had a reflectively level of greater than 80%.

Table 4.2: Properties of the grating sensors $S1$ and $S2$.

Property	S1	S2
Wavelength	1530.182 nm	1539.903 nm
Bandwidth	>0.75 nm	
Reflectivity	>80%	
Temp. sensitivity	10 pm/°C	

Figure 4.2 shows the entire setup of the experiment. The beam with the optical fibre was clamped to form a vertical cantilever. A linear stage actuator (Zaber NA23C60-T4) and stage controller were used for the deflection. The deflection point of contact was through a circular cross section end effector of radius 5 mm. The location of deflection is modified using a slider stage on which the actuator is fixed. The actuator has a movement range of up to 60 mm. The local strain measurements at the two sensor locations were measured using an FBG interrogator (National Instruments, PXIe-4844) whilst the displacement between them was measured by an FBG-Pair interferometric interrogator (Optics11, ZonaSens).

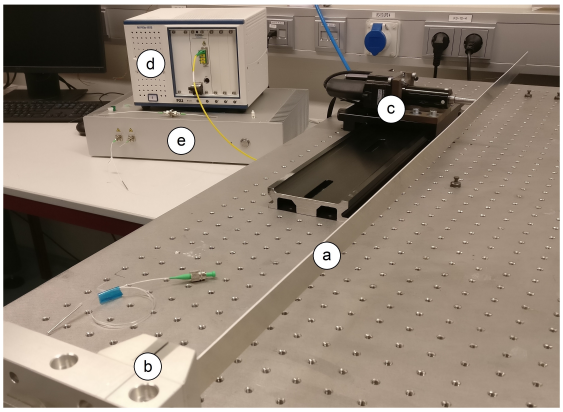

Figure 4.2: The experimental setup showing the a) Beam vertically fixed to a b) Clamp on one end to form a cantilever. The c) Linear stage provided deflections on the beam whilst the d) National Instruments interrogator and e) Optics11 interrogator measured the readings from the grating sensors $S1$ and $S2$.

4.3. Measurements

The measurement campaign involved calibration of the setup to record baseline measurements followed by measurements at arbitrary locations with arbitrary displacements.

For the calibration measurements, the linear actuator provided deflections along the x-axis with steps of 4 mm to a maximum deflection of 20 mm. On the other hand, the arbitrary measurement values were chosen by randomly sliding the actuator on the slider stage for each specific location and by using a random number generator for the displacement. The data recorded by the interrogators was used to estimate the position of the load and the subsequent magnitude of displacement of the beam.

4.3.1. Calibration

Two locations on the beam were selected to conduct the calibration tests. The calibration hence consisted of two sets of measurements one carried out at the tip of the beam and one at the mid point of the beam. The aim of these steps was also to verify the readings by comparing them with the analytical solutions for beam bending. The calibration measurements are used at a later stage for finding the location and magnitude of unknown deflections.

Using the slider stage, the linear actuator was set to apply deflections at x = 1050 mm. In 4 mm steps the beam was deflected up to 20 mm. The experimental values for the displacement ΔL and strain ε are as shown in Table 4.3 and Table 4.4, respectively. The second step was carried out following the same procedure with

the deflection now applied at the mid of the beam at x = 525 mm. The experimental values for the second case for the local strain ε are as shown in Table 4.5 and Table 4.6, respectively. The analytical results are used to compare the measurements for both cases. A systematic difference was noticed in both the cases which is discussed in Section 4.5. The loading point had a 5 mm radius area of contact. Through the slider stage, the actuator was set so that the marker on the beam was at the middle of the end effector and this had a position accuracy of $\pm$5 mm.

Table 4.3: Comparison between the analytical modelling and experimental measurements for ΔL due to δ applied at the tip of the beam.

δ (mm)	Anl. ΔL (μm)	Exp. ΔL (μm)	Difference (μm)
0	0	0	0
4	4.28	5.1	0.82
8	8.57	10.3	1.73
12	12.8	15.6	2.8
16	17.1	21.3	4.2
20	21.4	26.8	5.4

Table 4.4: Comparison between the analytical modelling and experimental measurements for ΔL due to δ applied at the midpoint of the beam.

δ (mm)	Anl. ΔL (μm)	Exp. ΔL (μm)	Difference (μm)
0	0	0	0
4	8.57	9.7	1.13
8	17.1	19.8	2.7
12	25.7	30.2	4.5
16	34.2	40.7	6.5
20	42.8	50.1	7.3

Table 4.5: Comparison between the analytical modelling and experimental measurements for ε due to δ applied at the tip of the beam.

δ (mm)	Anl. ε (μ)	Exp. ε (μ)	Difference (μ)
0	0	0	0
4	8.16	7.49	0.67
8	16.32	14.15	2.17
12	24.4	21.4	3
16	32.65	28.29	4.36
20	40.81	34.96	5.85

Table 4.6: Comparison between the analytical modelling and experimental measurements for ε due to δ applied at the midpoint of the beam.

δ (mm)	Anl. ε (μ)	Exp. ε (μ)	Difference (μ)
0	0	0	0
4	32.65	30.8	1.85
8	65.30	55.76	9.54
12	97.95	82.39	15.56
16	130.61	108.2	22.41
20	163.26	135.6	27.66

4.3.2. Unknown deflection at an unknown position

Using the data from the fibre optic sensors through the calibration measurement the aim was to determine the position of an unknown deflection. Since the grating sensor $S1$ was at the free end of the cantilever, its measurements were not included in the calculation. This was due to no change in Bragg wavelength as a result of no resistance to undergo strain at the tip of the beam in a cantilever configuration. Therefore, only grating sensor $S2$ local strain measurements were utilised.

The local strain measurement (ε) and the displacement between the two sensors (ΔL) were recorded for tip and mid deflections and are shown in Tables 4.7 and 4.8, respectively.

Table 4.7: Local strain (ε) and displacement (ΔL) measured between the grating sensors for deflections applied at the tip of the beam.

Tip δ (mm)	ΔL (μm)	ε (μ)
0	0	0
4	5.1	7.49
8	10.3	14.15
12	15.6	21.4
16	21.3	28.29
20	26.8	34.96

To demonstrate the feasibility of the estimation, the slider stage was moved to an unknown position and an unknown deflection was applied to the beam following the procedure mentioned in the beginning of Section 4.3. This was later checked to be a deflection magnitude of 8 mm (through the actuator) and at an approximate length of 974 mm (through the slider stage) on the beam.

Assuming x_1, x_2 and y_1 and y_2 are the ε and ΔL measurements for the first and second calibration steps, respectively, an iteration cycle can be used to estimate values x and y using the equation:

Table 4.8: Local strain (ε) and displacement (ΔL) measured between the grating sensors for deflections applied at the mid of the beam.

Mid δ (mm)	ΔL (μm)	ε (μ)
0	0	0
4	9.7	30.8
8	19.8	55.76
12	30.2	82.39
16	40.7	108.2
20	50.1	135.6

$$x = \frac{y - y_1}{y_2 - y_1}(x_2 - x_1) + x_1 \tag{4.2}$$

When the values of x and y values converge, the unknowns pertaining to the position and magnitude of deflection can be estimated.

For the test, the unknown position and an unknown deflection gave a ΔL value = 12.1 μm and a ε value = 20.8 μ. Using these values, the algorithm estimates the position and magnitude. The procedure for this is explained in the following section along with the results.

4.4. Results

Measurements on two known locations on the beam were recorded that served as baseline measurements. These were used as references during the final estimation. When an arbitrary load is applied on an unknown location, the loading point and deflection were estimated using a simple iterative calculation.

Table 4.9 lists the iterative steps to arrive at the earlier mentioned convergence point. To understand better the estimated length selection for each step, Figure 4.3 shows the x (mm) position that can be tallied with the x (mm) values from Table 4.9. The bars in Figure 4.3 are just pointers referring to which point on the beam was being measured. It basically visualises the first column from Table 4.9.

Table 4.9: Simultaneous estimation of unknown deflection (δ mm) at an unknown position (x mm) by the convergence of δ values from ΔL and ε.

x (mm)	δ (mm) through ΔL	δ (mm) through ε	Convergence Indicator
1050	9.358	11.67	2.312 ✗
525	4.95	2.7	2.25 ✗
787.5	6.44	4.42	2.02 ✗
918.75	7.63	6.66	0.97 ~
853.12	6.98	5.94	1.04 ✗
984.37	8.41	8.64	0.23 ~
885.94	7.29	5.94	1.35 ✗
951.56	8.00	7.54	0.46 ~
967.97	8.13	8.06	0.07 ✓

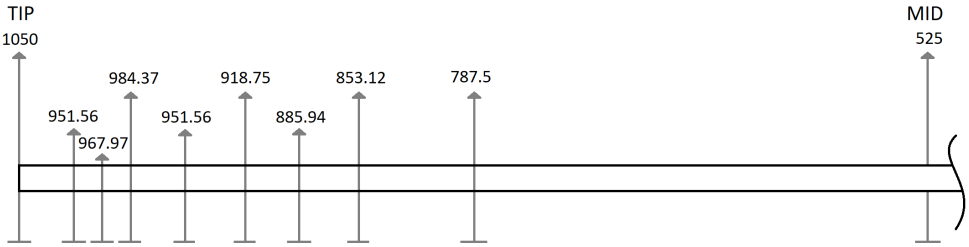

Figure 4.3: Location of the x (mm) values along the length of the beam used by the interpolation steps in Table 4.9.

4.5. Discussion

It is evident from Tables 4.3 to 4.6 that the error between the analytical and experimental values increases with the magnitude of deflection. The results though follow a linear and increasing trend. The possible sources of error that may cause this mismatch were identified.

In the analytical measurements using the strain equation (Equation 4.1), the variables h, x and L influence the slope of the line. On the other hand, in the experimental measurements the length is determined by the length between the two grating sensors. As the experimental measurements only consider the variable L, the varying slopes are attributed to the inaccuracies in length. The effective sensor length (L_sensor) had an approximate length of 1000 mm running along the centre line of the x-z plane. An average clearance of 25 mm was given on both ends of the beam as the optical fibre was not able to be bonded very close to the clamp or the beam end. This was also done to allow some space for clamping

and for the fibre not to reach to the end which might cause the fibre to break. The analytical model on the other hand posed no such issues and considered the whole 1050 mm length measured between the ends x_root and x_tip. It is to be noted that even if the analytical length was taken as 1000 mm, the measurement inequality would still be present. This on the other hand was not an issue as the analytical values were just a reference and not used in the final calculation. The experimental values reflect the actual FBG response to the beam bending taking into account the length uncertainties mentioned above. This also shows the importance of the calibration step.

Another source of length inaccuracy was attributed to the location of the gratings themselves. The location of the grating is typically marked by the manufacturer as a range where the grating could be present anywhere in between. This added to the uncertainty which in turn can increase the mismatch in the estimated results. It is impossible to spot the gratings with the naked eye. This would require striping the cladding layer of fibre to expose the core and viewing the marked region under a microscope.

Despite these errors and not accounting for them in the final estimation, the preliminary calculations yielded a good estimate of the position and magnitude of the unknown deflection. From the experiments (refer to Table 4.9), the magnitude of deflection had an accuracy of $\pm$0.07mm whilst the deflection position showed an accuracy of $\pm$6 mm along a length of 1000 mm.

To check the robustness of the system and the repeatability of the measurements, a series of 'extreme' tests were carried out which were not part of the main experimental campaign. The extreme tests involved repeated bending of the beam to deflections more than twice the maximum deflection planned for the final tests. This was also to ensure that the optical fibre was bonded properly to the beam.

In the first step, the translation stage was used to deflect the beam at different magnitudes and at predefined locations along the beam and the measurements were recorded as reference data. The second step involved repeated extreme bending, a trial of which is as shown in Figure 4.4 and in Table 4.10. Multiple iterations of these two steps were carried out and the reference data was compared after every iteration.

An interesting observation was made regarding the systematic errors in the measurement. The experimental values for ΔL were higher than the analytical values but those of ε were lower than the analytical values instead. For ε this decrease in strain is due to the grating present away from the root. The more further away the grating from the root, the lower the strain acts on it. On the other hand, the ΔL measurement faced a unique issue. The displacement ΔL is calculated between the two grating pairs. This essentially means that if the grating part of the fibre was left unbonded whilst the fibre region in between these gratings alone was bonded, this would suffice. The strain output is increased when one or both the gratings are bonded to the beam. A recommendation to overcome this would be to only bond the region between the gratings which would give more accurate results. But, a

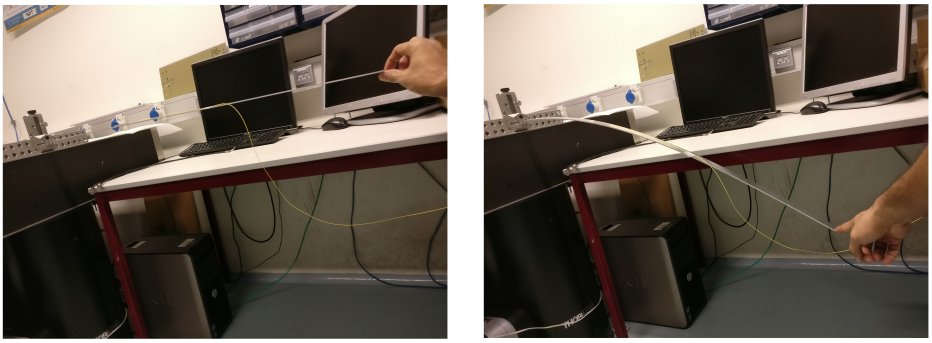

(a) (b)

Figure 4.4: Extreme deflection tests on the cantilever beam with the bonded optical fibre to check for repeatability and robustness. a) Undeflected and b) Deflected beam

Table 4.10: Iteration sample of an 'extreme test' at 40 mm deflection focussed on repeatability.

Tip δ (mm)	ΔL (μm)	ε (μ)
40	53.72	70.09
40	53.68	70.09
40	53.68	70.10
40	53.69	70.10
40	53.69	70.09
40	53.71	70.10

big drawback would be that the local strain measurements would not be able to be calculated as for this the FBGs do need to bonded. Hence, it is preferred to bond the the grating regions too.

4.6. Concluding remarks

This first technical chapter is of complexity level I and presents the feasibility study and demonstration of the multimodal fibre optic sensing approach on beams. A preliminary study was carried out followed by a thorough experimental campaign on a cantilever beam. Analytical modelling of the beam was used to compare the measurements acquired from the tests. The aim of this work was to demonstrate 1 dimensional sensing by estimating the position and magnitude of an arbitrary load on the beam. Two grating sensors were used through which local strain measurements as well as the displacement information between them

is captured.

This study showed that when the starting shape of the beam is known, it can be used as a reference to estimate its final shape based on the deflections taking place. Hence, the multimodal approach demonstrates a novel way of sensing the shape of the beam due to arbitrary loads applied on it. The calculation is based on an iterative process to estimate the unknowns. The results yielded a good approximation with an accuracy of $\pm$0.07mm and $\pm$6 mm for deflection magnitude and position estimation, respectively. The possible error sources were identified and discussed. This approach is independent of the material properties of the beam and hence can be used with beams of different materials and lengths provided they exhibit elastic behaviour. The geometry can also be varied provided the ratio between the width to the thickness remains below 10. To be able to use beams with varying geometry and material, it is important to have an initial calibration step for baseline measurements. With the series of extreme tests, it can be concluded that the the fibre remained intact and the measurements had good repeatability. Overall this gives rise to a reliable monitoring system.

This chapter forms the basis for understanding the system and for the chapters that follow. It opens up the idea for a higher complexity problem. The following chapter discusses complexity level II that involves 2 dimensional shape sensing on a plate that includes twisting in addition to bending.

References

[1] **N. Nazeer**, R. M. Groves, and R. Benedictus. "Simultaneous Position and Displacement Sensing Using Two Fibre Bragg Grating Sensors". In: *Proc. SPIE Smart Structures + Nondestructive Evaluation* 10970 (2019), 109701Z-1 –109701Z-8. doi: 10.1117/12.2513415.

[2] W. Ko, W. L. Richards, and V. T. Tran. "Displacement Theories for In-Flight Deformed Shape Predictions of Aerospace Structures". In: *NASA/ TP-2007-214612* (Oct. 2007).

[3] Q. Zhu, C. Xu, and G. Yang. "Experimental research on damage detecting in composite materials with FBG sensors under low frequency cycling". In: *International Journal of Fatigue* 101.P1 (2017), pp. 61–66. doi: 10.1016/j.ijfatigue.2017.03.034.

[4] M. Gherlone, P. Cerracchio, and M. Mattone. "Shape sensing methods: Review and experimental comparison on a wing-shaped plate". In: *Progress in Aerospace Sciences* 99 (2018), pp. 14–26. issn: 0376-0421. doi: https://doi.org/10.1016/j.paerosci.2018.04.001. url: https://www.sciencedirect.com/science/article/pii/S037604211730221X.

[5] H. Reismann and S. Cheng. "The edge reinforced cantilever plate strip". In: *Publication International Association for Bridge and Structural Engineering* 30 (1970), p. 149.

[6] Y. Mizutani and R. M. Groves. "Multi-Functional Measurement Using a Single FBG Sensor". In: *Experimental Mechanics* 51 (Nov. 2011), pp. 1489–1498. doi: 10.1007/s11340-011-9467-2.

5

Monitoring of a Cantilever Plate

This chapter forms the basis of understanding the multimodal sensing approach on plate-like structures. The study addresses Research Question 2 that falls under Complexity Level II and is focussed on 2 dimensional plate bending. The aim of this work is to be able to estimate the position of a point arbitrary load on a cantilever plate. By using four fibre Bragg grating sensors bonded on the plate, the shape of the plate before and after the deflections are estimated. An experimental based model is used that involves an initial calibration to compare and facilitate the experimental measurements. The results show a good approximation to the actual values and the sources of errors are identified and discussed. This chapter lays the foundation to investigate a higher complexity case involving bending, torsion and their combinations.

Parts of this chapter have been published in SN Applied Sciences 3, 667 (2021) [1].

5.1. Introduction

This chapter aims to address RQ2 which is a development over the previous cantilever beam study. This chapter aims at multi-axis monitoring and also focusses on the estimation of the location of an arbitrary point load on the surface of a cantilever plate. The methodology in this study is similar to the previous beam case where fibre Bragg grating sensors were used to measure local strain measurements as well as the displacement between any two sensors. Using the proposed hybrid sensing principle, the position and magnitude of an applied load on the surface of the plate is estimated. This chapter falls under the Complexity Level II category where the bending and torsion of a cantilever plate are studied.

For engineering structures, having information of the loads acting on them is vital for monitoring their health over their service life. This also includes point loads, especially for those structures that can be deflected and undergo bending and twisting according to their design specification. These mostly include cantilever structures like aircraft wings, rotor blades and masts. Apart from the magnitude of load on the structure, knowing the location of the load can give additional insight on the response of the structure and its capability to withstand these loads. With this information, occurrences of anomalous structural behaviours can be detected with the option of making design changes if required.

Some notable works like that of Jaramillo [2] and Reismann and Cheng [3] have analysed the bending of an infinitely long cantilever plate with concentrated loading. These formulations are difficult to understand, have several limitations including limited deflection cases and are known to be computationally difficult for general use [4].

The majority of the explicit analytical models for (rectangular) plates exit predominantly for simply-supported boundary condition cases, a list of which can be found in [5]. Moreover, for a rectangular cantilever, uniform loading is always presented, citing convenience. The case of an arbitrary point loading followed by the measurement of deflection along x and y axes is more complex and often has to deal with approximations in the model [5–8]. Moreover, the loading points are not arbitrary but predefined; They are 'edge loaded', 'load at the centre line' or 'load at the (free) edges'. For plates with thicknesses comparable to the width, shear was the predominant failure mode during bending. In our applications, the thickness of the structure is very small compared to the width (and length). Hence, shear does not play a role [3], as mentioned in Chapter 4.

A common approach is to resort to general purpose numerical models like finite element methods (FEM) is quite common. When it comes to complex structures, it may become difficult to accurately model the behaviour using traditional FEM methods. For example, it is simple to model the behaviour of a flawless flat plate. But, if a real world rectangular plate has inbuilt stresses and uneven curvature due to the cutting process, installation and clamping, it is increasingly difficult to represent these accurately.

Therefore, 'approximations' are used, as seen in previous works to replicate the structure. An alternative, which is adopted in this study, is to have an experimental

based model. In this way the exact response of the structure can be captured regardless of the presence of unknown irregularities.

The following assumptions are in place for the monitoring of the cantilever plate in this study.

- The loads on the plate do not result in shear (Kirchhoff hypothesis).
- The mid-plane of the plate remains un-deformed.
- The plate undergoes bending and torsion within a predefined range.

5.2. Cantilever Plate - 2D sensing

The geometry and coordinate system of the setup used for this test is as shown in Figure 5.1 along with the nomenclature used. The test specimen is an aluminium plate of length l, width w, and thickness t. The root and tip of the plate are denoted further on as root and tip, respectively. Deflection is in the z-axis and varies along l depending on the load/deflection.

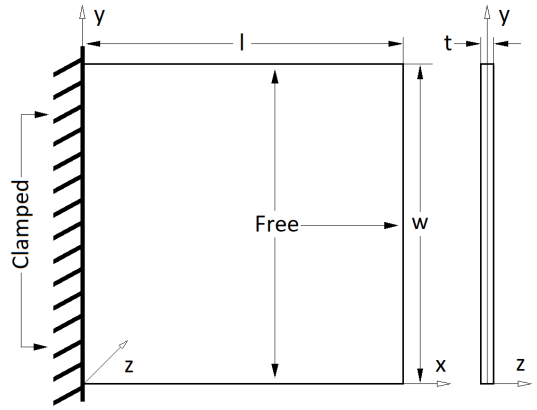

Figure 5.1: Geometry and coordinate system of the cantilever plate setup.

There is no load or deflection acting in the y-axis. The plate is undergoing bending in the negative $\pm$z-axis indicating that the upper surface undergoes tension whereas the lower surface undergoes compression. The central axis of the plate, corresponding to the neutral axis, undergoes no change in length (refer to assumptions; Section 5.1). The geometric properties of the plate are as shown in Table 5.1. The dimensions of the plate were chosen to have a better understanding of realistic sized structures. This was also done as the findings from this study would go on to develop the sensing approach for morphing wing sections of similar dimensions (Chapter 6).

Table 5.1: Material and geometric properties of the cantilever beam.

Property	Variable	Value
Material		Aluminium
Length	l	1000 mm
Width	w	1000 mm
Thickness	t	2 mm

5.2.1. Setup

The experimental setup is as shown in Figure 5.2. The plate was firmly clamped on one end and left free at the opposite side to form a cantilever configuration. For practical reasons as well as for ease of applying deflection, the plate was clamped vertically like a flag as opposed to a typical cantilever configuration. This was also done to minimize the gravitational loads acting on the the x-y plane.

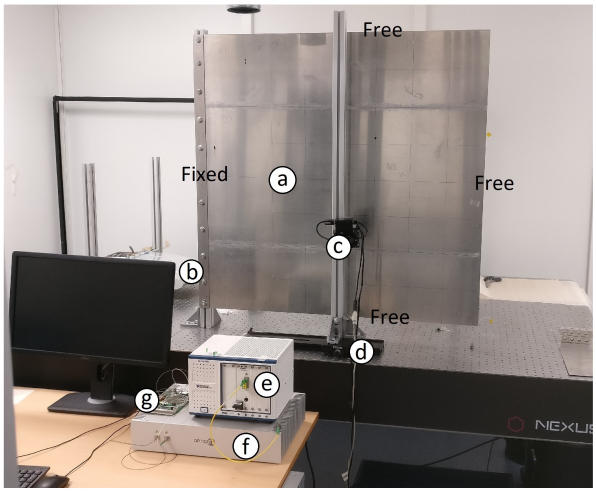

Figure 5.2: The experimental setup showing the a) Plate vertically fixed/clamped to a b) Support beam on one end. The c) Linear stage is attached to a d) Slider stage. The e) National Instruments interrogator, f) Optics11 interrogator and g) Optical switch are also shown.

The clamped side of the plate was bolted to an aluminium support beam (Boikon) of length l = 1100 mm, breadth b = 40 mm, and thickness t = 40 mm. The beam was attached and secured firmly to the optical table.

A linear stage actuator (Zaber NA23C60-T4) and stage controller, see Figure 5.3, deflected the plate at different points in the z-direction and had a travel range of up to 60 mm. The location of the loading points were accessed through slider

stages. The loading point of contact was a flat circular-cross-section surface of radius 5 mm. The local strain measurements were measured using an FBG interrogator (National Instruments, PXIe-4844) whilst the displacement between them was measured by an FBG-Pair interferometric interrogator (Optics11, ZonaSens). Both the interrogators have a tunable wavelength-swept laser and a class 1M laser. As each of the interrogators had their own light sources, an optical switch (Thorlabs, OSW22-1310E) was used to either select a particular interrogator or to switch between the two.

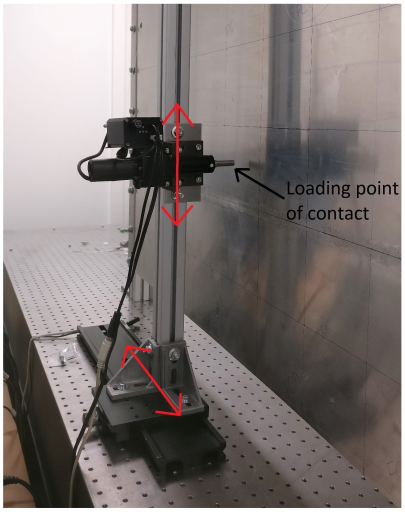

Figure 5.3: The linear actuator and loading setup showing the vertical and horizontal slider stage mechanism.

To interrogate the plate, a standard single mode (SM) SMF-28e (Corning) optical fibre was bonded to the plate that contained 4 fibre Bragg grating sensors inscribed in its core. The sensors are referred to as $S1$, $S2$, $S3$ and $S4$. The fibre layout, sensors and sensor properties are described in Section 5.2.2.

A schematic of the entire setup for monitoring of the plate is as shown in Figure 5.4. The fibre bonded to the plate is termed as the 'sensing fibre'. The zoomed in view of it shows the presence of the grating sensors as reflectors. The length between $S1$-$S4$ and $S2$-$S3$ pairs is the effective sensing length denoted as L_{sensor}.

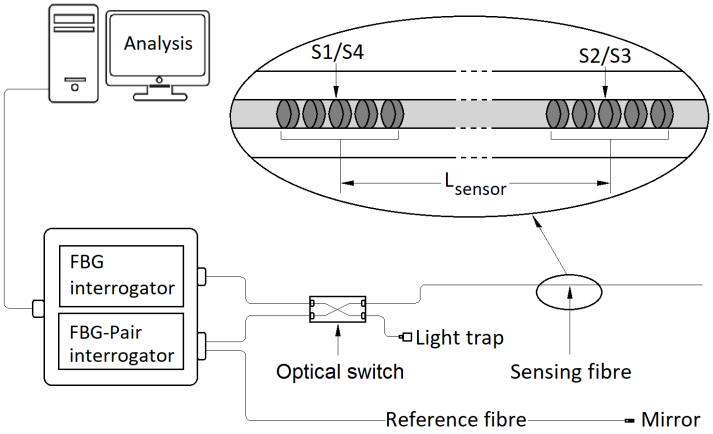

Figure 5.4: Schematic of the experimental setup including the sensing and reference fibre. Zoomed in: Structure of the sensing fibre containing the $S1/S2$ and $S4/S3$ grating sensor pairs.

5.2.2. Sensor design

The layout of the fibre and the positioning of the sensors was adopted from the study in Chapter 4. It also follows the location optimisation performed by Jones et al. [9] and Ko et al. [10] on similar cantilever structure studies. Figure 5.5 shows the layout of the fibres and the position of the sensors with respect to the plate edges. The fibre was laid out along the length (x-axis) of the plate and followed a U-shaped pattern. The straight lines of the U contain the sensors and hence the fibre (and the gratings) were perpendicular to the y-axis. They are 250 mm each from the central axis of the plate measured in the $\pm$y direction. This distance was chosen to be able to cover the entire plate so as to capture movements in multiple directions. These two fibre regions were bonded to the plate using a cyanoacrylate adhesive (3M Scotch-Weld). The curved part of the U did not contain any sensors and did not contribute (nor hinder) the measurements. This curved region was left unbonded and was just taped to the plate to avoid breakage and to look neat. Taping the fibre in that region did not have negative effects on the measurements. Sensors $S1$ and $S4$ were closer to the root of the plate whilst $S2$ and $S3$ were at the free end.

Sensor pairs $S1$ and $S4$ and $S2$ and $S3$ measure the normal strains acting in the clamped-free direction. They are positioned at approximately x = 50 mm and x = 950 mm from the root, respectively. These locations were chosen to stay away from the corners (especially the clamp side) as the fibre had to be curved in order to avoid breakage.

As also shown in Figure 5.4, the length between the adjacent sensors $S1$-$S2$ and $S3$-$S4$ forms the effective sensing zone (L_{sensor}) of the fibre. This effective zone

measured approximately 900 mm for each of the sensors pair. It is noteworthy to mention that the interrogation can also be done for even longer L_{sensor} values.

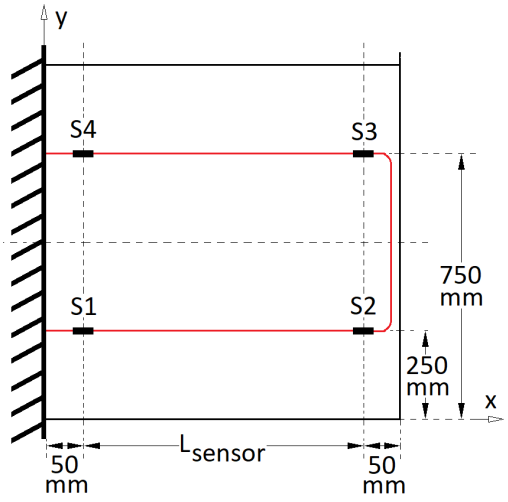

Figure 5.5: Layout of the fibre (in red) and the grating sensors. $S1$-$S2$ and $S3$-$S4$ are parallel and equidistant to the central axis of the plate and are along the clamped-free direction.

Measurement of the axial displacement between sensors $S1$ and $S2$ is denoted by ΔL_{1-2} and that between sensors $S3$ and $S4$ is denoted by ΔL_{3-4}. For the local strain measurements of each sensor, they are denoted corresponding to their individual sensor numbers subscripted (refer to Figure 5.5) as ε_1, ε_2 , ε_3 and ε_4.

The properties of the grating sensors $S(1-4)$ are listed in Table 5.2 and are as specified by the manufacturer (DK Photonics). Certain properties like the wavelength and reflectivity of the gratings were selectively chosen so as to accommodate the working of both the interrogators. The wavelength of the gratings were between 1530 nm and 1560 nm as the interrogators functioned better within the C-band range. The C-band is generally preferred due to low attenuation of the optical fibre. All the gratings had a temperature sensitivity of 10 pm/°C.

Table 5.2: Properties of the grating sensors S1, S2, S3 and S4 (DK Photonics).

Property	S1	S2	S3	S4
Wavelength	1530.182 nm	1539.903 nm	1549.955 nm	1560.118 nm
Bandwidth	0.785 nm	0.762 nm	0.785 nm	0.782 nm
Reflectivity	98.27%	98.12%	98.32%	97.42%
Temp. sensitivity	← 10 pm/°C →			

5.3. Measurements

The measurement campaign involved two main steps. The first step was the calibration of the setup and the recording of baseline measurements in order to develop an experimental based model. The second step involved measurements at arbitrary locations on the plate with arbitrary magnitudes. This step was done with two different calibration data to understand the calibration data dependency. The data recorded by the interrogators was used to estimate the position of the load and the subsequent magnitude of displacement of the plate. The linear actuator provided deflections along the z-axis with a range of 0 to 60 mm.

5.3.1. Calibration

The first step of the calibration procedure was to select calibration points. The plate was initially divided into a 8 x 8 grid as shown in Figure 5.6. Each grid was a square of 125 x 125 mm. The interest lied in the bending and torsion behaviour of the plate and the ability of the sensing method to estimate the position and magnitude of arbitrary loads. Within the elastic stress range, deflections within the x = 0 mm to 500 mm range caused the plate to undergo complex bending due to distributed stress concentrations that was out of the focus of this study. The area of interest was therefore the region within x = 500 mm to 1000 mm that are in the free half of the plate. Therefore, only the tip half of the plate was analysed as the maximum plate tip-deflection would be easily achieved with loads at the tip end. A 4 x 8 grid (with 45 calibration points) was considered and forms the highlighted part of the grid in Figure 5.6. These 45 points are the calibration measurement points and will be referred to as the 'finer grid'. Deflections were applied in steps of 5 mm up to a maximum of 25 mm (0, 5, 10, 15, 20 and 25 mm). This deflection range was chosen as the mock up wing (Chapter 6) and the SmartX wing (Chapter 7) were estimated to have similar ranges of deflection.

In addition to this, a second grid pattern was selected consisting of a 3 x 3 grid pattern for the same plate as shown in Figure 5.7. This is further referred to as the 'coarser grid'. The 3 x 3 pattern was chosen to understand the dependency of calibration-point number, location and grid density. A detailed study on the 'ideal grid spacing' would require a series of grid size convergence studies that is not the focus of this investigation.

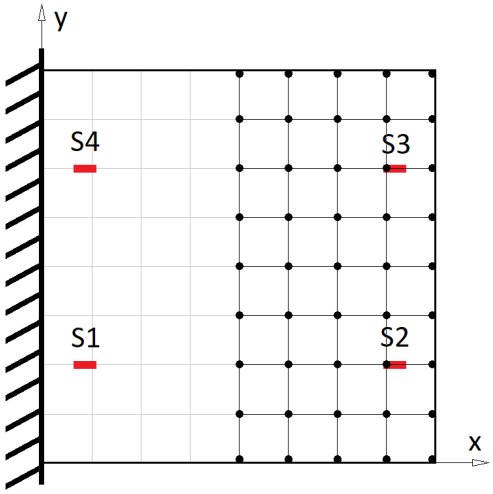

Figure 5.6: The highlighted pattern showing the area of interest and the 45 calibration points of the finer grid. The grid pattern is formed of 125 x 125 mm squares. The position of the sensors are also shown.

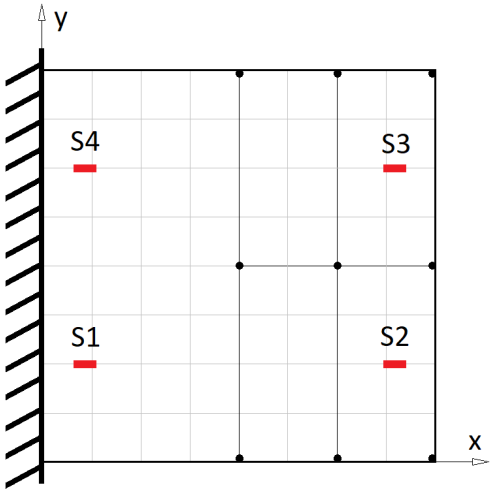

Figure 5.7: The highlighted pattern showing the area of interest and the 9 calibration points of the coarser grid. The grid pattern is formed of 250 x 500 mm rectangles. The position of the sensors are also shown.

5.3.2. Deflection at arbitrary locations

This measurement section is the most important part of the study where deflections are applied at arbitrary locations. This is to have a deeper understanding of plate deflections due to loads at unknown positions and with unknown magnitudes.

To a first approximation, the plate can be considered as two wide cantilever beams side by side each having an optical fibre. Each of these fibres are ± 250 mm from the central axis of the plate. As a first guess, for loads applied at the central axis line of the plate, the plate would undergo pure bending. This would result in the measurements from each of the sensors from either fibres to read the same. In other words, ΔL_{1-2}, ε_1 and ε_2 should measure the same as ΔL_{3-4}, ε_4 and ε_3, respectively.

Test 1 - Finer grid

Four locations on the plate were marked as A, B, C and D on the plate as shown in Figure 5.8. These were the arbitrary test points where deflections of 5 mm steps from 0 mm to 25 mm were applied. Furthermore, six trials were conducted for each deflection step to check the repeatability of the measurements. This means that for each deflection step the plate was loaded and un-loaded six times. The loading point of contact (see Figure 5.3) position accuracy was estimated to be within 2 mm error. The displacements between the sensors (ΔL) and the local strain measurements (ε) were recorded.

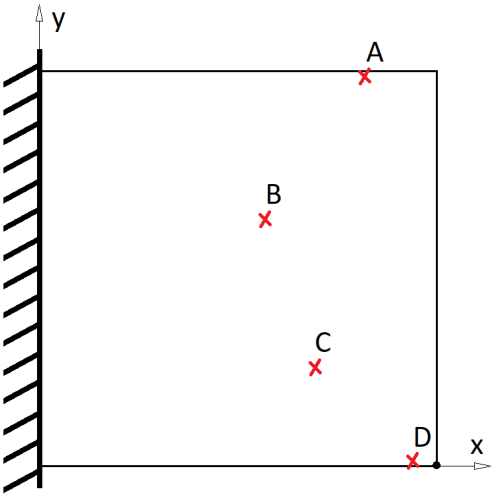

Figure 5.8: Location of the arbitrary test points A, B, C and D on the plate.

Test 2 - Coarser grid

Following the same steps of the finer grid (Section 5.3.2) measurement procedure, deflections were applied at the arbitrary points A, B, C and D with 5 mm steps from 0 mm to 25 mm. The difference is that the coarser grid (Figure 5.7) was considered here for measurements of ΔL and ε. The loading point of contact position accuracy was again estimated to have an error of within 2 mm.

5.3.3. Algorithm

To recap, each of the grating sensors in the experiment provide a local point strain measurement reading denoted as ε_{1-4}. A second set of measurements are recorded which correspond to the strain between the grating sensor pairs, denoted as $\Delta L_{1/2-3/4}$. The combination of all the measurements is mapped to a particular location on the surface of the plate which is used to estimate the loading position of any arbitrary load. Hence, the algorithm deals with the prediction and estimation of the load applied on the surface of the plate using the data from sensors.

The algorithm relies on linear interpolation between predetermined and fixed reference points that are further referred to as Calibration Points (CP) . For each of these reference points, the sum of the strains is calculated for each of the sensors. A data-driven method was developed to realise this estimation. This procedure consists of four steps and is elaborated as follows.

Step 1: Calibration data are recorded for all the 45 calibration grid points as shown in Figure 5.6. These measurements would serve as baseline and reference measurements for the upcoming steps. The CP's are calculated by deflecting the plate at known locations and recording the measurements of ε_{1-4} and $\Delta L_{1/2-3/4}$.

Step 2: The plate is deflected at arbitrary unknown locations (refer to Figure 5.8). These locations would further be referred to as Test Points (TP). Similar to step 1, measurements from all the sensors are recorded for all TP's.

From step 1, ε_1, ε_2, ε_3, ε_4, ΔL_{1-2} and ΔL_{3-4} measurements are recorded for points 1 to n. Variable n refers to the CP number where n_{max} = 45. These are the reference point data. Following this from step 2 the measurements are recorded for points 1 to n for all the TP's.

Step 3: The next step involves the ratios of all the CP's with the TP's (Equations 5.1- 5.6). Each CP measurement from step 1 is divided by the TP measurement from step 2. For example, CP ΔL_{1-2} for point 1 divided by TP ΔL_{1-2} of point 1, until, CP ΔL_{1-2} for point 45 divided by TP ΔL_{1-2} of point 45, and so on. The percentages of these ratios are denoted as $k1_n$, $k2_n$, $k3_n$, $k4_n$, $k5_n$ and $k6_n$ for all ΔL_{1-2}, ΔL_{3-4}, ε_1, ε_2, ε_3 and ε_4, respectively.

$$k1_{1\to n} = \frac{CP_{1\to n}\Delta L_{1-2}}{TP_{1\to n}\Delta L_{1-2}} * 100 \tag{5.1}$$

$$k2_{1\to n} = \frac{CP_{1\to n}\Delta L_{3-4}}{TP_{1\to n}\Delta L_{3-4}} * 100 \tag{5.2}$$

$$k3_{1\to n} = \frac{CP_{1\to n}\varepsilon_1}{TP_{1\to n}\varepsilon_1} * 100 \tag{5.3}$$

$$k4_{1\to n} = \frac{CP_{1\to n}\varepsilon_2}{TP_{1\to n}\varepsilon_2} * 100 \tag{5.4}$$

$$k5_{1\to n} = \frac{CP_{1\to n}\varepsilon_3}{TP_{1\to n}\varepsilon_3} * 100 \tag{5.5}$$

$$k6_{1\to n} = \frac{CP_{1\to n}\varepsilon_4}{TP_{1\to n}\varepsilon_4} * 100 \tag{5.6}$$

Step 4: The average of the sum of the results from equations 5.1- 5.6 for points 1 to n is denoted as (capital) K and is calculated for every variable that holds $1 \leqslant n \leqslant 45$ true as:

$$K_{1\to n} = \frac{(\sum_{i=1}^{n} k1_i + \sum_{i=1}^{n} k2_i + \sum_{i=1}^{n} k3_i + \sum_{i=1}^{n} k4_i + \sum_{i=1}^{n} k5_i + \sum_{i=1}^{n} k6_i)}{6} \tag{5.7}$$

There are two possible occurrences from this formulation. Either a TP would coincide and be equal to the corresponding CP or there would be a mismatch between them.

When the TP coincides with its corresponding CP, the percentage of the values of $k(1-6)_{1\to n}$ would be equal to 100, assuming no measurement errors are present. Substituting this value again in equation 5.7 would be 600/6 = 100. This shows that in a ideal case of TP = CP, K_n is always equal 100 indicating that the loading point is exactly at the reference/calibration point 'n'.

On the other hand, when the TP does not coincide with a corresponding CP, the values of $k(1-6)_{1\to n}$ are either greater or lower than 100. In this case, for the given strain values, the TP is bound to always fall within any of the calibration grid-boxes. This also means that the closest CP's to the TP are always the four corner points of the grid-box it is within. The aim henceforth is to locate the region within the grid-box that coincides or is the closest to K_n = 100. For this, an interpolation is done between all the adjacent points and the TP. By doing so a closed region is revealed that forms the estimated location of the applied load.

Furthermore, the TP from the previous step is now a new CP for the learning algorithm and is considered as an additional point in the calibration grid. In other words, the total calibration points that was 45 is now increased by 1 and the new range for the calculation of a new TP will be $1 \leqslant n \leqslant 46$. These iterations keep increasing the value of 'n' hence increasing the CP data library. The converse of the approach is utilised to estimate the magnitude of deflection keeping it as an unknown variable. The measurement library recorded from the sensors are used to back calculate the deflection magnitude.

5.4. Results

The local strain measurements of sensor $S2$ and $S3$ corresponding to ε_2 and ε_3, respectively were negligible. This was also intuitive as the free end of a cantilever undergoes the least amount of strain and the strain at the tip tends to zero. The magnitudes of ε_2 and ε_3 were measured to be less than 5% relative to ε_1 and ε_4 for all CP measurements and were not used in the final calculation.

Table 5.3 shows the typical magnitude of acquired strains from the sensors. For this measurement, the displacement was applied at the centre of the plate, measured at x = 500 mm and y = 500 mm. To check for the repeatability, six trials were recorded for each measurement. The values for ΔL_{1-2} and ΔL_{3-4} were within the 0 to 85 microns range and within the 0 to 160 microns range for ε_1 and ε_4. The standard deviation for these measurements were 0.035, 0.038, 0.012 and 0.013 microns, respectively. This deviation had an effect of ± 1.5 on the output quantity K_n (Equation 5.7) which was considered in the algorithm step whilst estimating the location.

Table 5.3: Typical magnitudes of measured displacement for ΔL_{1-2}, ΔL_{3-4}, ε_1 and ε_4. The plate was deflected at the centre by 20 mm.

Trials	ΔL_{1-2} (μm)	ΔL_{3-4} (μm)	ε_1 (μ)	ε_4 (μ)
1	68.79	55.28	110.58	129.02
2	68.82	55.25	110.57	128.99
3	68.74	55.32	110.59	128.99
4	68.74	55.22	110.58	129.01
5	68.83	55.28	110.59	129.02
6	68.80	55.24	110.61	129.02
Mean	68.79	55.27	110.59	129
Standard deviation	0.035	0.038	0.012	0.013

5.4.1. Finer grid

The actual locations of the arbitrary test points A, B, C and D were later measured and are as shown in Table 5.4. These points were used for the estimation with both the finer and the coarser (Section 5.4.2) grid. For each of these points individual plate maps are shown for all the 5 deflection cases (5 mm to 25 mm in steps of 5). Figures 5.9 to 5.12 display the position estimation map for test points A, B, C and D, respectively, for the case of the finer grid with a 4 x 8 grid pattern (Figure 5.6).

The measured and interpolated values are depicted on the plate in the form of a coloured distribution using the colormap function in Matlab. The two extremes of the colour map, green and red, represent the closest and the furthest from the predicted location, respectively. When a TP measurement is around the '100' mark (refer to Section 5.3.3), the colour bar (unit less) is represented by the colour green

Table 5.4: Actual location of the test points A, B, C and D.

Arbitrary test point	Location x,y (mm)
A	812,995
B	562,620
C	687,255
D	937,5

or its shades on the surface of the plate. A tolerance limit of 1.5 was chosen to have a larger estimation area. This was also done to have a higher resolution for marking the predicted region. The final output were closed regions on the plate that determined the position of the applied arbitrary load to be anywhere within them.

These regions were noticed to have different shapes when the load was applied at the free-edges (A and D) and in the bulk (B and C) of the plate. The estimated region for test point A (Figure 5.9) was discontinuous and ran beyond the plate edge regardless of the magnitude of the deflection. A noticeable feature of this region was the straight line sides that curve on one end and are left open on the other. As there were no reference points to link to past the edge, the region remained open. Although the shape of the estimated region remains constant through all deflection cases (5, 10, 15, 20 and 25 mm), the size of the region starts to increase with the increase in deflection. This indicates that the prediction error is the highest for deflection at and above 20 mm. Under this load the plate is undergoing torsion. Another point of interest is the varying colour map. As the deflection magnitude increases there is a noticeable shift from red/orange to yellow/green. A similar open pattern was also noticed for point D (Figure 5.12) since the point is also located at the edge of the plate. Under this load the plate undergoes torsion in the opposite side as of that of load at point A.

Unlike test points A and D, test points B (Figure 5.10) and C (Figure 5.11) had a clear closed region as they were located in and around the centre of the plate. The closed region is possible mainly because of the presence of linking reference points on all sides of the loading point. As the deflection increases, the size of the estimated region also increased but had a greater error than that of A and D for higher deflections. There was hence a larger spread of colour shift towards the yellow/green shade.

The asterisk indicates the actual loading point. It was seen to always lie within the estimated loading region for all TP cases. The size of the estimated loading region may vary based on loading location and loading magnitude but would always remain within the size of a single calibration block (125 mm x 125 mm).

The highest error was noticed for points B and C that were both closer to the root than than the others. More specifically, the x-direction error was greater than that of the y-direction. This effect is caused primarily because of the possible internal stresses and uneven curvature near the mid region of the plate at (x,y) = (0.6 m, 0.7 m). An anomalous behaviour was also noticed that is shown through abrupt

orange/red concentrated patches. This had an effect on the measured strain and the final estimation. Overall, for TP's A to D for a 1000 mm x 1000 mm plate, the estimations were within a region of (x,y) = (57.6 $\pm$1,67.5 $\pm$1).

When a sparse calibration pattern is chosen it is most likely that multiple points are closer to the 100 mark on the colour bar. For example, if two points are the closest to the 100 mark, an interpolation is done between them to reveal that the estimated point of interest is somewhere in between these two points. The algorithm considers a linear change between the reference points and therefore does not have a smooth/curved form for the estimated region.

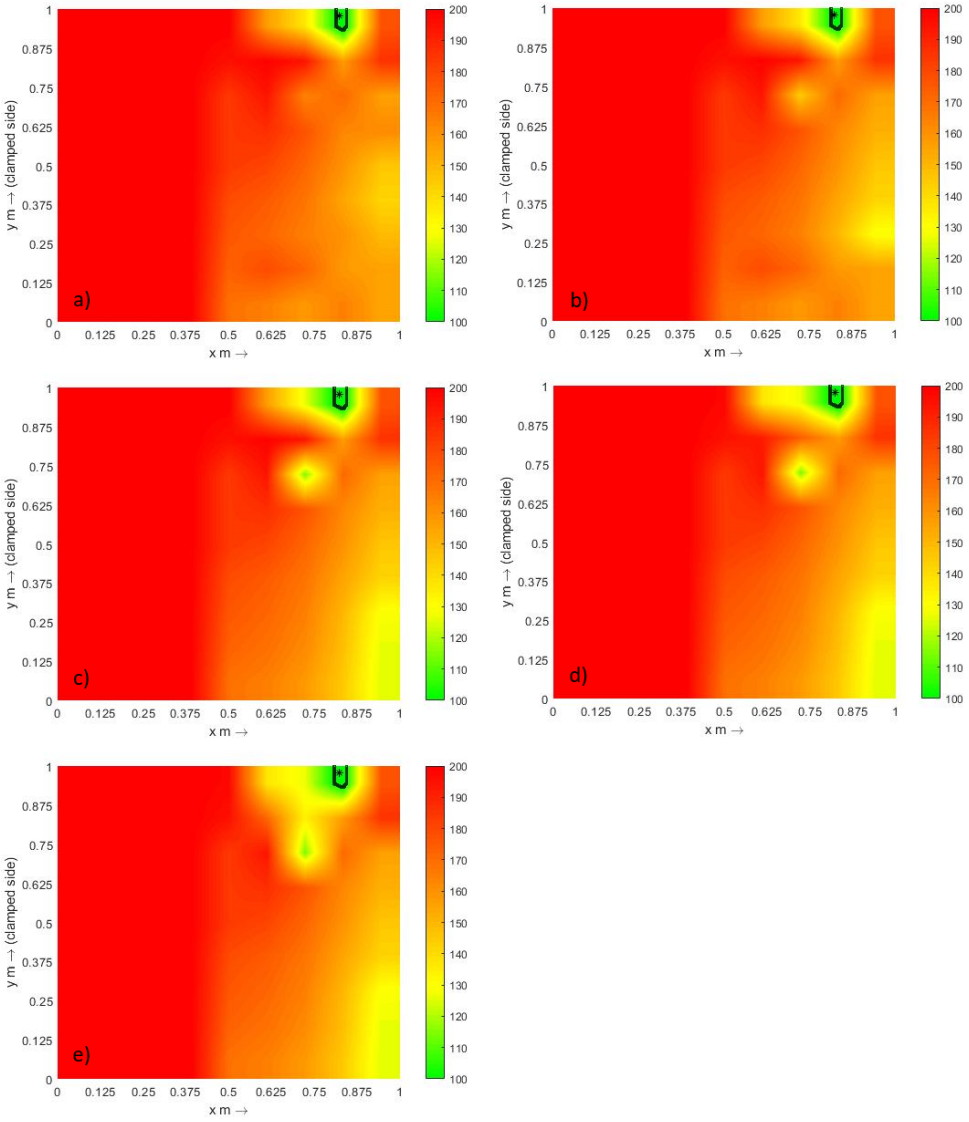

Figure 5.9: Estimated location of the applied load for arbitrary test point A using the finer grid. The actual location is marked by the asterisk. The estimation is shown for a) 5mm, b) 10 mm, c) 15 mm, d) 20 mm and e) 25 mm deflections.

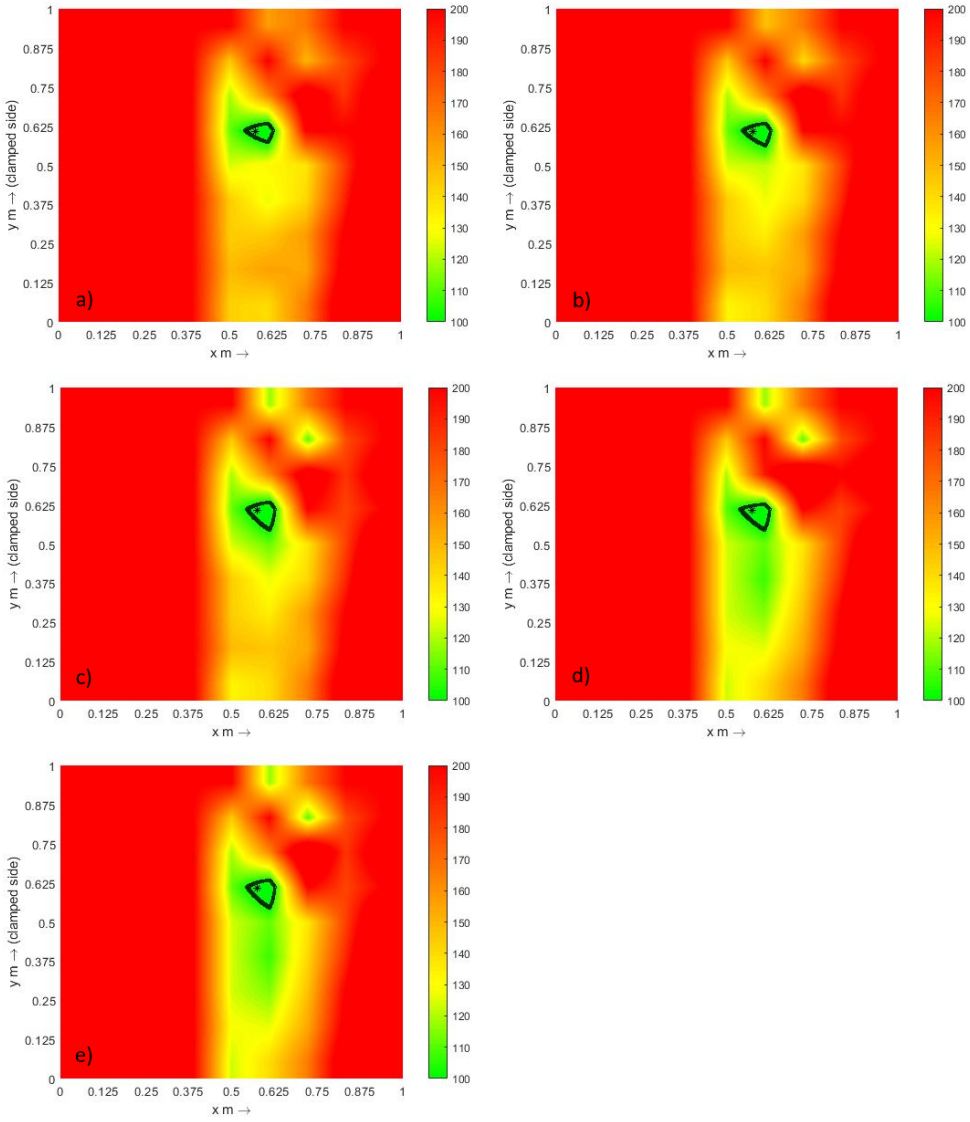

Figure 5.10: Estimated location of the applied load for arbitrary test point B using the finer grid. The actual location is marked by the asterisk. The estimation is shown for a) 5mm, b) 10 mm, c) 15 mm, d) 20 mm and e) 25 mm deflections.

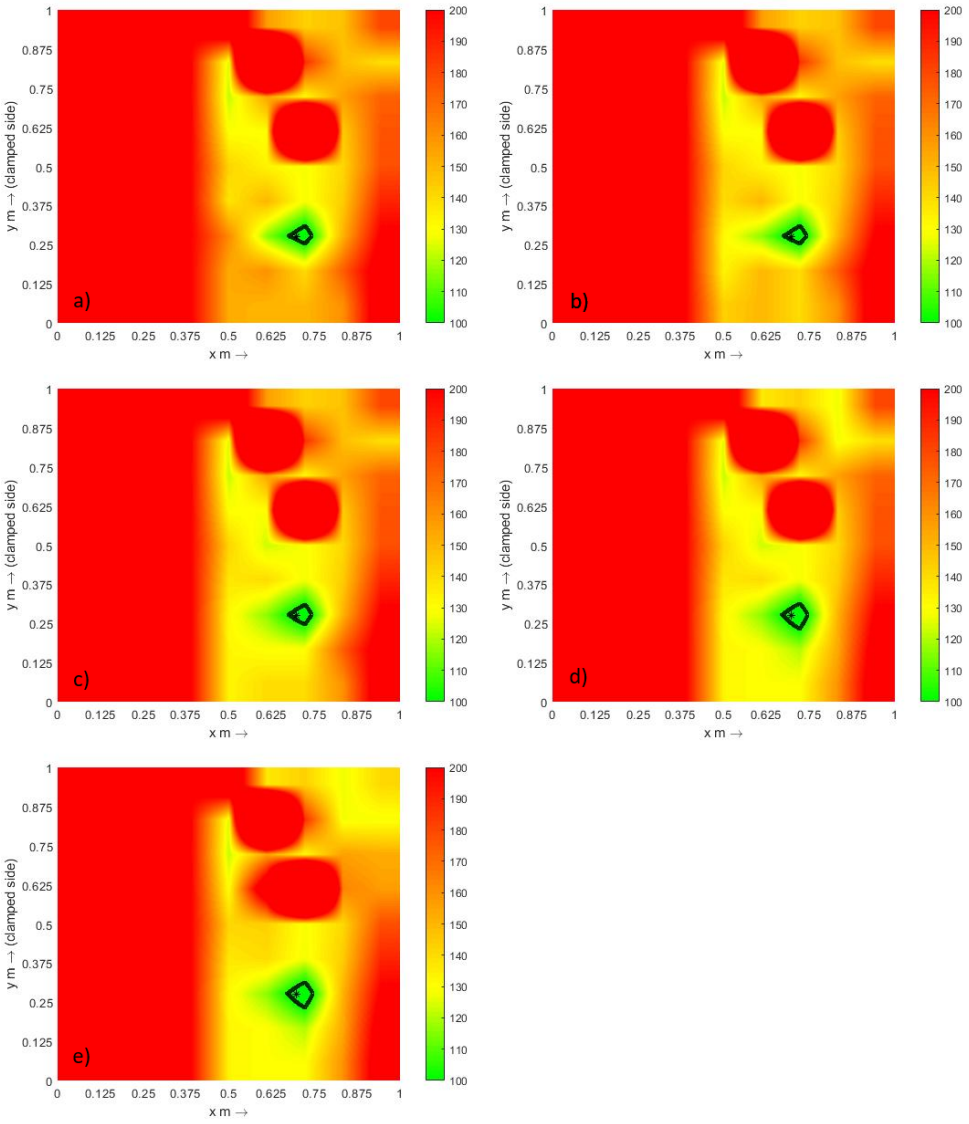

Figure 5.11: Estimated location of the applied load for arbitrary test point C using the finer grid. The actual location is marked by the asterisk. The estimation is shown for a) 5mm, b) 10 mm, c) 15 mm, d) 20 mm and e) 25 mm deflections.

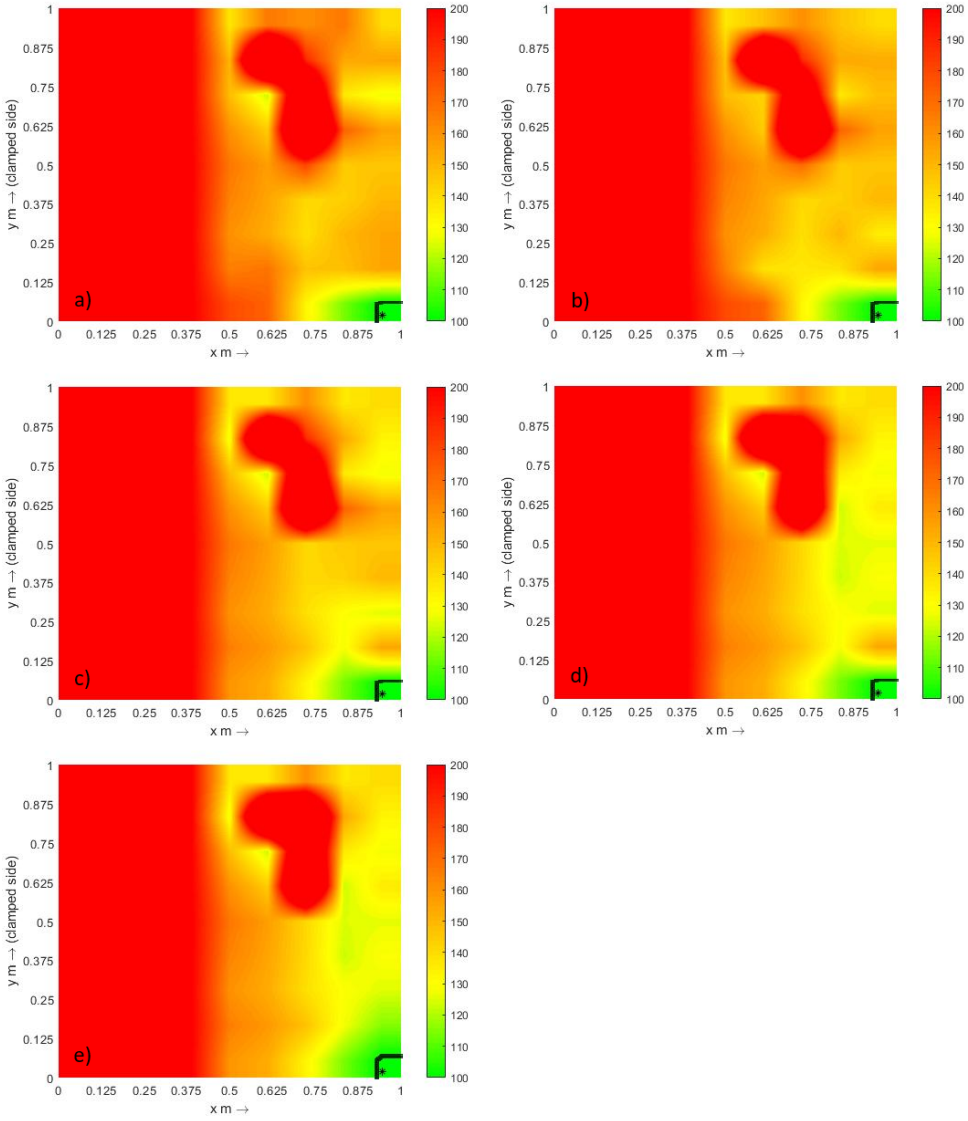

Figure 5.12: Estimated location of the applied load for arbitrary test point D using the finer grid. The actual location is marked by the asterisk. The estimation is shown for a) 5mm, b) 10 mm, c) 15 mm, d) 20 mm and e) 25 mm deflections.

5.4.2. Coarser grid

The understand the effect of lower calibration points, a coarser calibration grid was used. Each grid block was a rectangle of 250 mm x 333 mm. As mentioned in Section 5.3.3, with each iteration the CP data library is updated. An additional test was carried out to depict the result with an updated library. Figure 5.13 displays the position estimation map for test points A, B, C and D, respectively, for the case of the finer grid with a 3 x 3 grid pattern (Figure 5.7). Compared to the finer grid, this reduction in calibration points saw a decrease in estimation accuracy. The calculated error was up to 6% in the x-axis and 18% in the y-axis.

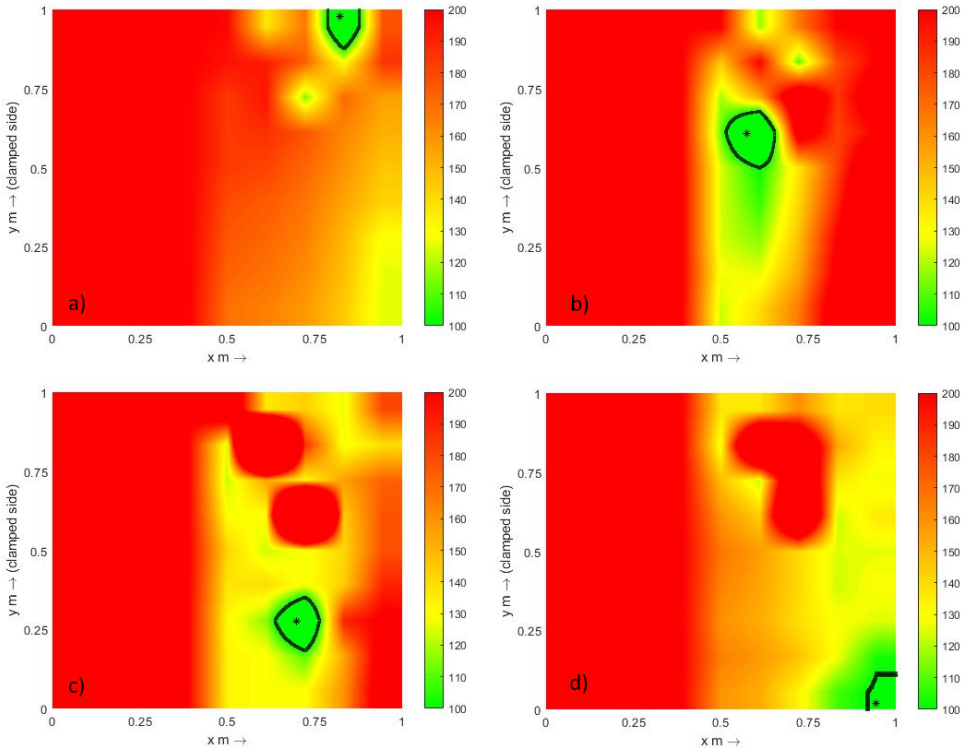

Figure 5.13: Estimated location of the applied load for arbitrary test points a) A, b) B, c) C and d) D, using the coarser grid. The actual location is marked by the asterisk. The estimation is shown for 20 mm deflection.

Overall, the estimations had a higher error due to an 80% decrease in the CP's. Nevertheless, in all the cases the actual loading point always fell within the estimated region. The highest error was in the y-direction estimation. This was because there were three CP's in the y-direction along a length of 1000 mm whilst in the x-direction the three points were along a shorter length (500 mm).

5.5. Discussion

Estimation of the location of an arbitrary load on the surface of a cantilever plate has been demonstrated. The multimodal sensing approach was adopted along with a novel algorithm to interrogate the plate within specified boundary conditions.

The plate was fixed like a flag in such a way that the thickness side faced the ground. Due to the cutting, clamping and bolting process, the plate had residual stresses and had visible uneven curvatures across its surface. The benefit of having an experimental based model was that the calibration tests capture the measurements taking into account these irregularities. Moreover, after each static test the sensor data was reset to be able to better compare all (and different) loading cases. The maximum deflections were when the load was acting at the tip end of the plate. Bending and torsion movements were of primary interest of the study for deflections up to 25 mm. A single optical fibre ran in a U shaped pattern along the length of the plate that consisted of four fibre Bragg grating sensors. As the tip of the plate experiences negligible strain (compared to those present at the root) the local measurements from sensors $S2$ and $S3$ were neglected. Moreover for smaller deflections these sensors did not show readings and did not have an effect on the final estimation. The measurements were carried out in the tip half of the plate (near the free edge) whilst the root half of the plate (near the clamped side) was not loaded. Two calibration grids were chosen. The dense grid consisted of 45 calibration points whilst the sparse grid consisted of mere 9 calibration points. The system in this chapter was calibrated for a single point force. It would be possible to estimate multiple points of deflection (or distributed loads) but this would require prior calibration.

Ideally, the sensor pairs $S1$-$S2$ and $S3$-$S4$ that run along the x-axis would have the same readings of ΔL and ε. This would hold true only if the following reasons are true. The plate does not undergo uneven bending, the length between each of the sensor pairs are the same and lastly, the position of the sensors are symmetric from the centre line. From the measurements we notice that there is an average of 25% difference in measurements between the sensor pairs. It can be inferred that the the errors stem from the three aforementioned reasons. The location of the gratings are specified as a range by the manufacturer which is basically an estimate. From practice it is seen that this estimate is generally more than three times the length of the grating itself. It would then also be difficult to place the other sensor pairs perfectly symmetrical to each other. A way to locate the exact position of the gratings though would be to study the side-lobe patterns of the grating spectrums [11]. The initial calibration step is important before the tests as it is carried out under the same fibre layout, sensors position and sensors configuration settings. This helps in making necessary adjustments in the calculation.

Temperature also plays a role in the sensor response. The source of these variations include the thermal expansion of the cyanoacrylate adhesive and that of the plate. These variations are slow and are filtered out at the interrogator level and hence do not exist in the final output signal. Moreover, a temperature fluctuation test showed that the variations in temperature within the lab were well within $\pm 0.5°$.

A great deal of effort went in to bonding the fibres (and in particular the effective sensing zone) properly. Fibres not bonded properly would not give consistent measurements throughout multiple trials. A series of repetitive trials were carried that showed consistency in the measurement readings. This confirmed that there was neither debonding nor incomplete bonding of the fibre to the plate.

Across all arbitrary test points (A, B, C and D) there was a uniform trend in the prediction of the estimated loading position. The estimations of the loading position were more accurate for smaller deflections and had greater errors for deflections above 20 mm. With an increase in deflections the uneven stresses in the plate also increased. This is noticed by the colour shift in the plate map that is also caused due to the uneven curvature and residual stresses. In case of a perfect plate profile, a completely red plate map would be achieved with a single green point marking the area of interest. The imperfections in the plate hence cause it to have an uneven and random map of red, orange, yellow and green on the plate. Regardless of the errors the actual loading point always fell within the estimated region.

This method can also help understand and bring forth essential data regarding the identification of the plate profile including curvature and geometry. The abrupt surfacing of such a colour map is also a function of erratic stress patterns in the plate. An example was the region around x,y = 0.6,0.7 m as it kept showing a red patch at a particular location through out all test cases.

This study takes in to account plate bending, torsion and its combinations. Higher order plate bending modes were not considered where complex bending was involved. Complex curvatures were prevailing mainly at areas closer to the root of the plate. The evidence to this is also the highest errors for test points B and C which were the two points closest to the root.

5.6. Concluding remarks

This second technical chapter is of complexity level II and presented the feasibility study and demonstration of the multimodal fibre optic sensing approach on plates. An experimental based model was used to have a better understanding of the plate under different loading conditions.

The aim of this work was to demonstrate 2 dimensional sensing by estimating the position and magnitude of an arbitrary load on cantilever structures. Four grating sensors were used through which local strain measurements as well as the displacement information between them was captured. With the starting shape of the plate known the final shape can be estimated based on the deflections taking place. The algorithm successfully estimated the position of an arbitrary load with an error of 9%. Bending and torsion of the cantilever plate was considered and the sources of error were identified and discussed. The importance of an initial calibration step was also explained. The study holds true for all cantilever structures geometry and material provided they exhibit elastic properties. The study was aimed towards bending of aircraft wing or wing sections.

This study opens up the idea for a higher complexity problem and will be extended to monitor more elaborate structures, including morphing aircraft wing sections. This method has been adopted to be able to accommodate structures whose structural response behaviour would be difficult to capture through analytical models. The following chapter discusses complexity level III that involves the monitoring of a morphing wing flap concept design.

References

[1] **N. Nazeer** and R. M. Groves. "Load Monitoring of a Cantilever Plate by a Novel Multi-modal Fibre Optic Sensing Configuration". In: *SN Appl. Sci.* 3.667 (2021). doi: 10.1007/s42452-021-04663-9.

[2] T. Jaramillo. "Deflection and moments due to a concentrated load on a cantilever plate of infinite length". In: *Journal of Applied Mechanics* 17.1 (1950), p. 67.

[3] H. Reismann and S. Cheng. "The edge reinforced cantilever plate strip". In: *Publication International Association for Bridge and Structural Engineering* 30 (1970), p. 149.

[4] S. N. Amiri, M. Hajali, and A. Esmaeily. "Exact Solution for Overhanging Slabs of Bridges under Arbitrary Concentrated Load Position". In: *Journal of Civil Engineering and Science* 3.1 (2014), pp. 1–13.

[5] R. Li, Y. Zhong, and B. Tian. "On new symplectic superposition method for exact bending solutions of rectangular cantilever thin plates". In: *Mechanics Research Communications* 38.2 (2011), pp. 111–116. doi: https://doi.org/10.1016/j.mechrescom.2011.01.012.

[6] D. L. Holl. "Cantilever Plate With Concentrated Edge Load". In: *Journal of Applied Mechanics* 4.1 (1937), A8–A10. doi: https://doi.org/10.1115/1.4008740.

[7] C. Fo-van. "Bending of uniformly cantilever rectangular plates". In: *Applied Mathematics and Mechanics* 1.3 (1980), pp. 371–383. doi: https://doi.org/10.1007/BF01874559.

[8] B. Tian, Y. Zhong, and R. Li. "Analytic bending solutions of rectangular cantilever thin plates". In: *Archives of Civil and Mechanical Engineering* 11.4 (2011), pp. 1043–1052. doi: https://doi.org/10.1016/S1644-9665(12)60094-6.

[9] R. T. Jones, D. G. Bellemore, T. A. Berkoff, J. S. Sirkis, M. A. Davis, M. A. Putnam, E. J. Friebele, and A. D. Kersey. "Determination of cantilever plate shapes using wavelength division multiplexed fiber Bragg grating sensors and a least-squares strain-fitting algorithm". In: *Smart Materials and Structures* 7.2 (1998), pp. 178–188. doi: 10.1088/0964-1726/7/2/005.

[10] W. Ko, W. L. Richards, and V. Fleischer. "Applications of KO Displacement Theory to the Deformed Shape Predictions of the Doubly-Tapered Ikhana Wing". In: *NASA/ TP-2009-214652* (2009).

[11] A. Rajabzadeh, R. Heusdens, R. Hendriks, and R. M. Groves. "A Method for Determining the Length of FBG Sensors Accurately". In: *IEEE Photonics Technology Letters* 31.2 (2019), pp. 197–200. doi: 10.1109/LPT.2019.2891009.

6

Monitoring of a Morphing Wing Mock-up

This chapter forms the basis of understanding the multimodal sensing approach on morphing wing-like structures. The study addresses Research Question 3 that falls under Complexity Level III and is focussed on shape estimation of a mock-up morphing wing on a test bench. The novelty of the research in this chapter lies in the demonstration of the multimodal sensing approach for monitoring of morphing-like wing sections with a single optical fibre. The aim of this work is to be able to estimate the deflection of the trailing edge of the wing due to arbitrary morphing. By using four fibre Bragg grating sensors bonded on the top and four on the bottom section of the wing, the shape of the wing before and after the deflections is estimated. An experimental based model is used that involves an initial calibration to compare and facilitate the experimental measurements. The results show a good proximity to the actual values and a recommendation on the most favourable fibre location is made. This chapter lays the foundation to investigate a higher complexity case involving bending, torsion and their combinations on a full scale morphing wing demonstrator in the wind tunnel.

Parts of this chapter have been published in Sensors 22, 2210 (2022) [1].

6.1. Introduction

This chapter aims to address RQ3 which is a development over the the previous 1D beam and 2D plate studies. The aim of this chapter is the monitoring of a morphing wing (mockup) section on a test bench in the laboratory. The shape of a morphing wing is of interest as it undergoes multiple deformations at different flight regimes. Monitoring the shape provides vital information for the flight controller in terms of keeping track of the morphing section and optimising the flight. This is also important as it could alert the user when the structure starts behaving outside its design limits. This chapter includes the implementation of the understanding from RQ1 and RQ2 to monitor the morphing behaviour. Recommendations on the most favourable fibre/sensor location are also studied. The sensing methodology is similar to the previous cases where fibre Bragg grating sensors are used to measure local strain measurements as well as the displacement between any two sensors. Using the proposed hybrid sensing principle the morphing behaviour is estimated for different morphing cases. This chapter falls under the Complexity Level III category where the bending and torsion of a realistic sized morphing wing section is studied.

As a proof of concept, this method is demonstrated on a mockup section that imitates the behaviour of a morphing wing trailing edge flap. This mockup section has fewer moving parts and is self-contained. The mechanism adopted here was inspired by the skin warping and bending concept [2] for morphing trailing edge deflection and is part of the larger SmartX project (refer to Section 1.5). This work also forms a preliminary step in understanding the behaviour of the morphing mechanism and to optimise the sensing capability of the system.

The structural design of a morphing structure has several aspects to consider. It is required to be rigid as well as flexible and at the same time to carry out the morphing sequences whilst sufficiently taking up all the aerodynamic loads. This is particularly challenging for the morphing design as it must be capable of resisting high in-plane strains whilst also having low in-plain stiffnesses. Moreover, an adequate amount of out-of-plane stiffness would also be required to resist the aerodynamic loads as well as local buckling [3]. For a complex system like this, deflection monitoring plays a key role in understanding the behaviour of the structure and also in making sure it is operating within its design limits. This information can also be used to track the movements of the structure and hence estimate its shape throughout the morphing sequence. The work here mainly focusses on simultaneously monitoring these morphing movements for shape sensing and load monitoring purposes.

The primary focus of this work is to characterise the shape sensing performance of the optical fibre sensing fibre sensing principle for a morphing wing.

6.2. Morphing-wing mockup

The geometry and coordinate system of the specimen used is as shown in Figure 6.1 along with the nomenclature used. The test specimen is a pseudo wing-section consisting of two parts that are referred to as the top section and

the bottom section. These two surfaces are part of a single construction formed by bending of an aluminium sheet over an actual conventional wing section. The geometric properties of the wing are as shown in Table 6.1. The top and bottom sections of the wing have a chord c, span s, and thickness t, with an approximate NACA 2519 profile. The fixed and free ends of the wing section are denoted further on as the root and the tip, respectively. The deflection happens in the y-axis which varies along the chord depending on the actuation and the morphing sequence. This wing section would be hereon referred to simply as the 'wing'.

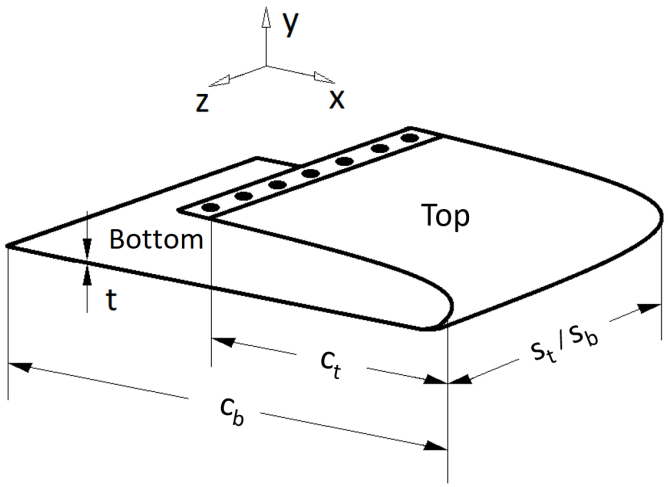

Figure 6.1: Geometry and coordinate system of the test wing section.

The wing undergoing bending in the negative y-axis indicates that, for the top section, the upper surface undergoes tension whilst the lower surface undergoes compression. At the same time, for the bottom section, the upper surface undergoes compression whilst the lower surface undergoes tension. The three assumptions mentioned in Section 5.1 hold true for the wing. With reference to the wing, they specify that no shearing takes place in the top and bottom sections, the neutral axes of the sections remains un-deformed and the wing morphing takes place within a predefined range.

Table 6.1: Material and geometric properties of the wing.

Property	Variable	Value
Material		Aluminium
Chord (top)	c_t	343 mm
Span (top)	s_t	350 mm
Chord (bottom)	c_b	570 mm (343 + 227)
Span (bottom)	s_b	350 mm
Thickness	t	1 mm

6.2.1. Setup

The experimental setup is as shown in Figure 6.2. The test-bench was a letter 'H' construction made using aluminium beams (Boikon). The shape of the test-bench was similar to that of a rugby goal post. The two vertical uprights were 585 mm tall, 40 mm wide and were attached firmly to the optical table 590 mm apart. The horizontal crossbar of the goal post was 590 mm in width and 95 mm from the optical table. The horizontal cross bar was securely connected to the two uprights and sat snugly in between them.

The top section of the wing was bolted to the top of the horizontal cross bar. It was positioned at the centre of the cross bar making it ~120 mm from each of the vertical uprights. On the other hand, the bottom section of the wing was left to hang under gravity. The only connection point of the wing to the horizontal crossbar was the top section of the wing.

An FBG spectral interrogator (National Instruments, PXIe-4844) measured the local strain (ε_{1-n}) at each of the FBG locations with a resolution of 4 pm, an accuracy of 4 pm and a dynamic range of 40 dB in a wavelength range from 1510 nm to 1590 nm. A second interrogator (Optics11, ZonaSens) measured the displacement (ΔL_{i-j}) between FBG-Pairs with a resolution of 1 pm, an accuracy of 10 nm and a dynamic range of 160 dB in a wavelength range from 1530 nm to 1560 nm. These two interrogators operated with their own light sources that were tunable wavelength-swept lasers of class 1M. Specious measurements were noted when light sources of both the interrogators ran together through the same fibre. This was overcome by using an optical switch (Thorlabs, OSW22-1310E) with an automated switching algorithm operated in LabVIEW.

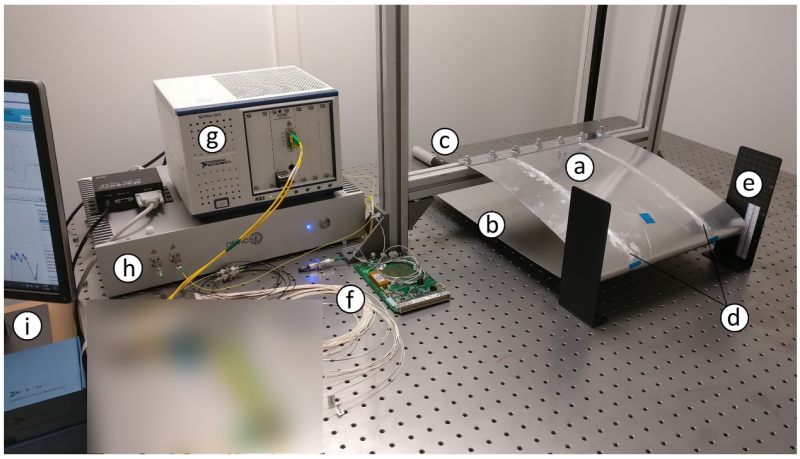

Figure 6.2: The experimental setup showing the test wing's (a) fixed top surface, (b) sliding bottom surface, (c) actuator (up close in Figure 6.4), (d) sensing fibres (e) vertical scales, (f) optical switch, (g) National Instruments interrogator, (h) Optics11 interrogator and the (i) data acquisition system.

In order to introduce movements to the wing, the bottom section was allowed to slide along the x-axis. Figure 6.3 shows the side view of the wing depicting the fixed top section and moving bottom section. For higher levels of defection involving twist, the wing resisted the actuation from one side due to how the wing was shaped. This was overcome by allowing the bottom section to move in the z-axis so as to allow the two sides of the wing to deflect in opposite ($\pm$y-axis) axes. As the resistance was higher than the force applied by the actuator, an asymmetric bending motion was introduced for lower deflection levels. The ranges for different movements of the wing are explained in detail in Section 6.3.2. As the top section was fixed, the curved part of the wing due to this motion moved up and down causing deflection in the y-axis. To facilitate this movement in a controlled manner, the bottom section of the wing had a longer chord to which an actuator was attached. The bottom section was moved using a linear actuator (PI, M-235) through a DC motor controller (Mercury, C-862) and a sliding stage.

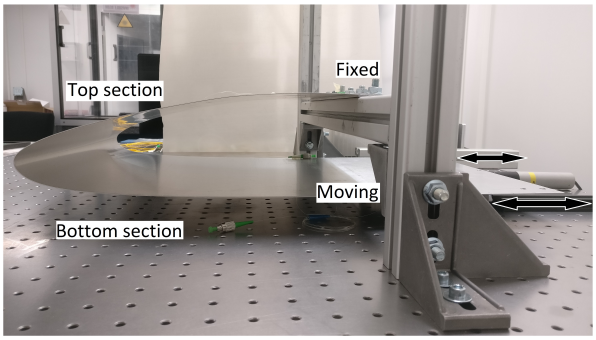

Figure 6.3: Side view of the wing attached to the support beams. The top section is fixed whilst the bottom section is allowed to slide.

Figure 6.4 shows the actuator detached and revealed. The actuator was connected to the optical table through a fixed base plate. A spring loaded moveable stage plate was connected to the bottom section of the wing; it was capable of introducing movements with a travel range such that the wing deflected up to a maximum of 30 mm whilst allowing a rotation of 40° at the root.

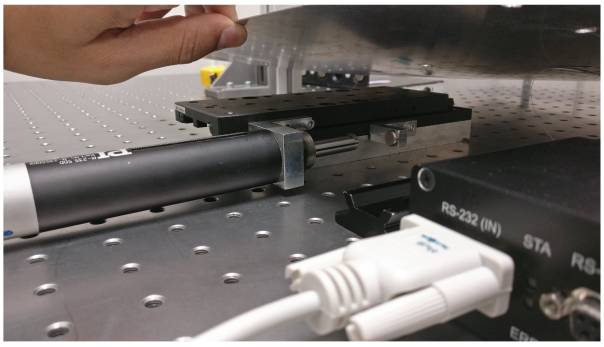

Figure 6.4: The actuation mechanism showing the actuator attached to a fixed base plate and a moveable spring loaded stage plate. The controller is in the foreground.

6.2.2. Sensor design

Figure 6.5 is a top-view of the wing showing the sensing fibre (in red) and its layout along with the grating sensors. Two standard single mode (SM) SMF-28e+ (Corning) fibres containing the grating sensors were bonded using cyanoacrylate adhesive (3M Scotch-Weld), one each on the surfaces of the top and bottom sections of the wing. For the top section, the fibre was bonded to its upper surface whilst for the bottom section the fibre was bonded to its lower surface. This was done due to ease of access as the fibre bonding process was initiated after the wing was brought to shape.

Gratings on the top section are marked as $S1$, $S2$, $S3$ and $S4$ and on the bottom section with asterisks as $S1^*$, $S2^*$, $S3^*$ and $S4^*$. The bottom surface fibre (and gratings) is a superimposition of the top surface fibre positions. It is to be noted that the fibre length between gratings $S2/S2^*$ and $S3/S3^*$ had no effect in the sensing and was hence simply partly taped and partly left free. FC/APC connectors were used for all the fibre connections.

The fibre layout and sensor placement design was adopted from the plate monitoring study (Chapter 5) which specifies the importance of having sensors placed relatively close to the clamped-free (x-axis) boundary as well as having at least two sensors in the free (z-axis) boundaries of the section. Apart from this each sensor should form a pair with an adjacent sensor running chordwise, to satisfy the FBG-Pair configuration [4].

The layout of the fibres is a U-shape pattern such that all the gratings are perpendicular to the y-axis. One end of the each fibre is connected to a switch whilst the other end is connected to an attenuator/light trap (Thorlabs, FTAPC1) with a return loss of $\geqslant$ 50 dB to reduce back reflections into the sensing fibre. Gratings $S1/S1^*$ and $S4/S4^*$ are at approximately 50 mm from the root and $S2/S2^*$ and $S3/S3^*$ are at 315 mm. The gratings measure the normal strains acting in the x-axis direction.

The nominal Bragg wavelengths as specified by the manufacturer (FORC-Photonics) of the gratings are mentioned in Table 6.2. As in the previous tests, gratings of length 3 mm each were chosen. To achieve best results with the interrogators, bandwidth and reflectivity levels were specified to be above 0.5 nm and 99 %, respectively. The temperature sensitivity of the sensors was as low as 10 pm/°C.

Table 6.2: Properties of the fibre Bragg grating sensor pairs $S1/S1^*$, $S2/S2^*$, $S3/S3^*$ and $S4/S4^*$ (FORC-Photonics). Unlike other sensor pairs, $S3/S3^*$ had different wavelengths and are mentioned separately.

Property	S1/S1*	S2/S2*	S3	S3*	S4/S4*
Wavelength	1529.3 nm	1539.3 nm	1549.4 nm	1549.1 nm	1559.4 nm
Bandwidth	← 0.5 ±0.1 nm →				
Reflectivity	← $\geqslant$ 99 % →				
Temp. sensitivity	← 10 pm/°C →				

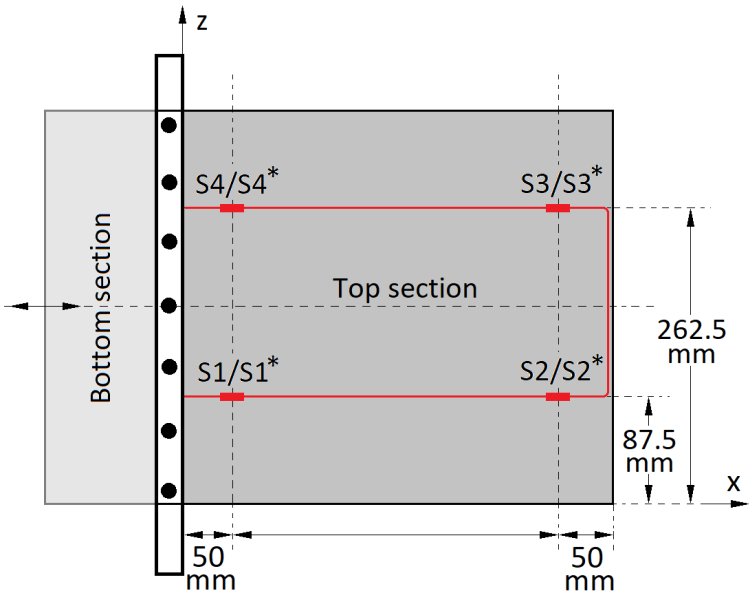

Figure 6.5: Top-view of the wing with the optical fibre running along the x-axis in the bulk of the top (and bottom) section(s). The grating sensors $S1$, $S2$, $S3$ and $S4$ are on the top section. The sensors on the bottom section are a superimposition of the top sensor positions marked with asterisks ($*$); (eg., $S1$ is directly above $S1^*$ and so on).

6.3. Measurements

The measurement approach involved an initial calibration of the wing followed by the development of a shape sensing tool. The first step was to record baseline measurements in order to develop an experimental based wing model. A transfer function model was then used to estimate the deflection and the final shape. The experiments were carried out on different morphing cases that were brought about through the actuator. The following sub-sections describe the morphing cases used in the experimental campaign, the calibration procedure for the wing and the series of tests involving arbitrary morphing to later estimate the deflections and the morphed shape.

6.3.1. Morphing cases

The wing undergoes different movements based on the actuator input. These movements are classified into four primary movements or morphing cases. The morphing cases include pure bending, torsion and a combination of bending and torsion of the wing. The morphing cases are termed bend-up, bend-down, left-twist and right-twist. Their (maximum) morphing positions are as shown in Figure 6.6.

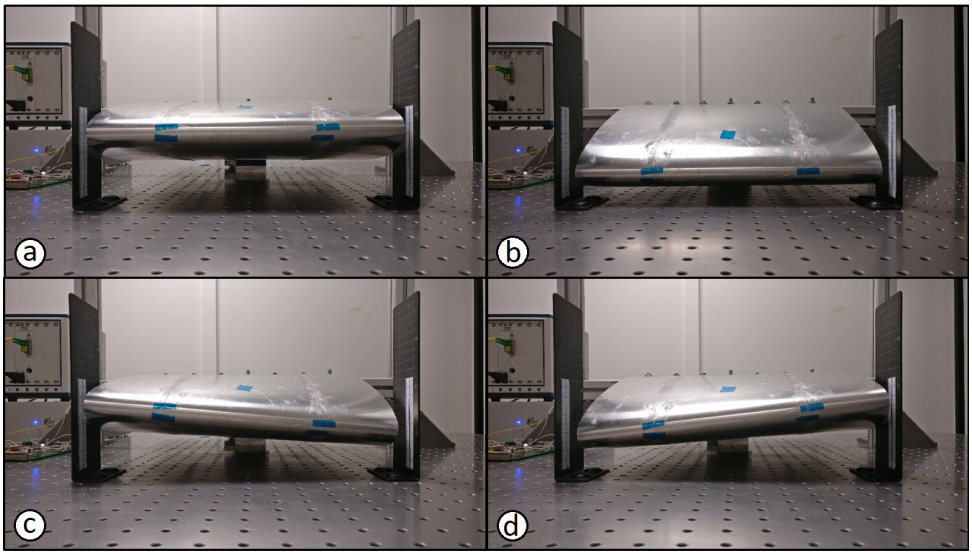

Figure 6.6: The position of the wing during a) bend-up b) bend-down c) right-twist and d) left-twist morphing cases.

6.3.2. Calibration

The calibration tests were performed using the same setup as in figure 6.2. The maximum and minimum ranges of deflection were mainly determined based on the actuator's range of 50 mm. The required deflections of the wing were taken into account and the ranges were set and are shown in table 6.3. This was necessary to confirm that all morphing cases could be accommodated as well as to ensure a total 50 mm wing tip deflection based on the actuator range.

The actuator had a push/pull force capacity up to 120 N which was sufficient to bring about all morphing scenarios . It is to be noted that the trailing edge line (along the z-axis) was assumed to be straight throughout the tests.

Table 6.3: Allowable movement ranges specified and set by the calibration procedure to adhere to the structural design limits. This pertains to the actuator (x-axis) and the deflection of the wing tip (z-axis).

Parameter	Bend-up	Bend-down	Twist
Actuator (x-axis)	-25 mm	+25 mm	±15 mm
Tip deflection (z-axis)	-20 mm	+40 mm	±15 mm

6.3.3. Arbitrary morphing

In these experiments the wing was morphed with unknown actuations which result in unknown deflections. They are divided into bending and twisting cases with four arbitrary cases each. These cases are termed as A, B, C and D for bending and E, F, G and H for twisting. For a bending case, the values of ΔL_{1-2} and ε_1 should measure the same as ΔL_{3-4} and ε_4, respectively. This does not hold true for twisting. This difference is accounted for in the algorithm. A random number function was used to generate unknown actuation cases for morphing. On purpose, values of 0, mid and max wing deflections were excluded as they were already included in the calibration step. The actuation was set to input values at steps of 1 mm.

The actual wing deflections for each of the morphing cases were later measured and recorded. Tables 6.4 and 6.5 show the right and left wing tip deflection separately for bending and twisting morphing cases, respectively.

Table 6.4: Actual deflections of the wing during bending due to arbitrary morphing A to D.

Morphing	δ_{right} (mm)	δ_{left} (mm)
A	-7	-7
B	-16	-16
C	13	13
D	28	28

Table 6.5: Actual deflections of the wing during twisting due to arbitrary morphing E to H.

Morphing	δ_{right} (mm)	δ_{left} (mm)
E	9	-9
F	12	-12
G	-3	3
H	-13	13

6.3.4. Algorithm

The algorithm relies on a transfer function from the measured strain output due to actuator movement to the trailing edge tip deflection. This was attained by relating the raw FBG and $FBG - Pair$ data to the tip deflection.

A wing-morphing → sensing-fibre-strain → trailing-edge-deflection type transfer function was used to correlate the measurement data with the wing trailing edge deflection.

Twisting of the wing is an important aspect that needs to be captured as it is part of the morphing capabilities of the a seamless wing/flap. In order to discern and distinguish the twisting motion in the wing, separate transfer functions were used for right and left twist.

Bending of a beam is a simpler motion that can be modelled using a linear interpolation approach. In this case a quadratic interpolation was utilised to account for any non linearity.

To satisfy the condition of bending, the strain at all the points that are equidistantly measured from the root along the span should be the same. This means that a single ε *FBG* measurement along with a single ΔL *FBG-P* measurement should suffice. The transfer function can hence be expressed as:

$$\delta = a.\varepsilon_{1/4}^2 + b.\Delta L_{1-2/3-4} + c, \tag{6.1}$$

where δ is the deflection of trailing edge line (along z-axis). The coefficients a, b and c of the variables (ε and ΔL) are equal to -0.00012, -0.14 and 0.023, respectively, for bend down and -0.00017, 0.16 and 1.8, respectively, for bend up. The coefficients are constant for an experiment campaign and are determined by curve fitting. Based on the calibration procedure, the measurements are sensitive to the errors in the coefficients and can have a maximum coefficient deviation of ± 1.3393.

The measurement data ε_1 and ε_4 particularly came into play when the positive and negative twists, respectively, were involved. To accommodate this, Equation 6.1 was separated into two transfer functions corresponding to positive and negative twisting.

The positive twist (right tip deflection), δ_{right}, was expressed as:

$$\delta_{right} = d.\varepsilon_1^2 + e.\varepsilon_4 + f.\Delta L_{1-2} + g, \tag{6.2}$$

and the negative twist (left tip deflection), δ_{left}, as:

$$\delta_{left} = h.\varepsilon_1^2 + i.\varepsilon_4 + j.\Delta L_{3-4} + k, \tag{6.3}$$

where d to k are again coefficients of the variables equal to -0.00031, 0.12, 1.5, -0.00039, -0.13 and 1.9, respectively. The coefficients are constant for a given experiment campaign and are determined by curve fitting. Based on the calibration procedure, the measurements are sensitive to the errors in the coefficients and can have a maximum coefficient deviation of ± 2.408.

This separation was done in order to better capture the whole shape of the wing. Moreover, this method also covers equation 6.1 that considers bending of the wing.

From equations 6.2 and 6.3 it can be proven that δ_{right} would equal δ_{left} when $\varepsilon_1 = \varepsilon_4$ and $\Delta L_{1-2} = \Delta L_{1-2}$. This satisfies the pure bending condition.

6.4. Results

Experiments pertaining to the four morphing cases were carried out following the procedure elaborated in section 6.3. Figures 6.7 to 6.9 and Figures 6.10 to 6.12 show the strain output of the sensors for their respective deflection for the top and bottom section, respectively. The positive and negative values imply that the fibres (and in turn the sensors) undergo tension and compression, respectively. Theoretically, for a bend up (and bend down), sensor pairs $S1$ and $S4$ should be the same (in magnitude and trend) and so should sensors pairs $S2$ and $S3$. On the other hand, in case of twist these pairs should also show the same readings but with opposite polarity (Figures 6.9 and 6.12). The slight offset between the two could mean one of the following; a) one side is being bent more than the other or b) the grating is closer to the root than the other grating causing it to experience higher strain. In twist, this disparity increases because the difference between the pairs themselves is added to the deflection error. Generally, the offset due to the errors resulting from improper fibre positioning and/or sensor position is already corrected at the strain calculation level. In this study, the focus of study was mainly on the trend they followed and hence the average of the pairs are shown. Comparisons of the estimated deflections with the actual deflections are tabulated in the following section.

For the top section, a clear distinction between the sensors near the root ($S1$ and $S4$) and at tip ($S2$ and $S3$) was noticed for the bend cases (Figures 6.7 and 6.8). Although the max deflection was higher for bend down than bend up, the trend line was similar for both the cases. Moreover, although the twist case (Figure 6.9) showed low strains for small deflections, it also had similar trend as the bend cases.

On the other hand, the sensors on bottom section had a different behaviour for both the bend and twist cases. Since the configuration of the bottom section was not similar to a cantilever setup, the sensors near the root ($S1$ and $S4$) and at tip ($S2$ and $S3$) did not have a clear distinction for bending (Figures 6.11 and 6.10). Unlike the top section, the bottom section experienced a sliding motion apart from the bending motion. In the bend down case, for the first few mm the sliding motion was dominant and hence no strain was experienced. This explains the flat line from 0 mm to 4 mm.

The biggest difference was seen in the twist case (Figure 6.12) where a messy pattern was observed. Again, this was attributed to the bottom section undergoing a combination of sliding and bending. In addition to that, as explained in Section 6.2.1, the bottom section also had movements in the z-axis that introduced strain that are not along the axis of the fibre.

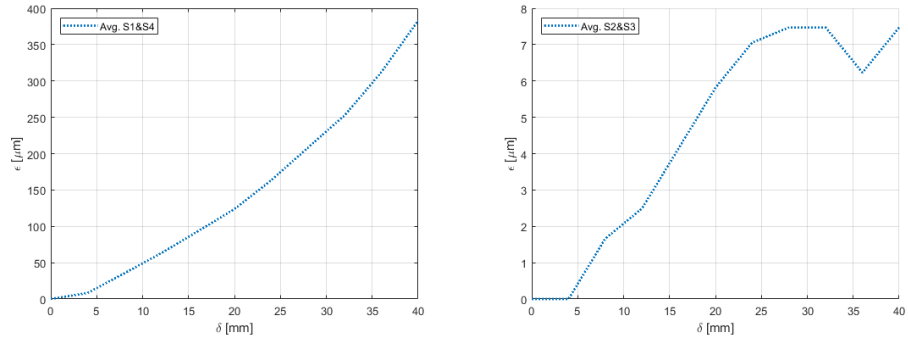

(a) (b)

Figure 6.7: Strain trend in the top section of the wing through sensors a) $S1$ and $S4$ and b) $S2$ and $S3$, undergoing bend-down with respect to deflection due to morphing. Separate figures are used due to the large variation in scales.

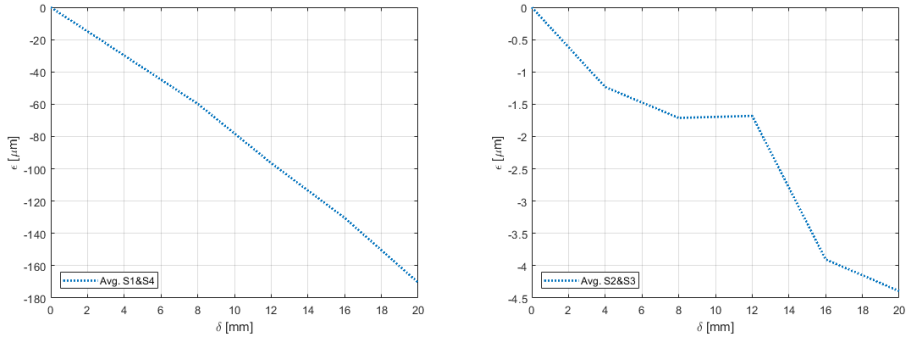

(a) (b)

Figure 6.8: Strain trend in the top section of the wing through sensors a) $S1$ and $S4$ and b) $S2$ and $S3$, undergoing bend-up with respect to deflection due to morphing. Separate figures are used due to the large variation in scales.

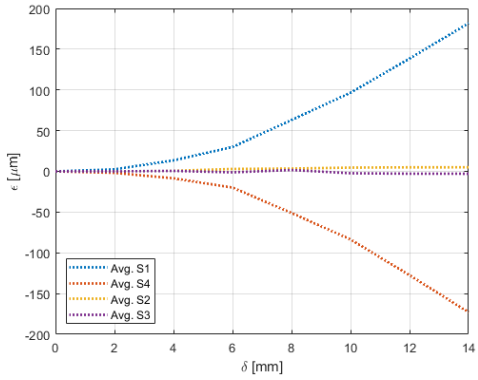

Figure 6.9: Strain trend in the top section of the wing undergoing twist with respect to deflection due to morphing.

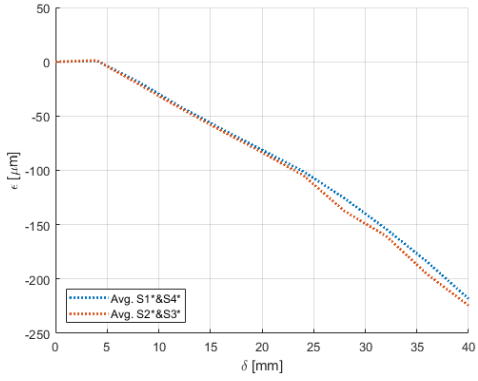

Figure 6.10: Strain trend in the bottom section of the wing undergoing bend-down with respect to deflection due to morphing.

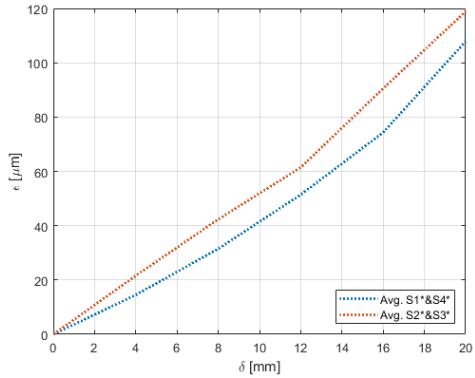

Figure 6.11: Strain trend in the bottom section of the wing undergoing bend-up with respect to deflection due to morphing.

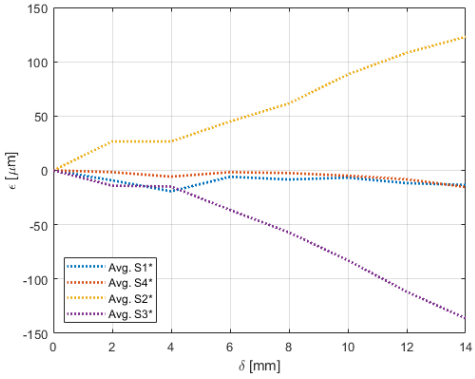

Figure 6.12: Strain trend in the bottom section of the wing undergoing twist with respect to deflection due to morphing.

6.4.1. Arbitrary morphing

Eight arbitrary morphing cases were tested and their estimated deflections were compared with the actual deflections. The error in the estimated deflections for morphing cases A to D are as shown in table 6.6 which had a maximum error of 0.45 mm. Tables 6.7 and 6.8 show the estimated deflections for morphing cases E to H which had a maximum error of 0.74 mm.

Table 6.6: Model estimated deflections of the wing during bending due to arbitrary morphing A to D.

Morphing	Actual δ (mm)	Estimated δ (mm)	Maximum error (mm)
A	-7	-6.893	0.107
B	-16	-15.94	0.06
C	13	12.55	-0.45
D	28	28.59	0.59

Table 6.7: Model estimated right deflections of the wing during twisting due to arbitrary morphing E to H.

Morphing	Actual δ_{right} (mm)	Estimated δ_{right} (mm)	Maximum error (mm)
E	9	9.311	0.311
F	12	12.53	-0.74
G	-3	-2.492	0.596
H	-13	-13.21	0.34

Table 6.8: Model estimated left deflections of the wing during twisting due to arbitrary morphing E to H.

Morphing	Actual δ_{left} (mm)	Estimated δ_{left} (mm)	Maximum error (mm)
E	-9	-9.212	0.311
F	-12	-12.74	-0.74
G	3	2.596	0.596
H	13	13.34	0.34

6.5. Discussion

The estimation of the deflection due to arbitrary morphing on a morphing wing mockup has been demonstrated and includes bend up, bend down and twist of the wing. The wing morphing was facilitated by an actuator that was attached to the sliding bottom section of the wing. The aim of the study was also to understand

the difference between placing the sensing fibre at two locations on the wing and concluded the most desirable location.

The measurements were recorded through two optical fibres bonded on each to the top and bottom sections of the wing. They were single-core SM fibres containing two pairs of fibre Bragg gratings each. The experiments were conducted within a controlled laboratory environment where the temperature variations were significantly low. The temperature was assumed to be constant throughout the experiment.

For any morphing sequence, the change in shape of the wing was measured in terms of strain on the fibres. The sensors placed closer to the clamp pick up local strain whilst the sensors on the free end do not measure this as the end had a free boundary condition. The sensors at the free end were used to measure the displacement along the chord of the wing as they formed sensor pairs with the sensors near the clamp. Using the reference measurements as baseline data the algorithm predicted the deflection of the trailing edge. The trailing edge line (along the z-axis) was assumed to be straight throughout the experiment. Due to the thickness of the material being negligible compared to other dimensions the shear strains on the wing are not considered here.

The wing had a natural bend due to gravity and reference zero strain values were measured after the wing was suspended. On being morphed, two local strain readings were obtained near the wing root of the top section. As the other sides of the top section were not fixed, the maximum strain was always near the clamp (similar to a cantilever case). The other set of measurements were the two strain components along the chord of the wing that were similar during bending and different during twisting.

The trailing edge was displaced along the y-axis by the movement of the bottom section. The trailing edge had a maximum dip of 40 mm that gradually reduced to 0 towards the clamped region. A symmetric behaviour was also noticed when the sliding (bottom) section was displaced (to a maximum of 20 mm) but in the positive x-direction. To distinguish these two cases, the distinction between compression and tension induced strain was identified at the interrogator level by the sign of the strain. This was also crucial because it helped in identifying the positive and negative wing movement which was essential for shape sensing. This also confirms the placement of the fibres on each surface. For the top section the fibre was placed on its upper surface such that during a bend-down the fibre experienced tension and vice versa. It was noticed that the tip (trailing edge line) no longer had the highest deflection point in a twist configuration. The actuator had to put in extra effort for twist and the maximum dip achieved for the trailing edge deflection was $\pm$14 mm but still following symmetry.

On the whole, the shape of the morphing wing was estimated within 1 mm of the trailing edge deflection. For lower deflections up to ~10 mm the estimation was almost linear. The non linearity gradually increased for higher deflections which also signified the wing leaving the cantilever domain. For deflections higher than 10 mm, small increases in the actuator input gave rise to increasingly higher trailing edge deflections. This was due to the surface experiencing a slight curving effect.

Hysteresis tests were carried out by gradually deflecting the wing from 0 mm all the way to the higher limits and back to 0 mm. The hysteresis detection limit was set as 1 mm. For all the trials the wing showed no hysteresis when measured on the vertical scale. Moreover, the actuator was measured to have a position accuracy of 0.0002 mm whose effect on the estimation was negligible.

The fibre on the top section on comparison with the bottom section gave a better distinction between the sensors near the clamped end and the free end. Moreover, the twist case for the bottom section had a messy trend as compared to a more discernible and smooth trend for the top section. The presence of a sensing fibre on the top section alone would hence suffice for the deflection estimation.

A limitation here is that bend up/down and twist readings were measured separately. Although the aluminium wing construction was flexible, it resisted the movement from one side during a twist inducing morphing, making the twisting motion difficult. For example, the actuation required for an x mm bend down was not equivalent to an x mm twist. To tackle this, a mechanism would be required to isolate both the sides of the wing so that they could operate similar to a twist. In other words, the movement for a one-sided twist should be equivalent to the movement of a one-sided bend. A way to realise this would be to consider the (top and bottom) section of the wing as two individual wings joined together. This could be visualised from Figure 6.1 by drawing a line along the x-axis in the middle of the wing considering it to divide the wing into two halves. Each half would have its dedicated actuator. But, this would create issues like gaps and an uneven surface. An alternative would be to have a region in between them that is strong yet flexible enough to overcome the issues mentioned above, that is, to have a smooth surface with no gaps and hence no/low resistance when the two wing sections are morphed independently.

As for the fibre layout, placing the fibre in a diagonal orientation might be good to pick up twist but would reduce sensitivity during bending. To overcome this a rosette pattern could be used but this basically means using additional gratings in the fibre. Doing so would directly go against the focus of this work, i.e., to use the least number of sensors.

6.6. Concluding remarks

This third technical chapter is of complexity level III and presented the feasibility study and demonstration of the multimodal fibre optic sensing approach on morphing wing mock-ups. An experimental based model was used to have a better understanding of the wing under different morphing cases.

The aim of this work was to demonstrate shape sensing by estimating the trailing edge deflection due to arbitrary morphing movements on wing sections. Furthermore, a recommendation on the most desirable location to place the sensing fibre was made.

The fibre on the top section had better capabilities of monitoring bending and twisting of the wing. For small deflections the estimation resembled a wide cantilever beam. The width was not a determining factor in the estimation as the

deflection was independent of the width of the wing. For higher deflections a slight non-linearity was noticed which was attributed to the curving of the wing surfaces. Based on the calibration data a transfer function model was used to estimate the trailing edge deflections. Since a better distinction was possible using the sensor readings on the top section of the wing, it was concluded that having the top fibre alone was sufficient.

Although the model has been developed around the morphing trailing edge, this approach can potentially be used to model any morphing structure, regardless of its material provided they exhibit elastic properties. Furthermore, this study opens the design space for future designs and design iterations of the morphing wing. As materials properties are not a constraint, with proper calibration, full composite wing structures can also be studied.

This study opens up the idea for a higher complexity problem and is extended to monitor a composite morphing wing section. The following chapter discusses complexity level IV that involves the monitoring of the SmartX wing demonstrator in the wind tunnel.

References

[1] **N. Nazeer**, R. M. Groves, and R. Benedictus. "Assessment of the Measurement Performance of the Multimodal Fibre Optic Shape Sensing Configuration for a Morphing Wing Mockup". In: *Sensors* 22.6 (2022). doi: 10.3390/s22062210.

[2] N. Werter, J. Sodja, G. Spirlet, and R. de Breuker. "Design and Experiments of a Warp Induced Camber and Twist Morphing Leading and Trailing Edge Device". In: *24th AIAA/AHS Adaptive Structures Conference* (2016), pp. 1–20. doi: 10.2514/6.2016-0315.

[3] F. Gandhi and P. Anusonti-Inthra. "Skin design studies for variable camber morphing airfoils". In: *Smart Materials and Structures* 17.1 (2008), p. 015025. doi: 10.1088/0964-1726/17/01/015025.

[4] **N. Nazeer** and R. M. Groves. "Load Monitoring of a Cantilever Plate by a Novel Multi-modal Fibre Optic Sensing Configuration". In: *SN Appl. Sci.* 3.667 (2021). doi: 10.1007/s42452-021-04663-9.

7

Monitoring of the SmartX Wing Demonstrator

This chapter forms the basis of understanding the multimodal sensing approach on a full scale composite morphing wing. The study addresses Research Question 4 that falls under Complexity Level IV and is focussed on shape estimation of the SmartX-Alpha wing morphing modules in the wind tunnel. The novelty of the research in this chapter lies in the capability of the multimodal sensing approach for shape sensing of morphing wing sections in the wind tunnel and the capability of measuring the effectiveness of the actuation. The aim of this work is to be able to estimate the deflection of the trailing edge of the wing during a series of load alleviation tests. By using four fibre Bragg grating sensors bonded on the morphing modules, the shape of the modules during morphing can be estimated. An experimental based model is used that involves an initial offline calibration as reference and to facilitate the wind tunnel measurements. The results show a good proximity to the actual values and the errors are discussed. The predominant source of error is identified and the capability of the sensing method to detect and quantify this error is acknowledged. The method also helps in understanding the actuator effectiveness during morphing.

Parts of this chapter have been published in Actuators 10, 107 (2021) [1].

7.1. Introduction

This chapter aims to address RQ4 which is a development over the the previous morphing wing mock-up investigation. The aim of this chapter is the monitoring of the SmartX wing (called the SmartX-Alpha) in the wind tunnel and the demonstration of the capability of the shape monitoring tool. The estimation will be done using a single-core optical fibre sensor followed by evaluating the actuator effectiveness during morphing through a series of Manoeuvre Load Alleviation (MLA) tests. The details are elaborated in the following sections. In order to obtain the exact control setting, information of the shape of control surfaces is required. This is also beneficial for close-loop control. The morphing control surfaces undergo continuous and flexible deformations which is due to one or a combination of actuator settings and aerodynamic loads. Therefore, knowledge of the morphing control surface shape is of prime importance.

This chapter includes the implementation of the understanding from the morphing wing mock-up study (Chapter 6) and its recommendations to get optimum results. These include fibre position and layout, sensor selection, sensing methodology and the effect on the strain output due to the behaviour of the top and bottom sections of the wing. Overall, the multimodal sensing methodology is similar to the previous cases where fibre Bragg grating sensors were used to measure local strain as well as the displacement between any two sensors. Using the proposed hybrid sensing principle the morphing behaviour is estimated for different load alleviation cases. This chapter falls under the Complexity Level IV category where the morphing behaviour of the control surfaces of the full-scale wing are studied.

7.2. Collaboration and Contribution

As the work in this chapter was a joint collaboration with other members of the SmartX team, this section is dedicated to highlight their individual contributions. This is also done to avoid contribution repetitions in each section.

My research contribution in this work pertained to the design, development, implementation and demonstration of the multimodal shape sensing technology on the SmartX wing using fibre optic sensing. This included the analysis of the morphing sequences from the MLA tests and studying the actuator effectiveness during morphing.

SmartX members Tigran Mkhoyan, Vincent Stuber and Nisarg Thakrar were involved in the manufacturing of the hardware demonstrator. This included the layup of the optical fibres that were selectively chosen and manufactured to order by me. I provided the manufacturing team with an extensive fibre installation manual to help in the installation and the layup process. This manual included information on the fibre layout design and fibre selection for each morphing section based on the property of the FBGs, which was a critical step for my analysis. The morphing control logic and Manoeuvre Load Alleviation (MLA) tests were designed by Xuerui Wang along with Tigran Mkhoyan who designed the actuator setup and the slow morphing technology. They also aided in the morphing control for my fibre optic

shape sensing calibration tests in the laboratory as well as the camber morphing tests in the wind tunnel through different MLA cases. The manufacturing team along with Xuerui Wang and Iren Mkhoyan helped build the Open Jet Facility (OJF) external balance following which I installed my fibre optics related setup.

7.3. SmartX enabling technologies

The multi-objectives of the SmartX technology integrator (alternatively referred to as the hardware demonstrator) include drag reduction in cruise, load control, aeroelastic stability control and lift control. To achieve these, four enabling technologies were established. They are: slow morphing, fast morphing, shape sensing and boundary layer sensing.

In this chapter, two of the aforementioned technologies, viz., slow morphing and shape sensing are utilised. Hence, only these two are elaborated further as they are required to understand the work. Additional information on the SmartX project philosophy, its enabling technologies and technology integration can be found in detail in the SmartX overview paper [2] which is a joint collaboration of the SmartX team.

7.3.1. Slow morphing concept

The SmartX slow morphing concept considers cambers and twists in the trailing edge of the wing in a frequency bandwidth of typically 0.1 Hz to 1 Hz. It is based on the Translation Induced Camber (TRIC) concept that was developed at the Delft University of Technology [3]. The TRIC concept is a chordwise seamless morphing concept that exhibits large deformations and associated driving force, but, although being seamless, does not introduce locally large strains in the structure. This enables the use of off-the-shelf aerospace materials, which makes the morphing concept feasible and scalable for a wide range of aircraft classes.

The basic idea behind the TRIC concept is that the closed-cell of a control surface is cut to reduce its torsional stiffness. The cut that was introduced is closed using a linear actuator. Therefore, the control surface can be moved without virtually any resistance from the skin whilst the actuator is moving, but the control surface closed-cell obtains the actuator stiffness once the actuator is locked. The idea behind the concept is shown in Figure 7.1. The slot in which the trailing edge skin can move in the chordwise direction can be observed. The relative motion of the trailing edge skin in the chordwise direction is ensured by the integrated linear actuator, which is located inside the wing box. Each morphing flap (hereon referred to as module) is equipped with two actuators located at either side in the spanwise direction. The actuators are selected for their high driving force and position feedback capabilities, counting to 12 in total for all six modules [2].

The SmartX hardware technology integrator is equipped with six trailing edge modules that contain the TRIC concept. These trailing edge TRIC modules cover the entire span of the wing and are equally spaced. The gap between each of the

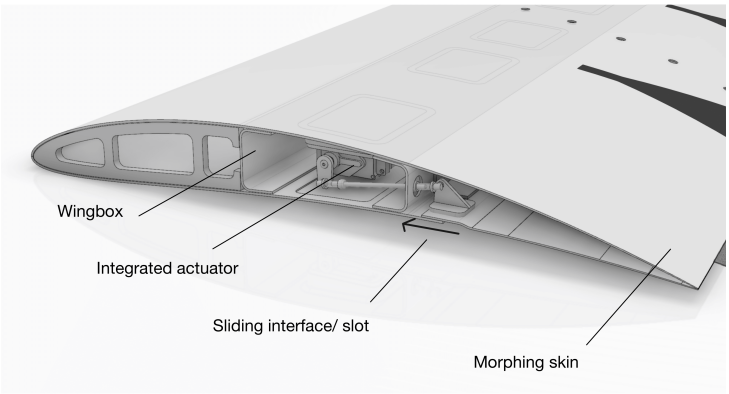

Figure 7.1: SmartX slow morphing concept: the trailing edge can seamlessly move up and down [2].

individual modules is closed using a flexible elastomeric material to make the wing trailing edge entirely seamless both in chordwise (due to the morphing concept) and spanwise (due to the silicone material) directions. The flexible elastomeric skin has been optimised such that a balance is found between the desired tip flexibility and required actuator loads.

Within the intended bandwidth up to 1 Hz, the slow morphing concept can exhibit peak-to-peak trailing edge deflections up to 16 mm upwards and 14 mm downwards and deliver a driving force which is in the order of the applied loads that can be expected on a wing of the size of the SmartX hardware technology integrator.

Variable skin stiffness in the form of skin thickness tailoring ensures that the trailing edge skin is sufficiently stiff to support the aerodynamic loads whilst it is flexible enough to allow the required deformations. The variable skin thickness is made possible by making use of ply drops of a composite skin. This is needed to obtain a smooth outer surface whilst matching a prescribed target shape for the control surface. A fluid-structure interaction routine was used to determine the most optimal ply dropping sequence. More details about this procedure can be found in [4]. The result of the optimisation can be seen in Figure 7.2 for a single slow morphing module.

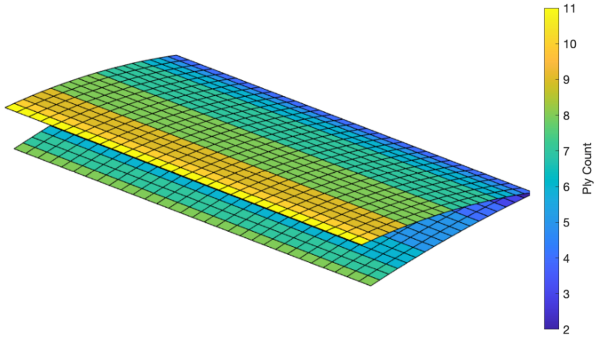

Figure 7.2: TRIC skin ply drop pattern (one layer has a thickness of 0.12 mm) [2].

7.3.2. Fibre optic shape sensing

Wing shape changes influence the aerodynamics and are also considered as a source of load acting on the wing. For load alleviation purposes and closed-loop control, shape sensing and wing deformation monitoring are necessary.

The wing contains a total of 14 optical fibres. Figure 7.3 shows the layout of the fibres that are bonded onto the skin and connected to the fibre connector hub. This layout was chosen by me based on the findings and understanding from the previous technical chapters. Doing so, capturing of the morphing behaviour including bending and torsion would be possible. The six independent morphing modules and the wingspan structure contain two fibres each, one on the upper surface and one on the lower surface.

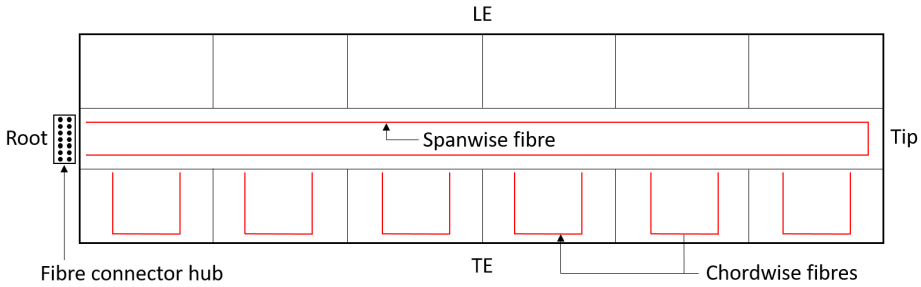

Figure 7.3: Layout of the spanwise and chordwise optical fibres (in red) on the SmartX wing. Connections to the 14 fibres are through the fibre connector hub.

7.4. Morphing control logic

Aircraft structural loads can be amplified significantly during sharp manoeuvres, which can lead to structural fatigue and even local structural damage. Therefore, it is crucial to alleviate aircraft structural loads during manoeuvre [5]. In the literature, a wide variety of control methods have been implemented for aircraft Manoeuvre Load Alleviation (MLA) purposes [6–8] and are known to have limitations [9]. On the other hand, the novel Incremental Nonlinear Dynamic Inversion (INDI) control overcomes these limitations by simultaneously reducing its model dependency and enhancing its robustness against model uncertainties and external disturbances [10]. These features make it promising for aircraft load alleviation problems [11]. In this study, the MLA control law is executed by distributed wing trailing-edge morphing surfaces. To accurately know the morphing control effectiveness, it is important to sense the morphing surface deformations in real-time.

The active morphing function of the SmartX-Alpha enables it to achieve control objectives in a seamless way. To guarantee the aerodynamic effectiveness of the morphing surfaces, it is very important to monitor and know the actual morphed shape and deformations of the control modules. The multimodal fibre optic sensing approach is perfect to achieve this goal because of its capability of monitoring bending and torsional deformations, whilst at the same time, using least number of sensors. The shape sensing and morphing control method used compliment each other to achieve one of the objectives for the SmartX-Alpha wing, which is to simultaneously alleviate gust and manoeuvre loads. In this study, the incremental nonlinear dynamic inversion with quadratic programming control allocation and virtual shape functions (INDI-QP-V) is proposed to reach this objective [12].

7.4.1. Manoeuvre Load Alleviation

The wing root shear force F_y and bending moment M_x are two important load indicators (plotted in Figure 7.4) for MLA. Their values can be measured by an external balance in real-time. The wing load alleviation is achieved by tracking the load references using INDI-QP-V. For example, in a symmetrical pull-up manoeuvre, the wing root shear force F_y should be increased to amplify the load factor. If the manoeuvre load alleviation is not performed, then the wing root bending moment M_x would also been amplified. By contrast, the spanwise lift distribution can be modified by the trailing-edge control surfaces, which makes it possible to increase the total lift without amplifying the bending loads. To be specific, in a symmetrical pull-up manoeuvre case, the outboard surfaces should morph up to reduce lift, whilst the inboard surfaces should morph down to increase lift. As a result, the wing aerodynamic centre is shifted inboard for alleviating manoeuvre loads. The spanwise lift-redistribution can also be used for alleviating wing loads during sharp roll. Keeping this in mind, three MLA cases were experimented with. They are $(F_y;M_x)$ = (20;0), (25;0) and (30;0).

7.5. SmartX hardware demonstrator

The test specimen was a carbon fibre composite (CFRP) morphing wing demonstrator manufactured as part of the SmartX project. The geometric properties of the wing are as shown in Table 7.1. The wing had a NACA 6510 profile, a span of 1800 mm and a chord of 500 mm giving it an aspect ratio of 7.2. It featured 6 independent morphing trailing edge sections with optical fibres running through each of them. These sections were allowed to deflect up to a maximum of +30/-20 mm, whilst allowing a rotation of 40° at the root of the trailing edge. The wing sat vertically on a root balance platform with the leading edge facing the incoming airflow.

Table 7.1: Material and geometric properties of the wing.

Property	Variable	Value
Material		Carbon fibre
Chord (wing)	c_w	500 mm
Span (wing)	s_w	1800 mm
Chord (module)	c_m	300 mm
Span (module)	s_m	300 mm
Thickness	t	Varying based on ply of 0.12 mm

The dimensions of the wing were chosen such that it would fit into the Open Jet Facility (OJF) wind tunnel of the Delft University of Technology, which has a square cross-section of 2850 mm x 2850 mm. The design loads for the wing were determined by the maximum flow velocity of the OJF of 35 m/s. More details about the wind tunnel model design can be found in [4].

7.5.1. Setup

The experiments for this study took place in the Open Jet Facility (OJF), a low speed wind tunnel at TU Delft's Aerospace Engineering faculty. Figure 7.4 shows the complete setup in the OJF, including the test specimen, the two optical fibre measurement systems, the optical switch, and the data acquisition system.

Each of the optical fibres contained fibre Bragg grating (FBG) sensors at pre determined positions (more details in Section 7.5.3). A spectral FBG interrogator (National Instruments, PXIe-4844) with 4 pm resolution, 4 pm accuracy, 40 dB dynamic range, and a wavelength range from 1510 nm to 1590 nm measured the local strain at each of these FBGs. Secondly, an FBG-Pair interrogator (Optics11, ZonaSens) with 1 pm resolution, 10 nm accuracy, 160 dB dynamic range and a wavelength range from 1530 nm to 1560 nm measured the displacement between two given FBGs. In order to avoid vague readings due to both the systems interrogating the same fibre simultaneously, an optical switch (Thorlabs, OSW22-1310E) was used. All the fibres from the wing are connected to the measurement systems through the connector hub (shown in Figures 7.3 and 7.7) present at the wing root.

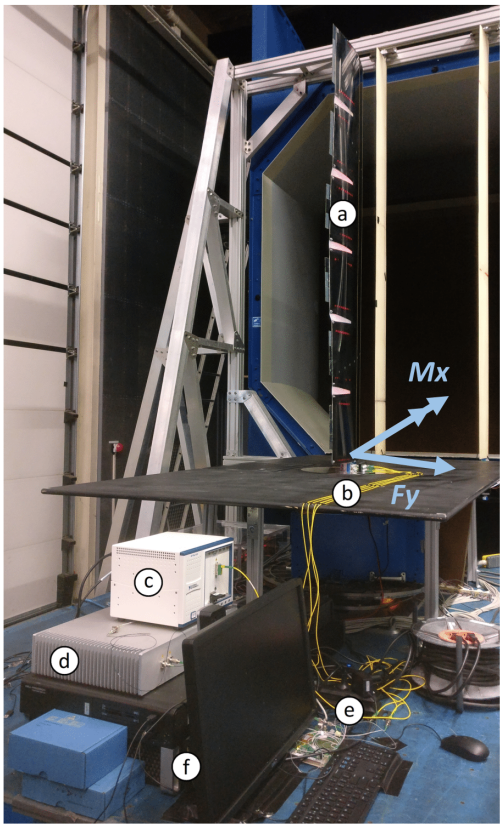

Figure 7.4: The experimental setup for shape sensing at the OJF (Open Jet Facility) low speed wind tunnel, showing the (a) wing, (b) optical fibres (yellow), (c) National Instruments interrogator, (d) Optics11 interrogator, (e) Thorlabs optical switch, and the (f) Data acquisition (DAQ) system.

Figure 7.5 gives a brief overview of the experimental workflow. The controller provides an input command that brings about appropriate actuator movements in the modules. This causes a morphing sequence to occur and the actuator position feedback is recorded. Simultaneously, the deflection of the module is calculated and recorded through the output of the FBG and FBG-Pair sensor measurements. Finally, the real morphing deformations are evaluated by comparison.

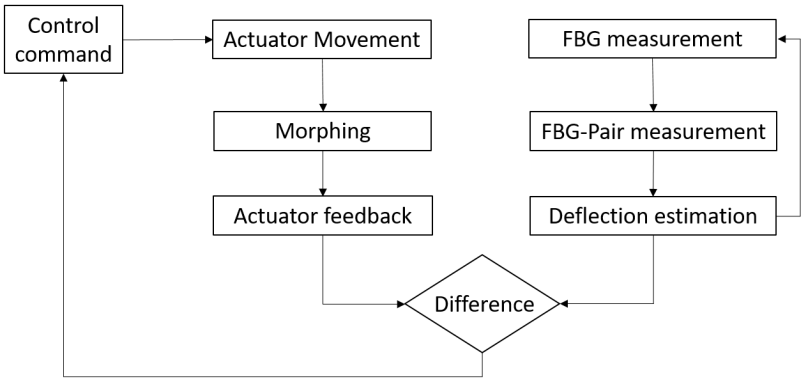

Figure 7.5: Block diagram depicting the sequential workflow of the experiment.

7.5.2. Actuator Setup

Each of the 6 trailing edge modules had actuators at each end that control the morphing behaviour. The concept of this morphing mechanism involves the upper surface of the module to be fixed and the lower surface to move with the help of actuators [3, 4, 13]. The actuators controlling the morphing movement were continuous torque servos (Volz DA 22-12-4112) designed for high continuous loads aimed for fixed-wing applications. The cut-off frequency of the actuators was $\approx$ 2.6 Hz (16.3 rad/s), and they allowed an actuator peak-to-peak amplitude of 25° [2].

Figure 7.6 is a CAD render of the wing and the actuation setup for morphing. The upper surface of the module (Figure 7.7) seamlessly connected to the wing box, whilst the lower surface (Figure 7.8) was left free, allowing it to slide in and out of a sliding surface/slot. The actuator arms were attached to this lower surface. Controlled activation of the individual actuators and, hence, the sliding motion of the lower surface subjects the module to bending and/or torsion. The actuator arm pulled towards the wing box caused a negative deflection of the trailing edge, and vice versa. All the six morphing modules of the wing functioned in the same way. The measurements in this study pertain to module #1 and module #6. These are the morphing modules at the wing root and tip, respectively (i.e., the bottom-most and top-most modules in Figure 7.4).

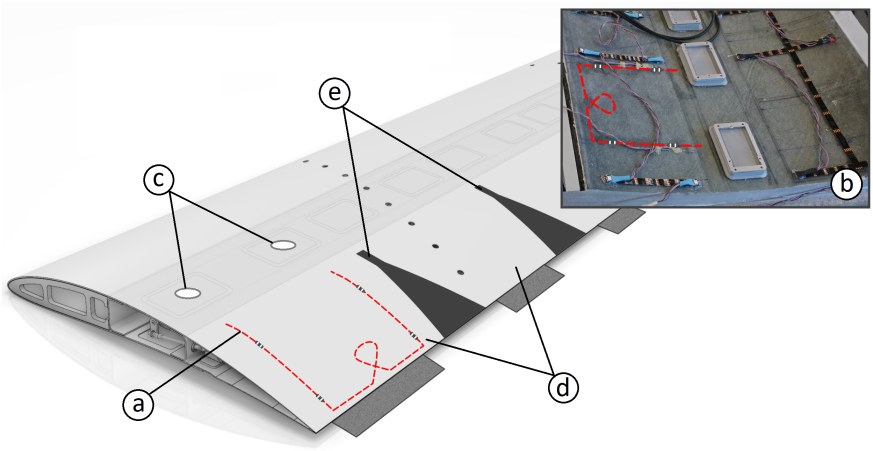

Figure 7.6: Overview of the wing showing the (a) fibre on module #1 and (b) internal view. The (c) actuator setup morphs the (d) seamless morphing modules that are connected through (e) flexible intermodular elastomeric skins [4].

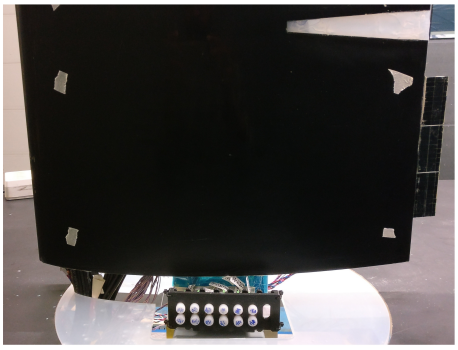

Figure 7.7: Zoomed-in images of module #1 of the test wing showing the module's upper surface (fixed) along with the optical fibre connector hub at its bottom.

Figure 7.8: Zoomed-in images of module #1 of the test wing showing the module's lower surface (sliding).

7.5.3. Sensor layout design

The layout of the optical fibres and the FBG sensor placement was followed based on the recommendations from the findings [13, 14] from the earlier chapters (Chapters 5 and 6).

Figure 7.9 shows an illustration of the fibre layout (in red) and FBG location on the upper (inner) surface of the morphing modules. For better understanding, the illustration can be considered as a superimposition of the FBG layout on Figure 7.7. This configuration has a total of 4 FBG sensors, which are marked as $S1$ to $S4$ along the fibre.

The sensing fibre was bonded to the inner upper and lower surface skins. This was necessary so that the fibre does not disturb the air flow on the outside surface of the wing and to be inconspicuous. Due to the ply dropping sequence [4], the inner surface had to be sanded to ensure the fibres were bonded on a flat surface. Cyanoacrylate adhesive (R&G-Sekundenkleber Typ SF5) was used to bond the fibre in a U-shaped pattern. In this way, the gratings $S1$ and $S4$ were 30 mm from the wing box, and gratings $S2$ and $S3$ 50 mm from the trailing edge. All the gratings were oriented parallel to the wing chord. The distance between grating pairs $S1$-$S2$ and $S3$-$S4$ were the effective sensing lengths. The distance between the $S1$-$S2$ and $S3$-$S4$ fibres was 145 mm.

The measured local strain ε from the FBG sensors is denoted by their corresponding sensor numbers as ε_1 to ε_4. The measured optical distance is given by ΔL_{1-2} and ΔL_{3-4} for grating pairs $S1$-$S2$ and $S4$-$S3$, respectively.

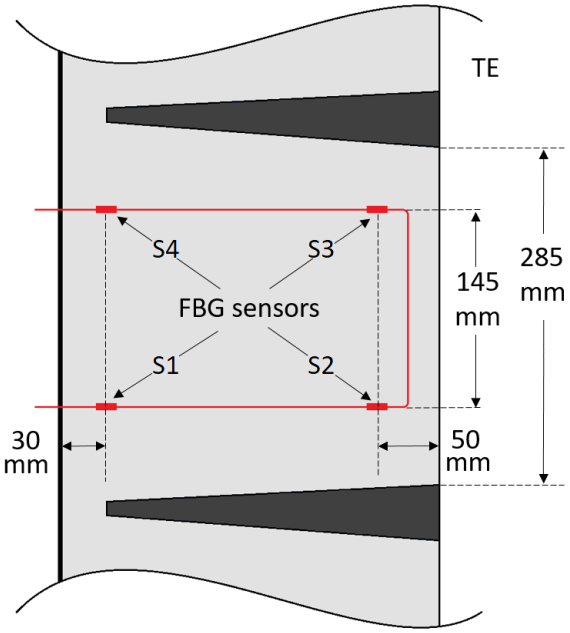

Figure 7.9: The U-shaped fibre layout (in red) on the upper (inner) surface of the morphing module. The location of FBG sensors ($S1$ to $S4$) along the fibre are as marked.

The optical fibre used was a standard single mode fibre (Corning ZBL SMF-28e) with an FC/APC connector. The properties of all the gratings in the fibre are mentioned in Table 7.2 and the sensors were manufactured by DK Photonics. The properties of the gratings were selectively defined to accommodate the capabilities of both the optical interrogators used. The gratings were each 3 mm long and operated in the 1530 nm to 1565 nm range (C-band). High reflection gratings were chosen (>84%) with bandwidths greater than 0.85 nm. The gratings had a temperature sensitivity of 10 pm/° C.

Property	S1	S2	S3	S4
Wavelength (nm)	1530.007	1540.016	1550.104	1559.992
Bandwidth (nm)	0.875	0.852	0.892	0.954
Reflectivity (%)	86.29	84.61	84.15	89.11
Temp. sensitivity		← 10 pm/°C →		

Table 7.2: Properties of the grating sensors S1, S2, S3 and S4 (DK Photonics).

7.6. Measurements

The measurement process incorporated here relies on the initial calibration of the morphing module outside the wind tunnel and camber morphing and deflection tests inside the wind tunnel.

7.6.1. Calibration

The calibration tests were carried out beforehand for the modules in the aircraft hangar outside the wind tunnel. The test setup for the calibration was similar to the setup elaborated in Section 7.5.1 and in Figure 7.4. Additionally, a standard vernier scale was used for measuring the module deflections. The calibration was done for upward, downward, and twist morphing configurations for different actuator positions. The positive and negative deflections of the module were distinguished by their polarity and were identified at the interrogator level. These measurements formed baseline data to develop an experimental-based-model that would later be used to estimate the deflections in the wind tunnel test. The algorithm depends on a transfer function that goes from measuring the strain output in the fibre due to the camber morphing to the trailing edge deflection. To achieve this, a relation between the raw *FBG* and *FBGP* data to the tip deflection was made.

7.6.2. Camber morphing - Wind tunnel tests

The camber morphing estimation was performed with the help of Manoeuvre Load Alleviation tests ((MLA); Section 7.4.1). This involved reading (both) the actuators and recording the strain and displacement data from the optical fibre system during morphing. The effectiveness of the system in monitoring the dynamic bending/twisting of the morphing module was determined for 3 test cases. This included continuous dynamic movements of the module for a run of 80 s each. The modules were deflected due to the input from their two respective actuators. A transfer function that related the tip deflection to the strain acquired from both the optical sensing methods was applied individually to both these actuators. This deflection was then correlated to the predicted servo angles.

The methodology used follows the steps developed and elaborated in Chapter 6, Section 6.3.4. A camber-morphing → sensing-fibre-strain → trailing-edge-deflection type transfer function was used to correlate the measurement data with the trailing edge deflection.

The following was observed from the calibration and baseline measurement tests. In the event of pure upward (and downward) bending, ε_2 and ε_3 *FBG* readings and ΔL_{1-2} and ΔL_{3-4} *FBGP* readings alone were required to identify these changes. On the other hand, when twist was considered, the measurements ε_1 and ε_4 that were not utilised in the bending case were involved and were necessary to identify the twisting behaviour. Having different functions for different (pre-known) morphing configurations is acceptable when static tests are considered where different test cases could be isolated and estimated. But, in case of a dynamic test (in the wind tunnel) a system that could involve and read all morphing cases was required.

This led to a preference to have separate transfer functions for both the actuators which could be applied for all morphing configurations simultaneously to have dynamic measurements. Additionally, this also gave the benefit to detect right and left tip deflections separately which could be related to the individual actuators at each end of the module. Therefore, combining all the sensor readings, the estimation was done following Equation 6.2 for right tip deflection (δ_r) and Equation 6.3 for left tip deflection (δ_l).

7.6.3. Manoeuvre Load Alleviation

To implement MLA for the SmartX-Alpha wing, the wing root shear forces and moments were measured by the OJF External Balance at 1000 Hz [12]. The core component of the balance is a set of strain gauges, which can be attached to real-world operational aircraft wing structures. The measurements were filtered by second-order low-pass filters with a damping ratio 0.8, and a circular frequency of 10 rad/s. The number of servos m is 12. The order of virtual shape functions were selected as $q = 5$. The position limit of the servos equalled 30°, whilst their rate limit equalled 80°/s. Regarding adjacent servos, if there was an elastomer between them, then their relative motions were constrained within 10°. Otherwise, this value was relaxed to 55°. The servos were connected to a single RS-485 device, and their positions were fed back to the control computation in 66.7 Hz [12]. The transport delay was approximately 15 ms. The system identification results showed that the servo dynamics can be modelled by second-order low-pass filters with damping ratio 0.71 and circular frequency 16.52 rad/s.

7.7. Results

Following the procedure explained in section 7.6, experiments were performed on the SmartX morphing wing modules involving varying load indicators F_y and M_x with the intention of alleviating gust and manoeuvre loads. Significant movements of the modules due to the morphing sequences were detected using the strain and displacement outputs of the fibre sensors. Figures 7.10 to 7.12 show the servo positions compared with the estimated positions from the FOS (Fibre Optic Sensor) measurements for module #1. Likewise, Figures 7.13 to 7.15 are for module #6. The positive and negative servo angles suggest that the surface of the module morphs downwards to increase lift and upwards to decrease lift, respectively (refer section 7.4.1).

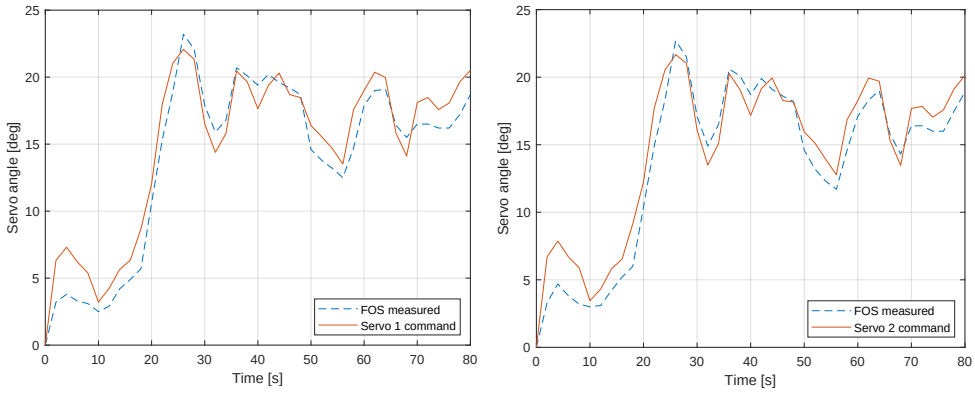

(a) (b)

Figure 7.10: Estimated position with respect to module #1 deflections for the F_y = 20 and M_x = 0 case. The morphing sequence begins at ~15 s. The positions of actuators 1 and 2 are separated and shown in figures a and b, respectively.

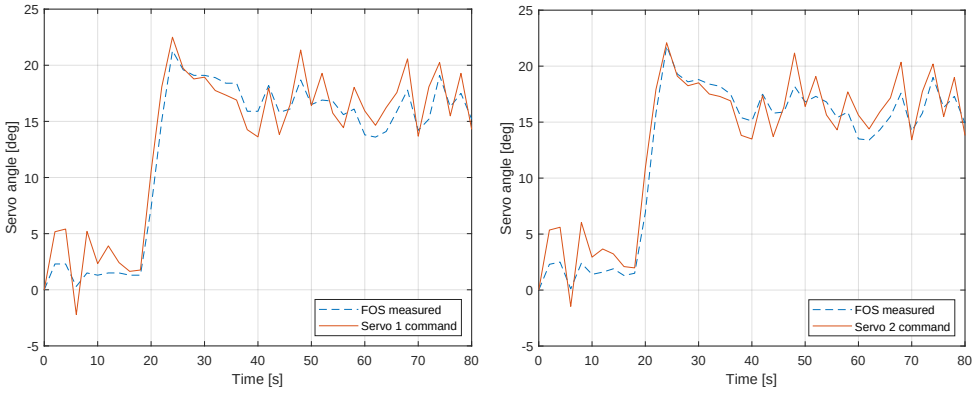

(a) (b)

Figure 7.11: Estimated position with respect to module #1 deflections for the F_y = 25 and M_x = 0 case. The morphing sequence begins at ~15 s. The positions of actuators 1 and 2 are separated and shown in figures a and b, respectively.

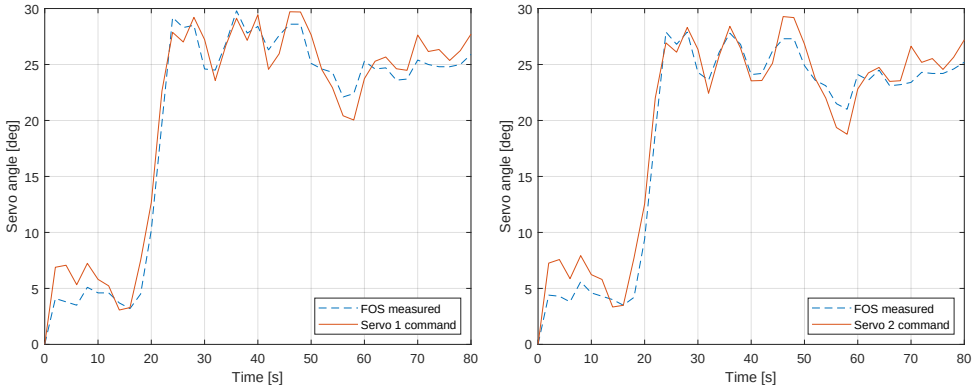

(a) (b)

Figure 7.12: Estimated position with respect to module #1 deflections for the F_y = 30 and M_x = 0 case. The morphing sequence begins at ~15 s. The positions of actuators 1 and 2 are separated and shown in figures a and b, respectively.

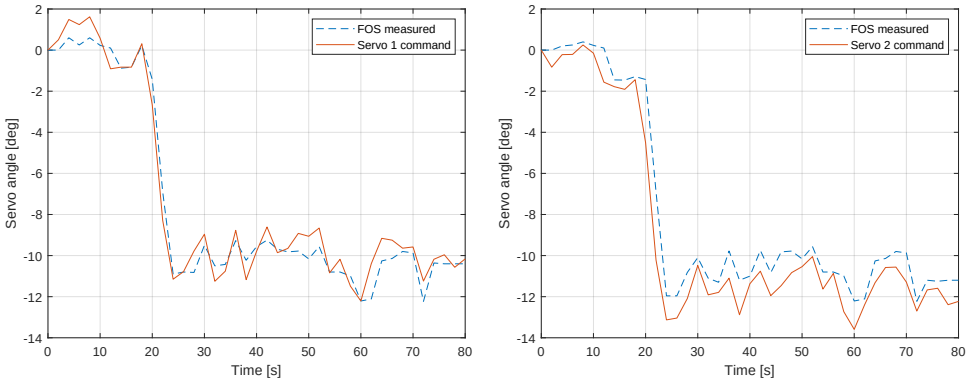

(a) (b)

Figure 7.13: Estimated position with respect to module #6 deflections for the F_y = 20 and M_x = 0 case. The morphing sequence begins at ~15 s. The positions of actuators 1 and 2 are separated and shown in figures a and b, respectively.

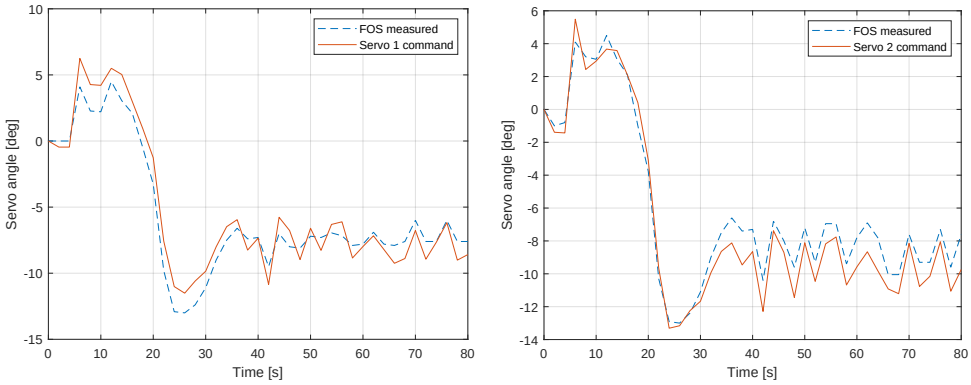

(a) (b)

Figure 7.14: Estimated position with respect to module #6 deflections for the F_y = 25 and M_x = 0 case. The morphing sequence begins at ~15 s. The positions of actuators 1 and 2 are separated and shown in figures a and b, respectively.

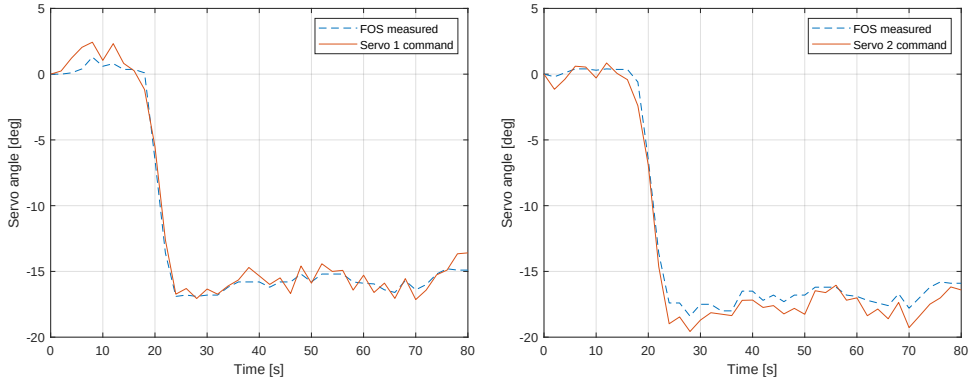

(a) (b)

Figure 7.15: Estimated position with respect to module #6 deflections for the F_y = 30 and M_x = 0 case. The morphing sequence begins at ~15 s. The positions of actuators 1 and 2 are separated and shown in figures a and b, respectively.

Overall, the estimation coincides and follows the trend for all the six cases (Figures 7.10 - 7.15). Initially until ~15 s the module is left free, and no servo commands are given. The morphing sequence starts thereafter. The mismatch is seen to be within 3 mm for the position estimation. This mismatch is better depicted through Figure 7.16, where the diagonal line represents a 1:1 estimation in degrees between the servo commands and the FOS measurements. The points are seen to be scattered within +3° to -3° from this diagonal. Additionally, since the movement range of the module is mostly from 13° to 30°, there are few measurement points below 13°.

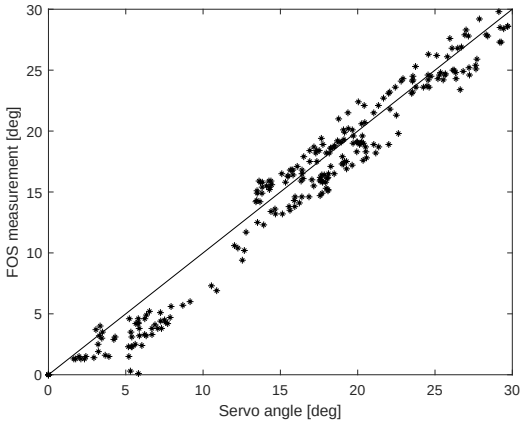

Figure 7.16: The mismatch in estimation between the servo command and the fibre optic sensor (FOS) measurement in degrees.

When the servo angle variations are small, there is very little morphing taking place. This is more prominent when the servo changes directions throughout the test run. This effect is noticed in Figure 7.11, starting from the 40 s mark, and more prominently throughout Figure 7.15.

7.8. Discussion

The inaccuracies in the fibres/sensors, experimental setup and possible error sources that may directly or indirectly affect the measurements are discussed as follows. There are mainly three aspects that could lead to the mismatches between the servo angles and fibre sensed data: (1) servo dynamics and delays; (2) random error from measurements and calculation; (3) nonlinear mechanism backlash.

Regarding the first point, the servo command given by the control computer cannot be immediately executed by the servo. Experimental data shows that there was approximately 15 ms of transport delay, which was sufficiently small when compared to the data rate of the optical interrogators. Moreover, the Volz DA 22-12-4112 servo used by the SmartX-Alpha had a transfer function as $H(s) = \frac{\omega^2}{s^2+2\zeta\omega s+\omega^2}$,

where s is the Laplace variable, $\zeta = 0.71$, $\omega = 16.52$ rad/s. This further caused a frequency-dependent phase lag between the commanded and real servo angle.

The second, unpredictable change in the measured value, came from the random error in the measurement. The random error in the experiment is significant as compared to the offset and/or scale factor errors. This is because an initial calibration procedure was done that removes the systematic errors. To account for the random errors, the error was quantified experimentally based on static deflection tests for different morphing sequences. The measured standard deviation for the quantities ε_1 and ε_4 was <0.05, and, for ΔL_{1-2} and ΔL_{3-4}, was <0.1. This measurement accuracy caused a variation of ± 1 mm in the transfer functions δ_l and δ_r.

Last but not least, mismatches were contributed by the nonlinear backlash in the morphing mechanisms. Backlash is a clearance phenomenon in mechanical systems caused by gaps between the parts. The present SmartX-Alpha wing involves largely handcrafted structural components and manual laminate layup, which inevitably lead to manufacturing imperfections, including the tolerance between the bottom skin and the sliding interface. As a result, whenever the servo command changed directions, the pick-up point needed to rotate, and the bottom skin needed to bend, before the ideal translational sliding actually happened [12]. This nonlinear backlash phenomenon caused hysteresis effects in both the OJF external balance and the optical fibre measurements.

In Figure 7.17, the servos start from 30° and gradually reduce to -30°, and then increase back to 30°. It can be observed that owing to backlash, the same servo command leads to different wing root shear forces (F_y) in upstroke and downstroke. Experimental data show the backlash servo angle is approximately in the range of -2.5° to 2.5°. Backlash is one of the predominant inducements for the estimation errors.

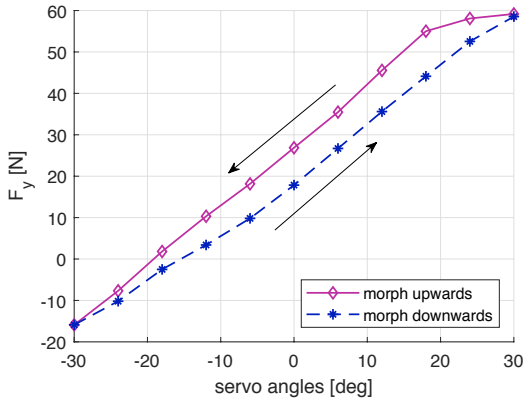

Figure 7.17: Experimental result for backlash-induced wing root shear force hysteresis loop [12].

7.9. Concluding remarks

This fourth technical chapter is of complexity level IV and presents the principles, design, and finally, the application of the multimodal fibre optic sensing approach for measuring the camber morphing of the SmartX hardware wing demonstrator. The wing was tested in the OJF low speed wind tunnel.

Wing shape changes influence the aerodynamics and are also considered as a source of load acting on the wing. For load alleviation purposes and closed-loop control, shape sensing and wing deformation monitoring are necessary. Morphing was chosen as the actuation concept instead of the use of conventional discrete control surfaces due to the aerodynamic efficiency as a result of seamless spanwise and chordwise morphing deformations.

This research has demonstrated the working of a multimodal optical fibre-based sensing method to predict the position of a wing camber morphing module in the wind tunnel. The effectiveness of the proposed sensing method in monitoring the morphing sequence was determined for three different Manoeuvre Load Alleviation (MLA) cases. These morphing sequences included: pure upward bending, pure downward bending, pure twist, and combined twist and bending. The morphing sequences were brought about by two servos at each end of the morphing modules.

A single core single-mode fibre containing four fibre Bragg gratings (FBG) was bonded to each module. Local strain measurements from each FBG and displacement measurements from each FBG pair were measured for each test. FBGs are known to be temperature sensitive. As the sensitivity within the wind tunnel was measured to be small enough (within $\pm 0.5°$), the temperature component was neglected in the final calculation.

A lucid explanation of the experimental measurement strategy is as follows. An appropriate servo command brings about a certain morphing sequence which results in a change in shape of the module. This change is picked up as strain by the FBG sensors and FBG sensor pairs in the bonded optical fibres. The algorithm then calculates the deflection of the module by estimating the position of the actuators using the baseline measurements as reference. This is done separately for each actuator to account for bending and/or twisting. It is to be noted that, due to hardware limitations, a truly real-time measurement was not achieved. This was attributed to limitations including unequal sampling speeds between the interrogators, longer switching (and calibration) time between the fibres and incapability of interrogating multiple fibres (and FBGs) simultaneously. Although important, this did not have an effect on the study as the prime requirement was to demonstrate the working of the principle and its application on a composite full-scale morphing wing in the wind tunnel.

The ability of the proposed method to estimate the deflections of the morphing module when subjected to a bending and/or twist proves its potential for shape monitoring of morphing structures. The study proposed here extends the two-dimensional idealization of a wing flap through a cantilever plate [14] and a morphing wing mockup study [13]. This work also shows that the deflection estimation can be easily achieved by using just four FBG sensors in a single fibre. The sources of inaccuracies and errors are identified, and the estimated measurements were

found to have within 10% error for trailing edge deflection estimation.

Finally, this study successfully concludes the initial shape sensing aim of the SmartX project including the monitoring of morphing aircraft structures. A novel multimodal fibre optic sensing approach was proposed and its feasibility as a shape sensing tool was successfully tested on the demonstrator in the wind tunnel.

References

[1] **N. Nazeer**, X. Wang, and R. M. Groves. "Sensing, Actuation, and Control of the SmartX Prototype Morphing Wing in the Wind Tunnel". In: *Actuators* 10.6 (2021). doi: 10.3390/act10060107.

[2] R. D. Breuker, T. Mkhoyan, **N. Nazeer**, V. Stuber, R. M. Groves, S. van der Zwaag, and J. Sodja. "Overview of the SmartX wing technology integrator". In: *Journal of Aircraft* (2022). Manuscript submitted for publication.

[3] N. Werter, J. Sodja, G. Spirlet, and R. de Breuker. "Design and Experiments of a Warp Induced Camber and Twist Morphing Leading and Trailing Edge Device". In: *24th AIAA/AHS Adaptive Structures Conference* (2016), pp. 1–20. doi: 10.2514/6.2016-0315.

[4] T. Mkhoyan, N. R. Thakrar, R. De Breuker, and J. Sodja. "Design of a Smart Morphing Wing Using Integrated and Distributed Trailing Edge Camber Morphing". In: *ASME 2020 Conference on Smart Materials, Adaptive Structures and Intelligent Systems*. American Society of Mechanical Engineers Digital Collection. 2020.

[5] M. de Virgilio Pereira, I. Kolmanovsky, C. E. Cesnik, and F. Vetrano. "Model Predictive Control Architectures for Maneuver Load Alleviation in Very Flexible Aircraft". In: *AIAA Scitech 2019 Forum*. January. San Diego, California: American Institute of Aeronautics and Astronautics, 2019. doi: 10.2514/6.2019-1591.

[6] Y. Ferrier, N. T. Nguyen, E. Ting, D. Chaparro, X. Wang, C. C. de Visser, and Q. P. Chu. "Active Gust Load Alleviation of High-Aspect Ratio Flexible Wing Aircraft". In: *2018 AIAA Guidance, Navigation, and Control Conference*. January. Kissimmee, Florida: American Institute of Aeronautics and Astronautics, 2018, pp. 1–36. isbn: 978-1-62410-526-5. doi: 10.2514/6.2018-0620.

[7] M. Pereira, de F. V., I. Kolmanovsky, C. E. S. Cesnik, and F. Vetrano. "Model Predictive Control for Maneuver Load Alleviation in Flexible Airliners". In: vol. 16. 1. Savannah, Georgia: International Forum on Aeroelasticity and Structural Dynamics - IFASD 2019, 2019, pp. 420–432.

[8] Y. Bi, C. Xie, C. An, and C. Yang. "Gust load alleviation wind tunnel tests of a large-aspect-ratio flexible wing with piezoelectric control". In: *Chinese Journal of Aeronautics* December (2016). issn: 10009361. doi: 10.1016/j.cja.2016.12.028.

[9] W. J. Rugh. "Analytical framework for gain scheduling". In: *IEEE Control Systems Magazine* 11.1 (1991), pp. 79–84. doi: 10.1109/37.103361.

[10] X. Wang, E. van Kampen, Q. Chu, and P. Lu. "Stability Analysis for Incremental Nonlinear Dynamic Inversion Control". In: *Journal of Guidance, Control, and Dynamics* 42.5 (May 2019), pp. 1116–1129. issn: 0731-5090. doi: 10.2514/1.G003791.

[11] X. Wang, E. van Kampen, Q. P. Chu, and R. De Breuker. "Flexible Aircraft Gust Load Alleviation with Incremental Nonlinear Dynamic Inversion". In: *Journal of Guidance, Control, and Dynamics* 42.7 (July 2019), pp. 1519–1536. issn: 0731-5090. doi: 10.2514/1.G003980. url: https://arc.aiaa.org/doi/10.2514/1.G003980.

[12] X. Wang, T. Mkhoyan, I. Mkhoyan, and R. De Breuker. "Seamless Active Morphing Wing Simultaneous Gust and Maneuver Load Alleviation". In: *Journal of Guidance, Control, and Dynamics* (2021), pp. 1–14.

[13] **N. Nazeer**, R. M. Groves, and R. Benedictus. "Assessment of the Measurement Performance of the Multimodal Fibre Optic Shape Sensing Configuration for a Morphing Wing Mockup". In: *Sensors* 22.6 (2022). doi: 10.3390/s22062210.

[14] **N. Nazeer** and R. M. Groves. "Load Monitoring of a Cantilever Plate by a Novel Multi-modal Fibre Optic Sensing Configuration". In: *SN Appl. Sci.* 3.667 (2021). doi: 10.1007/s42452-021-04663-9.

8

Conclusions

If you have knowledge,
let others light their candles in it.

Margaret Fuller

This chapter wraps up the thesis by summarising its key take-away points. The Research Questions are revisited and the work carried out to address them is outlined. The main findings are mentioned for each of the Research Questions followed by recommendations for improvement that also span to applications outside aerospace. A section is also dedicated towards ideas on follow-up work and possible future areas of research interest using optical fibre sensors for monitoring purposes.

8.1. Scope of the thesis

The aerospace industry is an ever-evolving field and has seen many technological advances over the past decades. The desire for aircraft to be not only efficient and reliable but also cheaper and safer has brought about many proposals across the industry. This push has seen new designs, materials and maintenance methods. One of these advances is towards morphing aircraft wings to make wings lighter, more flexible, aerodynamically efficient and structurally stable. One of the key elements of a morphing wing are the sensors that monitor the shape on the wing throughout the flight. The design and development of smart sensing methods is required. The research in this thesis under the project SmartX aimed to address this need and work towards the design and development of smart sensing methodologies for shape sensing and load monitoring of morphing aircraft wings.

Knowledge of the wing and morphing control surfaces shape is needed to obtain the exact control settings for closed-loop control purposes. Morphing control surfaces exhibit a continuous and flexible deformation which is influenced by the actuator setting, the aerodynamic loads and the deflection of the neighbouring seamless control surfaces. Therefore, knowledge about both the transient and steady-state wing and morphing control surface shapes is necessary.

This thesis was focussed towards the the design and development of a Structural Health Monitoring (SHM) tool for adaptive aerospace structures and at the same time to reduce the dependency on high number of sensors. Fibre Optic Sensors (FOS) were chosen as the preferred sensing technology for this work. Compared to other sensors, fibre optic based sensors are advantageous because of their properties including high sensitivity, lightweight, capability of having multiple sensing points in a single fibre, flexible and ability to operate in harsh environments [1].

8

8.2. Research process

Within the already available fibre optic techniques an identification was made for the potential of a higher performing SHM tool. A proposal was made to have a reliable, robust and cost effective sensing methodology for real time monitoring of morphing structures with a simultaneous focus on the SmartX morphing wing demonstrator. Secondary and sub-research questions were framed to address each aspect of the principle research question.

An essential step at the beginning of this work was to have a Principle Research Question (PRQ) followed by a list of secondary Research Questions (RQ). These questions were established based on the background knowledge and the research gaps taken from the literature review.

The PRQ and RQs established were, reproduced from Section 3.2, as follows:

PRQ How can a reliable and robust sensing system be developed for multi-functional real-time monitoring of adaptive aerospace structures that is economical and

does not require processing of large amount of data?

RQ1 How can a sensing technology be chosen that is unobtrusive and be permanently fixed to reliably measure the load and shape of a morphing wing?

RQ2 How can the hybrid sensing methodology be used for multi-axis monitoring including the estimation of position and magnitude of an arbitrary load?

RQ3 How can the hybrid sensing methodology be used for deflection monitoring of complex morphing structures that cannot be easily modelled.

RQ4 How can the fibre optic sensing methodology be integrated and function in the SmartX morphing wing demonstrator?

The research process was guided with steps of increasing complexity to ensure stepwise development and understanding. A structured workflow was adopted by dividing the thesis into four technical chapters that take the reader through a stepwise increment in complexity. Table 3.1 explained the alignment of the RQs with the technical chapters of the thesis and further with the complexity levels for a structured flow. Instead of jumping directly to morphing wing structures, the study aimed to first establish a good foundation of the novel fibre optic sensing methodology and further build over it. This approach should help the reader in understanding better the development of a robust and reliable SHM tool for different applications.

8.3. Key points

Refering to the RQs established, the work was split into four sub-studies. They were focussed on the feasibility study of the proposed multimodal sensing approach and its validation, demonstration of 1 and 2 dimensional sensing involving the estimation of unknown loading position and magnitude, demonstration on a complex morphing mechanism to estimate the shape whilst morphing and lastly, the estimation of the shape of a 1.8 m wing in the wind tunnel along with studying the actuator effectiveness whilst morphing.

Feasibility study

This pertains to RQ1. The first step was to investigate and validate the feasibility of the proposed multimodal fibre optic sensing method and is elaborated in Chapter 4. This was carried out on an aluminium strip and a cantilever beam. Demonstration of 1 dimensional sensing was done by estimating the position and magnitude of arbitrary loads on the beam [2]. Analytical models for cantilever bending are well known and were used to validate the estimated results. The method was shown to be independent of the material properties and opened up the possibility of having a varying geometry but within predefined limits. The importance of having an initial calibration step for baseline measurements was emphasised. This step formed the basis for understanding the sensing method and its capabilities.

Loading position and magnitude

This pertains to RQ2. The next step was focussed on moving to more realistic (sized) structures and is elaborated in Chapter 5. A large cantilever plate was investigated to demonstrate the 2 dimensional sensing capabilities of the method [3]. The required dimension of the plate was initially cut from a larger sheet of aluminium and then drilled and bolted on one side to a support beam. This caused the plate to develop unevenness, curves and internal stresses. In order to capture these irregularities an experimental based model was used for verification. The position and magnitude estimation was done for arbitrary loads that caused the plate to undergo bending and twisting.

Shape estimation

This pertains to RQ3. On successfully demonstrating the capability of the method to estimate loading position and magnitude, the next step was to be able to determine the shape of the structure before and after the influence of (arbitrary) external loads. This is elaborated in Chapter 6. The final aim was to monitor a full scale morphing wing. A self-contained mock-up morphing wing section was manufactured and set up on a test bench. This also helped in understanding the morphing mechanism and in giving recommendations on the sensing fibre placement and sensor location [4]. The importance of initial calibration was also pointed out. The proposed method was able to estimate the initial and final shape of the wing and monitoring its deflections.

Actuator effectiveness

This pertains to RQ4. The final step of the thesis was to apply the findings from the previous steps for monitoring a full scale composite morphing wing and is elaborated in Chapter 7. This was done in the wind tunnel to simulate real-world conditions and took into account the implementation of the recommendations from the earlier study to get optimum results. These included fibre position and layout, sensor selection, sensing methodology and the effect on the strain output due to the behaviour of the top and bottom sections of the wing. The potential for shape monitoring of morphing structures was demonstrated with the ability of the proposed method to estimate the deflections of the morphing modules when subjected to different load alleviation tests [5]. Additionally, the sensing method was able to identify and quantify the issue of backlash in the system which added to its capability as a morphing monitoring tool.

8.4. Future work and ideas

The study was constrained towards thin structures where the thickness was negligible compared to the other dimensions. An interesting direction would be to study the effect of loading and deformation on thick structures. This would involve an extra factor of shear-effect that would have to be included in the estimation.

One direction that could be explored is the study of different fibre layouts. The case of strain along the grating length is primarily used in this study. Although the sensitivity is reduced (and negligible in an orthogonal orientation), gratings can pick up a portion of the strain that is not exactly along the grating. An optimisation study regarding the grating distribution could also be studied in efforts to reduce the number of gratings required.

Another improvement in the sensing model would be to have a closed loop system with sampling times on par with the controller requirements. This would help in a truly real-time and continuous monitoring that would be beneficial for the operators as well as for SHM information. Further, an interrogator capable of measuring all the fibres on the wing at once would reduce the delay in interrogation due to switching and recalibrating for different fibres.

Having a sensing fibre that could be attached to any morphing wing where it measures the structural and aerodynamic induced changes whilst measuring the real-time deformations would give rise to a master fibre. A by-product of having such a system would be to have a virtual representation of the wing and its behaviour that would serve as its real-time digital counterpart. In short, this information could contribute to the building of a digital twin system.

Another direction that could be explored is the development of an optical fibre based pressure sensor. The wing structure would require tiny negligible sized holes on the surface that could be used as pressure sensing points as shown in Figure 8.1. The fibre could also be simply bonded to the surface instead of having a gap and cavity points. Having an array of them in a particular pattern would also help in retrieving the aerodynamic load/pressure pattern on the wing. This could be done, for eg., either using a grating pair for each pressure point or long period gratings for the whole fibre that make use of evanescent wave sensing.

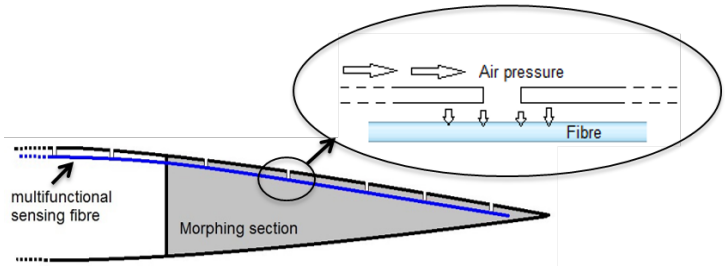

Figure 8.1: Idea for an unobstructive optical fibre pressure sensor.

Although the working of the monitoring tool was demonstrated in the wind tunnel, it would be ideal to conduct these tests on an actual flight. An alternative would be to begin with tests on Unmanned Aerial Vehicles (UAV) or scaled demonstrator wing models and then progress to commercial aircraft. It can be argued that the current commercial aircraft do not have morphing sections as shown in this thesis but the monitoring tool is not constrained to morphing sections. A simple example would be the capability of measuring the (spanwise) deflections and loads of the

wing which is basically a cantilever structure.

Moreover, it is vital to point out that the method developed and demonstrated in this thesis is not limited to aerospace (and morphing) structures and can be extended to other engineering structures. Load carrying structures that undergo deformations/deflections can be monitored provided they are properly calibrated. These include and are not limited to rotor blades, masts, beam structures and bridges.

List of Publications

Journals

4. R. D. Breuker, T. Mkhoyan, **N. Nazeer**, V. Stuber, R. M. Groves, S. van der Zwaag, and J. Sodja. "Overview of the SmartX wing technology integrator". In: *Journal of Aircraft* (2022). Manuscript submitted for publication

3. **N. Nazeer**, R. M. Groves, and R. Benedictus. "Assessment of the Measurement Performance of the Multimodal Fibre Optic Shape Sensing Configuration for a Morphing Wing Mockup". In: *Sensors* 22.6 (2022). doi: 10.3390/s22062210

2. **N. Nazeer**, X. Wang, and R. M. Groves. "Sensing, Actuation, and Control of the SmartX Prototype Morphing Wing in the Wind Tunnel". In: *Actuators* 10.6 (2021). doi: 10.3390/act10060107

1. **N. Nazeer** and R. M. Groves. "Load Monitoring of a Cantilever Plate by a Novel Multi-modal Fibre Optic Sensing Configuration". In: *SN Appl. Sci.* 3.667 (2021)

Conferences

3. T. Mkhoyan, V. L. Stuber, **N. Nazeer**, R. D. Breuker, R. M. Groves, W. A. Groen, S. van der Zwaag, J. Sodja, and X. Wang. "Multi-modal fibre optic shape sensing for the SmartX morphing wing demonstrator (PPT)". in: *Smart Materials, Adaptive Structures and Intelligent Systems, SMASIS 2020* Los Angeles, USA (2020)

2. **N. Nazeer**, R. M. Groves, and R. Benedictus. "Multi-modal fibre optic shape sensing for the SmartX morphing wing demonstrator (PPT)". in: *Smart Materials, Adaptive Structures and Intelligent Systems, SMASIS 2020* Los Angeles, USA (2020)

1. **N. Nazeer**, R. M. Groves, and R. Benedictus. "Simultaneous Position and Displacement Sensing Using Two Fibre Bragg Grating Sensors". In: *Proc. SPIE Smart Structures + Nondestructive Evaluation* 10970 (2019), 109701Z-1 –109701Z-8

National Review - NL

1. **N. Nazeer** and R. M. Groves. "Non-Destructive Evaluation - National Review - Netherlands". In: *International Committee on Aeronautical Fatigue and Structural Integrity* icaf.aero/index.php (2021)

Magazines

1. A. Rajabzadeh, **N. Nazeer**, L. Fazzi, and R. M. Groves. "Fiber optic sensing for aerospace structures". In: *PhotonicsNL* photonicsnl.org/ (2018)

Posters

6. **N. Nazeer** and R. M. Groves. "Shape Sensing of Morphing-wing Sections using Fibre Optic Sensors". In: *Precision Fair 10-11 November* Brabanthallen, 's-Hertogenbosch, NL (2021)

5. **N. Nazeer**. "SmartX Morphing Wing: Deflection Monitoring in the Wind Tunnel using Optical Fibre Sensors". In: *PhD Scientific Event 26 February* TU Delft, NL (2021)

4. **N. Nazeer**. "Development of a Fibre Optic Shape Monitoring System for a Morphing Wing Section". In: *PhD Poster Day 28 February: Graduate School AE* TU Delft, NL (2020)

3. **N. Nazeer** and R. M. Groves. "Development of a Fibre Optic Shape Monitoring system for a Morphing Wing Section". In: *Precision Fair 06-11 November* NH Conference Centre Koningshof, Veldhoven, NL (2019)

2. **N. Nazeer**. "Fibre Optic Shape Sensing for Monitoring of Aerospace Structures". In: *PhD Poster Day 08 March: Graduate School AE* TU Delft, NL (2019)

1. **N. Nazeer**. "Structural Health Monitoring of Adaptive Aerospace Structures". In: *PhD Poster Day 16 March: Graduate School AE* TU Delft, NL (2018)

Acknowledgements

First of all, I would like to thank my supervisor and promotor, Roger Groves, for believing in my potential and offering me a PhD position in his group. Roger - I'd like to recount one of our earlier meetings where you asked me to explore and find my way. You had mentioned that you would always have a birds-eye-view watching over me so that if or when I drifted too far away you'd slowly push me back on track. Thank you for giving me the freedom to explore and at the same time making sure I did not go astray. Your feedback over the years has helped me a lot. Thank you too for your understanding, motivation and support during the difficult times. I've always enjoyed (and will miss) our discussions in the office and in the lab. I take this opportunity to express my profound gratitude and deep regards.

I would like to extend my gratitude to my second promotor Rinze Benedictus. I vividly remember that moment when you gave me the thumbs-up from inside the room as I anxiously waited at the door after the Go/No-Go presentation. Thank you for your support and feedback throughout the PhD.

I'd also like to thank Henri Werij and Jacco Hoekstra for their advice, encouragement and support during the peak COVID times. Thank you too for the insightful discussions.

A big thank you goes to Gemma van der Windt for making sure everything from A to Z went smooth from even before the PhD began. I am grateful for your all-round support.

I'd also like to acknowledge and thank my second/back-up supervisor Roeland de Breuker who was also the lead for the SmartX project. Thank you too for your active support and feedback throughout the PhD.

Thank you to the rest of the SmartX team members - Tigran Mkhoyan, Vincent Stuber, Xuerui Wang, Jurij Sodja, Iren Mkhoyan, Nisarg Thakrar, Pim W.A. Groen and Sybrand van der Zwaag for each of their individual contributions that led to the success of the SmartX project. Thanks also to George Wijnschenk Dom for the discussions and help during the design phase of the SmartX wing.

Thanks goes out to all the technicians in the lab and the workshop for making sure all the equipment were in order and for making sure all my experiment related needs were met.

Thanks also goes to the service desk and ICT team for the support and for organising all my computer related needs.

To my committee members, Prof. dr. W. N. MacPherson, Prof. dr. K. A. Williams, Prof. dr. ir. H. L. Offerhaus, Prof. dr. F. Scarano, Prof. dr. F. C. T. van der Helm and Prof. C. A. Dransfeld, I'd like to thank you for accepting to be part of my doctoral committee and for your insightful comments and feedback on my thesis. I am grateful for your valuable time and effort invested towards this process.

Shout-out to those from NB. 0.38 who welcomed me when I first joined the office. Special thanks to Pedro, Nikos and Hongwei for their support and for making sure there wasn't a dull moment in the office. I'd like to extend this thanks to Tiago, Xiang and Caroline too. Oh, and thank you all for not minding my huge Pringles collection in the office.

I am glad to be part of such an international and diverse department. I am grateful to all for making the department an enjoyable place. I enjoyed all our activities together. Andrei - thank you for your support and the interesting discussions. Thank you Ali, Vincentius, Pratik, Michael and Nan. Thank you Bram for always being ready to help and support the PhDs of our group. Thank you Aydin for always being ready to answer my barrage of questions. Yannos, I still chuckle remembering that moment in the anechoic chamber. Thank you Nitesh, Chirag, Marta, Chau, Eirini, Lubin, Chantal, Xi, Romina, Julian, Yuzhe, Fabricio, Leila, Niels, Ilias, Tian, Zahid, Maria, Nick, Jesse, Dimitrii, Giacomo and Milad. Thank you Camila and Raul - and special thanks for helping us during the 'big move'. It made our life so much easier. Thank you so much, Agnes and Laurike, for taking out time to translate my thesis summary and propositions to Dutch. Thank you Luigi for all the fun conversations whilst eating all my pistachios. Thank you Mohamed, Marouen and Yasine for the discussions and amazing time spent everyday. Thank you Ozan - we need to tick another Turkish restaurant from the list soon. I still find it amusing and cool that two of us are required to read and understand those old Ottoman books. Nicolas - thank you for understanding and appreciating my memes, for the best jump-scare reactions and for the game nights. Speaking of gaming, I'd also like to thank Megan and Sebastian for constantly reviving me without getting annoyed. Thank you to those friends too who are so-far-yet-so-close. I'd like to collectively thank you all for all the fun (and serious) discussions, deep (and inane) conversations and most importantly for supporting each other.

Words are inadequate to describe the support and prayers of my family members. Your sacrifices are immeasurable. Thank you Ma, Pa and Bhaiya for keeping me motivated from two different time zones and for your selfless care and support throughout the years.

I'm grateful for the prayers and well wishes of my friends and relatives, especially the elders. I'm also grateful for the prayers and well wishes of my parents-in-law and my wife who adds pizzazz to my everyday life. Likewise, Saliha, life would be incomplete without you. *Allahumma baarik*.

Nakash Nazeer
Delft, 2022

About the author

Nakash Nazeer was born in Chennai, India, on the 22^{nd} of September 1991. He received his B.E. in Aeronautical Engineering in 2013 from Hindustan University, Chennai, India.

His interest and passion for aerospace led him to Singapore where he received his MSc in Aerospace Engineering from Nanyang Technological University. The MSc. degree was a joint programme with The Technical University of Munich, Germany. During his masters he joined the Ultrasonic and NDE group led by Assoc. Prof. Dr. David Fan as a graduate student researcher. His research was on ultrasonic guided wave inspection for aircraft wing spar structures. He investigated the interaction of the shear horizontal guided wave mode with defects present in the bend region and studied the importance of the curvature effect on the different sensitivity to inner and outer bend defects.

In 2017 he moved to The Netherlands to purse his PhD in Aerospace Engineering at Delft University of Technology at the department of Aerospace Structures and Materials. Within the department he was part of the Aerospace NDT group led by Assoc. Prof. Dr. Roger Groves who was his PhD supervisor and also his promotor. The research in his study was part of the larger SmartX project involved in the design and development of an autonomous smart wing. He was responsible for the smart sensing of the SmartX wing which included shape sensing and load monitoring. He proposed, developed and demonstrated a novel fibre optic sensing method that was reliable, robust and cost effective for monitoring of morphing structures.